Distribution Agreement

In presenting this thesis or dissertation as a partial fulfillment of the requirements for an advanced degree from Emory University, I hereby grant to Emory University and its agents the non-exclusive license to archive, make accessible, and display my thesis or dissertation in whole or in part in all forms of media, now or hereafter known, including display on the world wide web. I understand that I may select some access restrictions as part of the online submission of this thesis or dissertation. I retain all ownership rights to the copyright of the thesis or dissertation. I also retain the right to use in future works (such as articles or books) all or part of this thesis or dissertation.

Signature:

_____   _____
Huanhuan Yang   Date

Parameter Estimation and Reduced-order Modeling in Electrocardiology

by

Huanhuan Yang
Doctor of Philosophy

Mathematics and Computer Science

_____
Alessandro Veneziani, Ph.D.
Advisor

_____
Michele Benzi, Ph.D.
Committee member

_____
David Borthwick, Ph.D.
Committee member

_____
Flavio Fenton, Ph.D.
Committee member

Accepted:

_____
Lisa A. Tedesco, Ph.D.
Dean of the James T. Laney School of Graduate Studies

_____
Date

Parameter Estimation and Reduced-order Modeling in Electrocardiology

by

Huanhuan Yang
M.S. in Mathematics, Chinese Academy of Sciences, 2010

Advisor: Alessandro Veneziani, Ph.D.

An abstract of
A dissertation submitted to the Faculty of the
James T. Laney School of Graduate Studies of Emory University
in partial fulfillment of the requirements for the degree of
Doctor of Philosophy
in Mathematics and Computer Science
2015

Abstract

Parameter Estimation and Reduced-order Modeling in Electrocardiology
By Huanhuan Yang

Computational modeling of electrocardiology (EC) has a great potential for use in improved diagnosis and prognosis of cardiac arrhythmia. However, recent computational methods usually suffer from three major limitations that hinder their clinical use: lack of efficient model personalization strategies; high computational demand from the EC solver; lack of good trade-off between the simplification of cellular ionic models and the demand on keeping sufficient biophysical details. This thesis aims at solving above challenges.

The principal part is on the estimation of cardiac conductivities that parameterize the bidomain/monodomain model—the current standard model for simulating cardiac potential propagation. We consider a variational approach by regarding the parameters as control variables to minimize the mismatch between computed and measured potentials. The existence of a minimizer of this misfit function is proved. We significantly improve the numerical approaches in the literature by resorting to a derivative-based optimization method with the settlement of some challenges due to discontinuity. Our numerical results is mainly in 3D, on both idealized and real geometries. We demonstrate the reliability and stability in presence of noise and with an imperfect knowledge of other model parameters.

We then focus on the computational cost reduction for the inverse conductivity problem. The Proper Orthogonal Decomposition (POD) approach is taken for forward model reduction, along with the Discrete Empirical Interpolation Method (DEIM) for tackling nonlinearity. In the application of this POD-DEIM combination, we obtain a rather small set of samples by sampling the parameter space based on polar coordinates and densifying the "boundary layer" of the sample space utilizing Gauss–Lobatto nodes. The computational effort is finally reduced by at least 90% in conductivity estimation.

The last part is developing a data-driven approach to the reduction of state-of-the-art cellular models in atrial electrophysiology. The reduced model predicts cellular action potentials (AP) in a simple form but is effective in capturing the physiological complexity of the original model. We start from an AP manifold learning, and continue with a regression model construction. The reduced cellular model drastically improves the performance of tissue-level atrial electrophysiological modeling and enables almost real-time computations.

Parameter Estimation and Reduced-order Modeling in Electrocardiology

by

Huanhuan Yang
M.S. in Mathematics, Chinese Academy of Sciences, 2010

Advisor: Alessandro Veneziani, Ph.D.

A dissertation submitted to the Faculty of the
James T. Laney School of Graduate Studies of Emory University
in partial fulfillment of the requirements for the degree of
Doctor of Philosophy
in Mathematics and Computer Science
2015

Acknowledgements

A lot of people have contributed to this fulfillment of my PhD study, and here I sincerely thank all of them.

I gratefully thank my advisor Alessandro Veneziani for introducing me to the filed of scientific computing. It has been a wonderful experience that I can bring math to the real world during my dissertation research. I hereby express my sincere gratitude to him for the guidance in solving practical issues beyond textbooks, for the optimism and enthusiasm he always delivers to me, for the patience he always keeps with me, and for the freedom and trust he always grants me in pursuing my scientific interests. Honestly, he is the most amazing advisor in the world.

I would like to thank the professors in my thesis committee: Michele Benzi, David Borthwick, and Flavio Fenton. From various perspectives including numerical analysis, functional analysis and electrophysiological experiment, their insightful comments, encouragement, and also hard questions have guided me towards more professional scientific research.

My special thank also goes to Tiziano Passerini and Tommaso Mansi (Siemens Corporate Research), who offered me an opportunity to join their team as intern. It was a highly rewarding experience from which I gained remarkable interest in clinic-oriented engineering and learned a lot of essential skills in multiple fields that help my professional growth.

I wish to thank Prof. Shanshuang Yang, with whom I was doing complex analysis in my first two years. Thank you for being supportive when I decided to switch to the world of applied math. I appreciate all the valuable advices, in teaching and in life, over the past five years.

I thank my fellow labmates in the ECM2 group: Tiziano, Mauro, Lucia, Alexis, Luca, Boyi, Jim, Gaetano, Huijuan, Sofia, Alexander (the 2nd), Alessandro (the 3rd). They have always been like family members, taking care of me and cheering me up in difficult moments. I enjoyed the valuable group help, the stimulating discussions and the countless days we were working together. A special note goes to Luca, who helped me a lot in the use of LifeV as well as in the theoretical discussion. I could expect a much harder time without him.

Finally, I would like to thank my family and my friends for their love and support. I enjoy all the pains and funs we have had in past years. To my lover Zhengyao: I don't fear death or poverty, I only fear the world without you.

To new applied mathematicians

Contents

List of Figures

List of Tables

Chapter 1

Introduction

1.1   Clinical significance of electrocardiological modeling

"Did you know that heart attacks can give you mathematics!?" This was posted by James Keener, an applied mathematician at University of Utah. Indeed, there are a vast of problems in cardiology that request merged contribution from a wide variety of disciplines including but not limited to mathematics, biomedical engineering, and medicine. This thesis is intended to contribute, mostly from the community of computational mathematics, to the fight for an improved application of electrocardiological modeling in the clinic.

Among cardiovascular diseases, the leading causes of death worldwide [83], particularly severe ones are the electrical dysfunctions of myocardium, such as *atrial* or *ventricular fibrillation*, that are categorized as *cardiac arrhythmia*. Cardiac arrhythmia is triggered by abnormal initiation and (or) abnormal propagation of electrical waves. Possible treatment therapies include synchronized electrical cardioversion, pharmacologic therapy, and catheter ablation of the underlying reentrant circuit. The choice of a proper therapy depends on the condition of the affected patient.

The *defibrillation* therapy by delivering a strong electric shock to the heart is generally effective for combating sudden cardiac death, but the necessary high-strength require-

ment on the shock would make conscious patients suffer from extreme pain and may cause permanent damage on the tissues around the shock electrodes [120]. Taking antiarrhythmic drugs (AAD) is another option for cardioversion, but it sometimes has side effects including chest pain, fainting, and swelling of the feet or legs [1]. In particular, no current AAD is atrial specific and one must take care to avoid adverse effects on ventricular rhythm. The objective of catheter ablation is to burn cardiac tissues with lines of conduction blocks in purpose of preventing initiation and maintenance of meander waves. Although it achieves a high success rate, the ideal lesion pattern with minimal burn on the tissue is still unknown. To sum up, there is a need for tools that allow better therapy planning.

Deeper understanding of cardiac electrophysiology (EP) is crucial for improved diagnosis and prognosis of cardiac arrhythmia. Computational modeling of healthy and diseased electrocardiology is becoming an additional formidable tool to complement *in vitro* and *in vivo* studies, and it has a great potential for use in clinical practice. Over the coming years, it is expected to provide non-invasive, cost effective and personalized assessment of the state of the heart; furthermore, it is desired to support the planning and guidance of treatment therapies such as rendering the optimal leisure pattern for ablation therapies. Therefore, computational electrocardiology has been a well-established field, whose importance relies upon both the intrinsic challenging mathematical/numerical features and the practical relevance to cardiac physiopathology [33, 69, 108].

In recent decades, computational electrocardiology has been highly attractive to researchers not only in academia but also in industry. Computational methods have been continuously refined and made closer and closer to clinical application. For instance, [28] provides an optimal control approach for cardiac defibrillation by determining an applied external stimulus such that it optimizes a given design objective. In [3], computational simulation of atrial fibrillation for AAD treatment has been investigated. An optimization of the ablation line pattern has also been studied in [37] and [71] by electrocardiological modeling. However, all current computational methods suffer from some limitations that

hinder their use in the clinic: high computational demand from the EP solver or lack of good model personalization strategies.

1.2   Some challenges in computational electrocardiology

The goal of computational electrocardiology is to provide efficient and reliable simulations of healthy or diseased electrical activity of the heart. We point out that this is not an easy task and we remark in the flowing the main challenges in this field. Several challenges are also presented in [25].

1. **Personalization challenge**. Electrocardiological models depend on parameters that typically come from appropriate but empirical constitutive laws, and their quantification for a specific patient may be problematic. In particular, the bidomain/monodomain model has been shown to be strongly sensitive to the cardiac conductivity parameter.

   Recent work on variational parameter estimation in electrocardiology utilized either a derivative-free optimization approach or a least-squares approach which usually involves a large number of optimization iterations. More efficient model personalization or parameter estimation techniques should be applied in this field.

2. **Simulation challenge**. The intrinsic complexity of the heart anatomy and the complex interplay among cell, tissue and organ modeling scales make the requirement on computational efficiency of simulation hard to be satisfied. This is even more true for an inverse problem of parameter estimation, as high computational cost arises in many "queries" of forward simulations with different model parameters.

   Model order reduction techniques have been investigated in the literature, but their application to conductivity estimation is challenging, due to the nonlinearity of the model and the exceptional feature like wave-front propagation of its solution.

3. **Modeling challenge**. It is difficult to keep the cardiac cellular model minimally

complicated so that it can be solved with little computational effort, but simultane-
ously make the model sufficiently detailed so that it can reproduce as much clinical
data as possible.

Several simplified or phenomenological models have been proposed as compu-
tationally efficient surrogates of biophysically detailed models. However, these
models usually lack the capability of describing important physiological proper-
ties. Moreover, no simplified model is currently available for human atria-specific
cellular electrophysiology.

4. **Alternans challenge**. The dependence of action potential duration (APD) on the
   pacing cycle length, called the restitution curve, and the onset of abnormal alter-
   ations of APD, called alternans, are important action potential features, but their
   accurate prediction through mathematical criterion is still under investigation.

1.3   Thesis outline

The work in this thesis is in the direction of trying to solve the challenging problems we
just mentioned. The outline of the thesis is as follows.

We start in **Chapter 2** with an overview of the electrical activity of the heart and the
mathematical models in electrocardiology that will be used in the following chapters.

In **Chapter 3** we estimate the cardiac conductivity parameter using a variational
data assimilation approach. We solve the **personalization challenge** by resorting to a
derivative-based optimization method and address some challenges involved due to dis-
continuity. We validate our conductivity estimation approach in presence of noise and
with an imperfect knowledge of other model parameters. The existence of a minimizer
of the misfit function, which calculates the mismatch between computed and measured
potentials, is proved in **Chapter 4** with the phenomenological Rogers–McCulloch ionic
model that completes the bidomain system.

In **Chapter 5** we use the Proper Orthogonal Decomposition (POD) model reduction

technique to efficiently solve the monodomain system. We present the way of tackling nonlinearity, that is, the Discrete Empirical Interpolation Method (DEIM). The POD-DEIM combination is finally applied for the inverse problem of cardiac conductivity estimation. We describe in detail the derivative-based optimization constrained by the reduced monodomain model. This chapter addresses the **simulation challenge**.

Chapter 6 aims at solving the **modeling challenge** that we mentioned before. A data-driven approach is developed for the model reduction of an atrial cellular model. We introduce the manifold learning techniques for dimensionality reduction and the non-linear regression methods for the reduced model construction. At the end, the reduced cellular model is applied for tissue-level electrocardiological modeling. We also present a restitution study by diastolic interval change, which intends to address the **alternans challenge**.

Concluding remarks and perspectives for future research directions are addressed at the end of these chapters, they are also summarized in **Chapter 7**.

Chapter 2

Mathematical models in electrocardiology

2.1 Heart function and electrical activity

2.1.1 Anatomy and function of the heart

The heart is situated in the middle of the chest cavity between the left and right lungs, and is enclosed in a membranous sac—the *pericardium*. The heart has four chambers: two blood-receiving chambers called the *atria* and two blood-discharging chambers called the *ventricles*. The detailed structure of the chambers and various accessory tissues is shown in Figure 2.1.

The heart is divided into left and right halves by an inner wall called the *septum*, supporting the function of pumping deoxygenated blood by the right and pumping oxygenated blood by the left. The *left atrium* (LA) and the *right atrium* (RA) are upper, smaller, and thinner, while the *left ventricle* (LV) and the *right ventricle* (RV) are lower, larger, and thicker. Each respective atrium and ventricle pair is separated by a *coronary sinus,* and connected by an atrioventricular valve that controls the blood flow between them. The valve in the right side is the *tricuspid valve,* and the one in the left is the *bicuspid valve* or the *mitral valve*. The heart wall is made of three layers. The outer layer

Anterior view
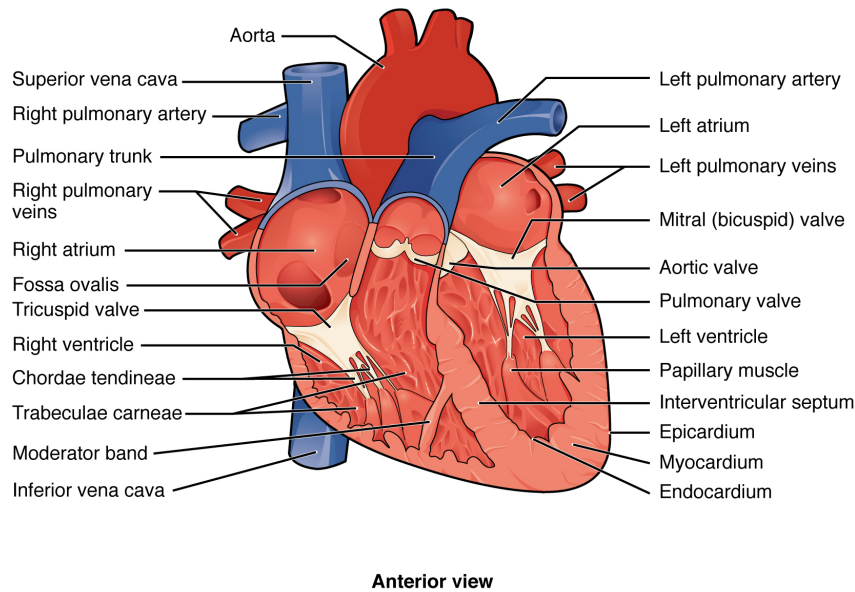
Figure 2.1: Internal structure of the heart. Major components include the four chambers, the major vessels, as well as the valves. From Wikimedia Commons, source: OpenStax College http://cnx.org/content/col11496/1.6/

is called the *epicardium*, the middle layer is the *myocardium*, which is the heart muscle, and the innermost layer is the *endocardium*.

The cardiac tissue consists mostly of muscle cells (*myocytes*) that are roughly in cylindrical shape with a length of 100 μm and a diameter of 10 to 20 μm in human ventricular tissue [108]. Myocytes are arranged in fibers, and layers of fibers—that are called *sheets*—constitute the myocardium. The gaps between adjacent cells within a sheet or between sheets are structural proteins called *collagens*, which enable the conduction of electrical signals.

The fiber orientation can be described by a local coordinate system, based on the tissue microstructure, including the fiber direction, the transverse direction in the sheet plane, and the cross-sheet direction. In ventricles, fibers smoothly rotate counterclockwise from epicardium to endocardium across the myocardium [76, 126] (see the illustration in Figure 2.2). In atria, the orientation varies gradually across the thickness of the walls and abruptly between bundles [61, 62], which refer to collections of fibers with the same general alignment. Myocardium fibers play an important role in the electrical conductivity,
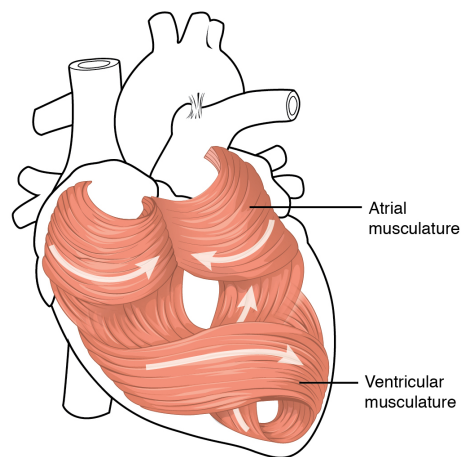
Figure 2.2: Heart musculature. From Wikimedia Commons, source: OpenStax College http://cnx.org/content/col11496/1.6/

as it is observed that electrical conduction along the length of myocytes is faster than transverse [90, 124]. The fiber orientation can be obtained *in vitro* using histology [126] or imaging techniques like diffusion tensor MRI [64, 105, 143]. These techniques perform well *ex-vivo*, but their application to moving heart is highly involved and the imaging techniques usually take long acquisition time. Consequently a patient-specific description of the fiber orientation is generally unachievable.

The heart functions as a pump, through both the systemic circulation and the pulmonary circulation, to provide a continuous circulation of blood throughout the body. A complete blood circulation throughout the heart is illustrated in Figure 2.3. The RA collects deoxygenated blood from two large veins, the *superior* and *inferior venae cavae*. This deoxygenated blood in the RA is then pumped through the tricuspid valve to the RV, and then through the pulmonary valve into the pulmonary artery. There the blood travels into the pulmonary circulation, collects oxygen from the lungs, and delivers carbon dioxide for exhalation. After re-oxygenation, the blood is returned to the LA via the pulmonary vein. It is then pumped through the bicuspid valve to the LV. The LV is responsible for pumping the re-oxygenated blood out into the aorta for the systemic circulation. In the systemic circulation, the blood travels through the whole body from the aorta which is the largest artery, then smaller arteries and arterioles, and eventually to the capillaries.
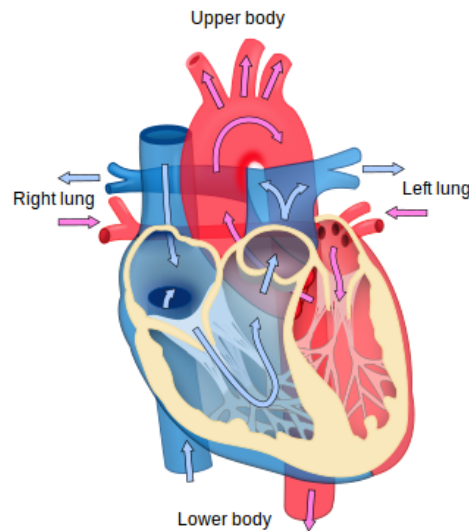
Figure 2.3: Blood flow through the heart. Blue components indicate de-oxygenated blood pathways and red components indicate oxygenated blood pathways. From Wikimedia Commons, author: ZooFari.

In the capillaries, the blood supplies oxygen and nutrients to body cells for metabolism, and collects the exchanged carbon dioxide and waste substances. After this exchange in the body, the blood enters the RA via the venous part of the systemic circulation.

Because the LV contracts forcefully to pump blood to the reset of the body, while the RV pumps blood only to the lungs, the LV has considerably thicker wall than the RV. As the atria fill largely through passive blood flow, the myocardium within the atria is the thinnest [108]. A cardiac cycle (a complete heartbeat) includes *systole* and *diastole* and the intervening pause. Systole is the period of contraction during which the ventricles pump blood to the body; diastole is the period when the ventricles relax and fill with blood. Typical systolic pressure (about 120 mmHg) and diastolic pressure (about 80 mmHg) can be measured non-invasively in the well-known clinical "blood pressure" test.

2.1.2 Electrical activity of cardiac myocytes

The cell membrane of cardiac muscle is composed of a phospholipid bilayer into which membrane-spanning proteins are woven [108]. The bilipid shell encapsulates a small volume that is known as the *intracellular space* (ICS). We will use the subscript i to de-

note properties of the intracellular space. The *extracellular space* (ECS) corresponds the volume outside the cell membrane, and the subscript e will be used for its property description. The combination of proteins in the bilipid layer forms tiny holes or pores in the cell membrane. These pores are selectively permeable: only specific ions are allowed to pass through the membrane under certain conditions. Because they are channels through which ions may flow, these pores are often referred to as *ionic channels*.

It is the property of selective permeability of the cell membrane that allows for the presence of an imbalanced ionic charge across the membrane and therefore the formation of a potential difference between the intracellular and extracellular spaces. This potential difference across the cell membrane is defined as the *transmembrane potential* u (or *membrane potential*):

$$u = u_i - u_e$$

where u_i is the potential in the intracellular space (called the *intracellular potential*) and u_e is the potential in the extracellular space (called the *extracellular potential*).

At rest, the intracellular and extracellular concentrations of each ion species are usually substantially different. Any natural flowing of a particular ion across the membrane down its concentration gradient will cause a flux of electrical charge, until the electrochemical equilibrium on this single ion is reached. The transmembrane potential at which there is no flow of an ion species is called the *reversal potential* of this ion, referring to the fact that a change around this potential reverses the direction of the ion flux. The reversal potential is also known as the *Nernst potential*, as it can be evaluated from the *Nernst equation* [108]

$$E_x = \frac{RT}{z_x F} \ln \left(\frac{[x]_e}{[x]_i} \right).$$

Here E_x is the Nernst potential for ion x, R is the universal gas constant, T is the absolute temperature, z_x is the valence of ion x and F is the Faraday's constant. The terms $[x]_e$ and $[x]_i$ denote the extracellular and intracellular concentrations of ion x. Typical ions that could give rise to a variation of the transmembrane potential over time are Na^+, K^+

and Ca^{2+}. Based on their concentrations at resting state [80] the Nernst potentials of these ions are $E_{Na} = 70$ mV, $E_{K} = -88$ mV and $E_{Ca} = 128$ mV at body temperature $37\,^{\circ}$C [108]. A cardiac muscle cell, as a multi-ion system, typically has a *resting potential* around -85 mV which is close to E_{K}, reflecting the dominant permeability of the cell membrane to K^{+} [108].

In each cardiac cell, if a stimulus of sufficient amplitude is applied, either by an electric current from an adjacent cell through gap junction, or by an electric impulse fired autonomously from pacemaker cells, or by an artificial device, the transmembrane potential will rise above a critical value known as the *threshold potential* and fall following a particular trajectory. This active response is known as the cardiac *action potential* (AP). A typical cardiomyocyte AP is illustrated in Figure 2.4. The action potential has 5 phases [108]:

Phase 4 At rest when the cell is not being stimulated, the cell membrane is in a polarized state (phase 4) with a resting potential around -85 mV. This is what happens in 99% of cardiac muscle cells [122].

Phase 0 Once the cell is electrically stimulated, the opening of the fast Na^{+} channels causes a rapid influx of sodium ions and thus produces an upstroke at the beginning of the AP. The transmembrane potential is reversed from negative to positive and to the peak voltage about 30 mV. Therefore phase 0 is known as the *depolarization* phase. The slope of the depolarization phase indicates the maximum rate of increase of the transmembrane potential and is denoted as $\max \frac{du}{dt}$.

Phase 1 After depolarization, the fast Na^{+} channels are inactive and the outward movement of potassium ions drives the potential to rapidly decrease (phase 1). When the potential returns to a negative voltage the cell is *repolarized*. This happens shortly and phase 1 is therefore called the rapid repolarization (or brief repolarization) phase.

Phase 2 The long-lasting "plateau" phase of the AP is sustained by a balance between
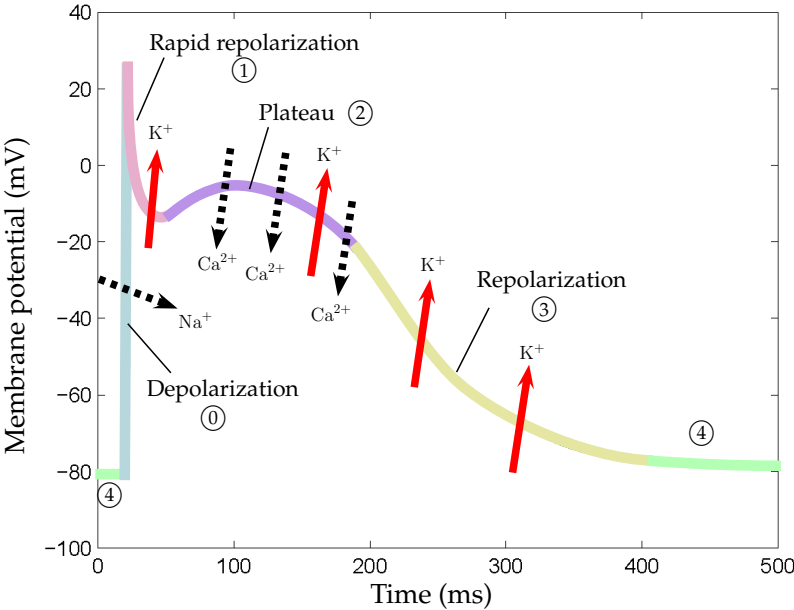
Figure 2.4: Typical action potential of a cardiac muscle cell.
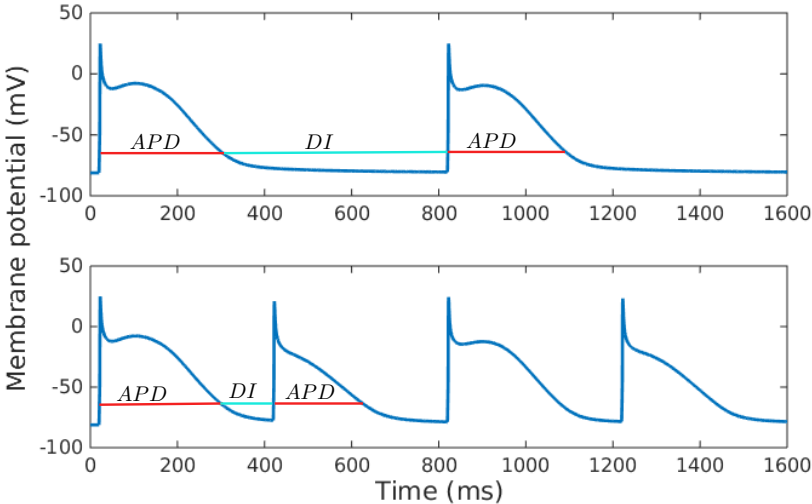
Figure 2.5: Restitution feature of the action potential. Top: slow pacing ($CL = 800$ ms) yields normal APD. Bottom: faster pacing ($CL = 400$ ms) causes shorter APD.

the influx of the calcium ions and the efflux of the potassium ions. The outward potassium current I_K tends to drive the cell back to the resting state, whereas the inward calcium current I_Ca holds the transmembrane potential in a depolarized value.

Phase 3 The calcium current I_Ca fails when the Ca^{2+} channels close in phase 3, then the potassium current I_K brings the voltage to the resting potential (phase 4).

The duration of an action potential is commonly quantified by the *action potential duration* (APD) (see Fig. 2.5), which is the amount of time during which u keeps elevated above some specified voltage. Suppose a cell is repeatedly stimulated with a period called pacing *cycle length* (CL), we characterize the amount of rest the cell stays in between consecutive action potentials by the the *diastolic interval* (DI), which is simply given as $DI = CI - APD$. As illustrated in Fig. 2.5, the shorter the DI of current action potential, the shorter the APD of the next one. This dependence of APD on DI is typically characterised as the *restitution* of APD.

2.1.3 Electrical activity of the heart

Mechanical contraction of the heart for blood pumping is caused by the electrical excitation of the heart. The heart has the ability to initiate electrical activity spontaneously at a regular pace, and the electrical activity continues even if the heart is removed from the body. The initiation and conduction of the electrical activity can be described in sequence, shown schematically in Figure 2.6.

The electrical excitation is initiated by a natural pacemaker known as the *sinoatrial* (SA) node, located on the upper portion of the RA wall near the superior vena cave. The SA node normally generates action potentials at the rate of 60 to 100 per minute in a resting adult human heart [108]. The action potential travels across firstly the right atrium and then the left atrium through specialized electrical pathways, until it reaches the *atriaventricular* (AV) node. Once the atria are depolarized, the muscles are excited so they contract and pump blood into ventricles.
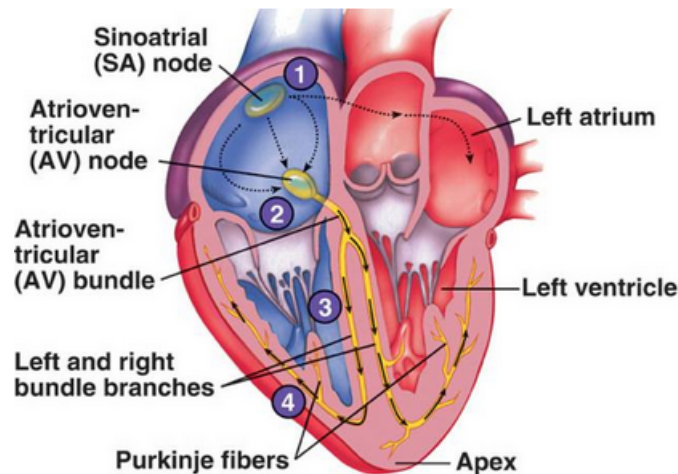
Figure 2.6: The cardiac excitation sequence through the electrical conduction pathways. Source: http://www.austincc.edu/apreview/PhysText/Cardiac.html

The excitation propagation through the AV node, located in the cardiac septum between atria and ventricles, is slightly delayed. The AV node has the function of autonomous excitation similar to the SA node, but it is still paced by the electrical impulse propagated from the SA node since its own beat rate is slower, ranging from 40 to 55 beats per minute. The AV node is the only electrical pathway from atria to ventricles. When the electrical impulse is held up by the AV node for a brief period, the delay allows the atria to finish blood pumping before the action potential propagates through the ventricles and causes them to contract.

Following the delay, the electrical impulse conducts through the *bundle of His* and enters the ventricles. The bundle of His splits after a short distance into left and right bundle branches, which continue down the septal wall and subdivide into further branches. These branches form a complex network of fibers called the *Purkinje fiber* network, spreading across the inner ventricular walls and into the subendocardial region of the ventricular myocardium. From the bundle of His, the electrical activity runs down the septum and reaches the apex of the heart, and then through the Purkinjie fibers it disperses throughout the myocardium. The rest of ventricular cells are lastly activated by cell-to-cell propagation of the action potential through gap junctions. The excited ventri-
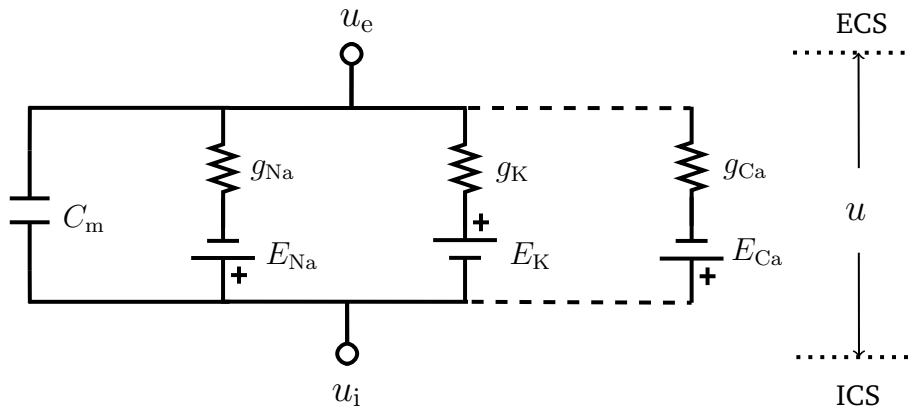
Figure 2.7: A standard electric circuit describing the electrical function of the cell membrane. The cell membrane acts as a capacitor with capacitance C_{m}. The channel of ion x acts as a resistor with the conductance g_x. The difference between u and the Nernst potential E_x governs the direction of the associated current flow, thus it acts as a battery in the circuit.

cles then contract and pump blood into the circulation systems.

The normal propagation of electrical excitation can be interfered with ectopic firing foci or cardiac fibrosis. The former can initiate abnormal electrical waves hence cause action potential alternans, the latter functions as obstacles that prevent the electrical conduction. Either of these pathological conditions would provoke *cardiac arrhythmia* such as *tachycardia* and *fibrillation*.

2.2   Electrocardiological models in the cellular level

The mechanism behind the occurrence of action potential, which represents the variation of the transmembrane potential over time, is the movement of ions causing the currents flowing across the cell membrane. This potential variation can be modeled and reproduced by regarding the cell membrane as an equivalent electric circuit. A standard formation is to analogize the cell membrane to a capacitor in parallel with a sequence of resistors mimicking different ionic channels in the membrane, as shown in Fig. 2.7.

For the current I_x flowing across the channel of an arbitrary ion x, its direction is determined by the difference between the transmembrane potential u and the Nernst

potential E_x. Let g_x be the conductance of this ionic channel, we formulate

$$I_x = g_x(u - E_x).$$

The conductances of ionic channels in general have complex dependencies. They vary along with the opening (activity) and closing (inactivity) of the associated channels. They are also sensitive to the transmembrane potential and sometimes the concentrations of specific ions. Therefore the representation of I_x is generally nonlinear. For convenience, let us denote by I_{ion} the the total current flowing through all ionic channels: $I_{\mathrm{ion}} = \sum_x I_x$. With the parallel arrangement in the electric circuit, we can compute the total current flow I_{m} through the membrane as

$$I_{\mathrm{m}} = C_{\mathrm{m}} \frac{du}{dt} + I_{\mathrm{ion}}$$

where C_{m} is the capacitance of the cell membrane per unit area. The action potential of an isolated cell ($I_{\mathrm{m}} = 0$ in this case) can be reconstructed by the ordinary differential equation (ODE)

$$\frac{du}{dt} = -\frac{I_{\mathrm{ion}} + I_{\mathrm{stim}}}{C_{\mathrm{m}}} \tag{2.1}$$

where I_{stim} denotes an external stimulus current—necessary when the cell is at rest—to trigger the excitation of the cell.

A wide range of cardiac ionic models have been developed representing the action potentials of different cell types: ventricular cell, atrial cell, sinoatrial node cell, and so on. A summary on these models can be found in [44] and in the CellML repository [1]. The cell models differ in the manner of development and also in the level of details described regarding the biophysics of the underlying mechanisms.

In the following, we will introduce the ionic models that are adopted in this thesis, classified by the manner of development.

---

[1]CellML, https://models.cellml.org/electrophysiology.

2.2.1 Biophysics-based ionic models

The aim of a biophysics-based cardiac cell model is to reproduce the action potential of a cell by accurately modeling the underlying sub-cellular processes, such as ion transfers, pumps and exchanges across the cell membrane.

These biophysical models originated from the Hodgkin–Huxley model ([63], 1952) of the squid giant axon. Since its appearance, a considerable number of cardiac cell models have been developed in the last decades, with a continuous increase on the number of ionic currents described. In particular, we mention some of the better known models: the Beeler–Reuter model ([13], 1977, 3 currents) of mamalian ventricular cells, the Luo–Rudy I model ([79], 1991, 6 currents) of guinea pig ventricular cells, the Courtemanche–Ramirez–Nattel (CRN) model ([36], 1998, 12 currents) of human atrial cells, and the Ten Tusscher–Noble–Noble–Panfilov (TNNP) model ([131], 2004, 12 currents) of human ventricular cells.

A general form of this class of models reads

$$
\begin{cases}
I_{\text{ion}} = \sum_{i=1}^{M} I_{x_i}(u, \mathbf{w}, \mathbf{c}) \\[2mm]
\dfrac{d\mathbf{w}}{dt} + \mathbf{g}(u, \mathbf{w}, \mathbf{c}) = \mathbf{0} \\[2mm]
\dfrac{d\mathbf{c}}{dt} + \mathbf{h}(u, \mathbf{w}, \mathbf{c}) = \mathbf{0}
\end{cases}
\tag{2.2}
$$

where I_{x_i} is the ionic current associated with ion species x_i, $\mathbf{w}$ is the vector of J gating variables $\{w_j\}_{j=1}^{J}$ and $\mathbf{c}$ is the vector of K typical ion concentrations $\{c_k\}_{k=1}^{K}$. The dynamic of the transmembrane potential u is governed by the equation (2.1). The gating variable w_j describes the probability that the j-th gate will open to allow the ion transfer through particular ion channels, thus it is in the range of $[0, 1]$. A simple example of using gating variable w_j is to model the conductance of ion species x_i as $g_{x_i} = \overline{g}_{x_i} w_j$, where $\overline{g}_{x_i}$ is the maximum value of conductance. The dynamic of the gating variable w_j is typically described by an ODE

$$
\frac{dw_j}{dt} = \alpha_{w_j}(1 - w_j) - \beta_{w_j} w_j
$$

where α_{w_j} and β_{w_j} are voltage-dependent variables and their formulation generally contains exponential functions of u.

The dynamics of typical ion concentrations are modeled only recently. In cell models developed at earlier ages, such as the Beeler-Reuter model and the Luo–Rudy I model, the ion concentrations are treated as constants, because the variations of ion concentrations over time caused by the occurrence of action potential are often negligible.

We introduce in particular the CRN atrial ionic model which is adopted in Chapter 6 and the TNNP ventricular ionic model as a comparison with the minimal ventricular ionic introduced in the next subsection.

The CRN atrial ionic model

The CRN ionic model was developed using specific formulations of the Na^+, K^+, Ca^{2+} currents based on human atrial cell data, along with the inclusion of pump, exchange, and background currents [36]. The model includes 12 ionic currents governed by the time evolution of 21 state variables. Specifically, the total ionic current is formulated as

$$I_{\mathrm{ion}} = I_{\mathrm{Na}} + I_{\mathrm{K1}} + I_{\mathrm{to}} + I_{\mathrm{Kur}} + I_{\mathrm{Kr}} + I_{\mathrm{Ks}} + I_{\mathrm{Ca,L}} + I_{\mathrm{p,Ca}} + I_{\mathrm{NaK}} + I_{\mathrm{NaCa}} + I_{\mathrm{b,Na}} + I_{\mathrm{b,Ca}} \quad (2.3)$$

with each term in the sum denoting an ionic or pump/exchanger current. In particular, I_{Na} represents the fast Na^+ current, I_{Kur} is the ultrarapid delayed retifier K^+ current, $I_{\mathrm{Ca,L}}$ denotes the L-type Ca^{2+} current, and $I_{\mathrm{Na,Ca}}$ represents the Na^+/Ca^{2+} exchanger current. Figure 2.8 shows a schematic representation of these membrane currents and pump/exchanger currents. Inside the cell, three compartments are included: myoplasm, sarcoplasmic reticulum (SR) release compartment or junctional SR (JSR), and SR uptake compartment or network SR (NSR).

The model uses 21 state variables: the membrane potential u; 12 gating variables for the membrane currents ($m, h, j, o_a, o_i, u_a, u_i, x_r, x_s, d, f, f_a$); 3 gating variables for the Ca^{2+} currents through SR (u_u, v, w); 3 intracellular concentrations ($[Na^+]_{\mathrm{i}}, [K^+]_{\mathrm{i}}, [Ca^{2+}]_{\mathrm{i}}$); 2 Ca^{2+} concentrations in SR ($[Ca^{2+}]_{\mathrm{rel}}, [Ca^{2+}]_{\mathrm{up}}$). For a complete explanation on these
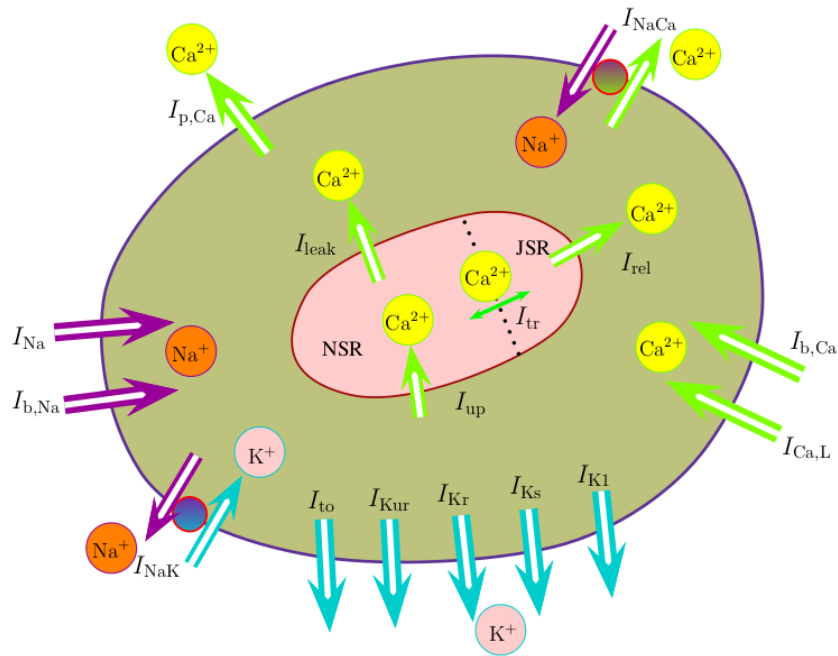
Figure 2.8: Schematic representation of the currents, pumps, and exchangers in the CRN atrial cell model
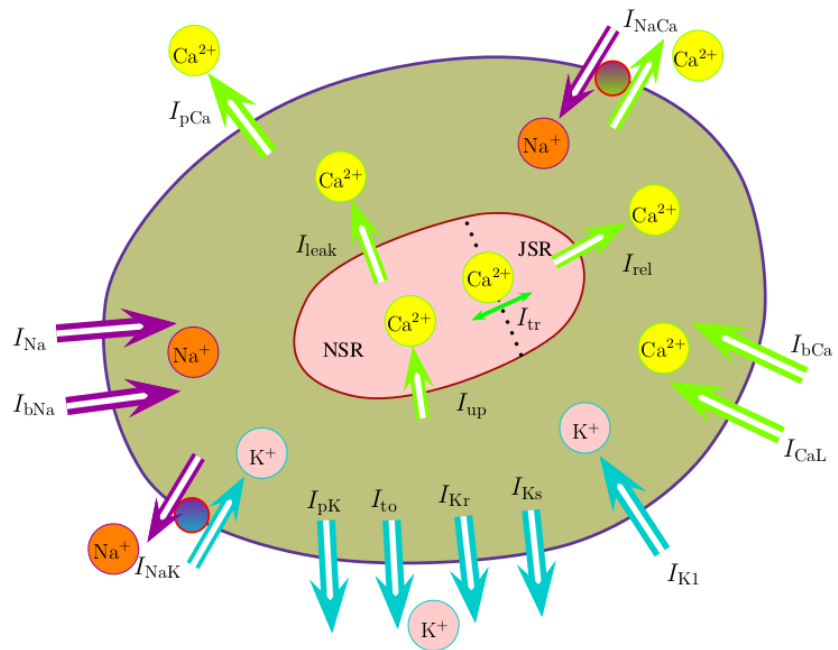
Figure 2.9: Schematic representation of the currents, pumps, and exchangers in the TNNP ventricular cell model

currents and their mathematical formulation please refer to Table 2.1, more details on the dynamics of state variables are given in the original publication [36].

The TNNP ventricular ionic model

The TNNP ionic model includes a high level of biophysics details. It reproduces the experimental data on important action potential features of human ventricular cells. The model includes 12 membrane currents and they are summed up as the total ionic current

$$I_{\mathrm{ion}} = I_{\mathrm{Na}} + I_{\mathrm{K1}} + I_{\mathrm{to}} + I_{\mathrm{Kr}} + I_{\mathrm{Ks}} + I_{\mathrm{CaL}} + I_{\mathrm{NaCa}} + I_{\mathrm{NaK}} + I_{\mathrm{pCa}} + I_{\mathrm{pK}} + I_{\mathrm{bCa}} + I_{\mathrm{bNa}}. \quad (2.4)$$

Specifically, these currents in order are: fast Na^+, inward rectifier K^+, transient outward K^+, rapid and slow components of the delayed rectifier K^+, L-type Ca^{2+}, $\mathrm{Na}^+/\mathrm{Ca}^{2+}$ exchanger, Na^+-K^+ pump, plateau Ca^{2+} and K^+ , and background Ca^{2+} and Na^+ currents. A schematic representation of these currents are shown in Figure 2.9. The TNNP model uses 17 state variables: the membrane potential, 12 gating variables, and 4 ion concentrations.

2.2.2   Reduced ionic models

Biophysics-based cell models include the ionic currents with high level of reality but also complexity, hence their numerical solutions in large-scale problems are often computationally demanding and the mathematical formation of their adjoint equations are considerably complicated. As an alternative, reduced ionic models have been developed from biophysically detailed ones. Typically, these reduced models were formulated by disregarding detailed sub-cellular processes and considering only the most contributing ones to the action potential.

A general form of these reduced ionic models and also those phenomenological models

Table 2.1: Currents in the CRN ionic model. The symbol u denotes the transmembrane potential which is denoted by V_{m} in [36] and the gating variable u_u is the same as the gating variable u in [36]. The expressions of some currents are omitted due to complexity, we refer to [36] for details.

Membrane currents	Expressions	State variables	Model constants
Fast Na$^+$ current	$I_{\mathrm{Na}} = g_{\mathrm{Na}} m^3 h j (u - E_{\mathrm{Na}})$	u m h j [Na$^+$]$_{\mathrm{i}}$	g_{Na} [Na$^+$]$_{\mathrm{o}}$
Time-independent K$^+$ current	$I_{\mathrm{K1}} = \dfrac{g_{\mathrm{K1}}(u - E_{\mathrm{K}})}{1 + \exp[0.07(u + 80)]}$	u [K$^+$]$_{\mathrm{i}}$	g_{K1} [K$^+$]$_{\mathrm{o}}$
Transient outward K$^+$ current	$I_{\mathrm{to}} = g_{\mathrm{to}} o_a^3 o_i (u - E_{\mathrm{K}})$	u o_a o_i [K$^+$]$_{\mathrm{i}}$	g_{to} [K$^+$]$_{\mathrm{o}}$
Ultrarapid delayed rectifier K$^+$ current	$I_{\mathrm{Kur}} = g_{\mathrm{Kur}} u_a^3 u_i (u - E_{\mathrm{K}})$	u u_a u_i [K$^+$]$_{\mathrm{i}}$	g_{Kur} [K$^+$]$_{\mathrm{o}}$
Rapid delayed outward rectifier K$^+$ current	$I_{\mathrm{Kr}} = \dfrac{g_{\mathrm{Kr}} x_r (u - E_{\mathrm{K}})}{1 + \exp(\frac{u+15}{22.4})}$	u x_r [K$^+$]$_{\mathrm{i}}$	g_{Kr} [K$^+$]$_{\mathrm{o}}$
Slow delayed outward rectifier K$^+$ current	$I_{\mathrm{Ks}} = g_{\mathrm{Ks}} x_s^2 (u - E_{\mathrm{K}})$	u x_s [K$^+$]$_{\mathrm{i}}$	g_{Ks} [K$^+$]$_{\mathrm{o}}$
L-type Ca^{2+} current	$I_{\mathrm{Ca,L}} = g_{\mathrm{Ca,L}} d f f_{\mathrm{Ca}} (u - 65)$	u d f f_{Ca}	$g_{\mathrm{Ca,L}}$
Background Ca^{2+} current	$I_{\mathrm{b,Ca}} = g_{\mathrm{b,Ca}} (u - E_{\mathrm{Ca}})$	u [Ca^{2+}]$_{\mathrm{i}}$	$g_{\mathrm{b,Ca}}$ [Ca^{2+}]$_{\mathrm{o}}$
Background Na$^+$ current	$I_{\mathrm{b,Na}} = g_{\mathrm{b,Na}} (u - E_{\mathrm{Na}})$	u [Na$^+$]$_{\mathrm{i}}$	$g_{\mathrm{b,Na}}$ [Na$^+$]$_{\mathrm{o}}$
Ca^{2+} pump current	$I_{\mathrm{p,Ca}} = \dfrac{I_{\mathrm{p,Ca(max)}} [\mathrm{Ca}^{2+}]_{\mathrm{i}}}{0.0005 + [\mathrm{Ca}^{2+}]_{\mathrm{i}}}$	[Ca^{2+}]$_{\mathrm{i}}$	$I_{\mathrm{p,Ca(max)}}$
Na$^+$-K$^+$ pump current	I_{NaK}	[Na$^+$]$_{\mathrm{i}}$	$I_{\mathrm{NaK(max)}}$ [Na$^+$]$_{\mathrm{o}}$ [K$^+$]$_{\mathrm{o}}$ $K_{\mathrm{m,Na(i)}}$ $K_{\mathrm{m,K(o)}}$
Na$^+$/Ca^{2+} exchanger current	$I_{\mathrm{Na,Ca}}$	[Na$^+$]$_{\mathrm{i}}$ [Ca^{2+}]$_{\mathrm{i}}$	$I_{\mathrm{NaCa(max)}}$ k_{sat} γ [Na$^+$]$_{\mathrm{o}}$ [Ca^{2+}]$_{\mathrm{o}}$ $K_{\mathrm{m,Na}}$ $K_{\mathrm{m,Ca}}$
Ca^{2+} currents through SR	I_{rel} I_{tr} I_{up} I_{leak}	u_u v w [Ca^{2+}]$_{\mathrm{rel}}$ [Ca^{2+}]$_{\mathrm{up}}$ [Ca^{2+}]$_{\mathrm{i}}$	k_{rel} $I_{\mathrm{up(max)}}$ K_{up} [Ca^{2+}]$_{\mathrm{up(max)}}$

mentioned later in Section 2.2.3 reads

$$\begin{cases} I_{\text{ion}} = \sum_{i=1}^{M} I_{x_i}(u, \mathbf{w}) \\ \dfrac{d\mathbf{w}}{dt} + \mathbf{g}(u, \mathbf{w}) = \mathbf{0} \end{cases} \tag{2.5}$$

where $\mathbf{w}$ is the vector of gating variables as before, but the dynamics of ion concentrations are not considered.

Some examples of reduced ionic models include the Fenton–Karma ionic model [45], the minimal ventricular ionic model [21], and the Mitchell–Schaeffer ventricular ionic model [88]. In particular, we introduce in the following the minimal ionic model which is adopted in Chapter 3 and the Mitchell–Schaeffer model which is used in Chapter 6.

The minimal ventricular ionic model

As the name suggests, the attractive feature of this model is the low number of state variables (only four) in comparison with other biophysics-based models. Nevertheless, it can be fitted to reproduce in detail experimentally measured characteristics of human ventricular action potentials as well as the dynamics of more complex models (such as the TNNP model) with less computational effort. These characteristics are in tissue-level and they include the action potential amplitude and morphology, the upstroke velocity, the *action potential duration* (APD), the conduction velocity (CV) restitution property, and so on [21].

Instead of including a wide range of ion channel currents, the total ionic current of the model is designed as the sum of all three membrane currents: a fast inward current, a slow inward current, and a slow outward current. The model, having denoted $\mathbf{w} = [v, w, s]^T$, reads

$$I_{\text{ion}}(u, [v, w, s]^T) = 85.7 C_{\text{m}}(J_{\text{fi}} + J_{\text{so}} + J_{\text{si}})$$

$$J_{\text{fi}} = -vH(\tilde{u} - \theta_v)(\tilde{u} - \theta_v)(u_u - \tilde{u})/\tau_{fi}$$

$$J_{\text{so}} = (\tilde{u} - u_o)(1 - H(\tilde{u} - \theta_w))/\tau_o + H(\tilde{u} - \theta_w)/\tau_{so}$$

$$J_{\text{si}} = -H(\tilde{u} - \theta_w)ws/\tau_{si}$$

$$\mathbf{g}(u, [v, w, s]^T) = \begin{bmatrix} -(1 - H(\tilde{u} - \theta_v))(v_\infty - v)/\tau_v^- + H(\tilde{u} - \theta_v)v/\tau_v^+ \\[2mm] -(1 - H(\tilde{u} - \theta_w))(w_\infty - w)/\tau_w^- + H(\tilde{u} - \theta_w)w/\tau_w^+ \\[2mm] -((1 + \tanh(k_s(\tilde{u} - u_s)))/2 - s)/\tau_s \end{bmatrix} \tag{2.6}$$

where $\tilde{u} = (u + 84)/85.7$ and $H(\cdot)$ is the standard Heaviside step function intended to model switch-like dynamics. There are several coefficients in (2.6) dependent on the voltage variable u and they are defined as follows:

$$\tau_v^- = (1 - H(\tilde{u} - \theta_v^-))\tau_{v1}^- + H(\tilde{u} - \theta_v^-)\tau_{v2}^-$$

$$\tau_w^- = \tau_{w1}^- + (\tau_{w2}^- - \tau_{w1}^-)(1 + \tanh(k_w^-(\tilde{u} - u_w^-)))/2$$

$$\tau_{so} = \tau_{so1} + (\tau_{so2} - \tau_{so1})(1 + \tanh(k_{so}(\tilde{u} - u_{so})))/2$$

$$\tau_s = (1 - H(\tilde{u} - \theta_w))\tau_{s1} + H(\tilde{u} - \theta_w)\tau_{s2}$$

$$\tau_o = (1 - H(\tilde{u} - \theta_o))\tau_{o1} + H(\tilde{u} - \theta_o)\tau_{o2}$$

$$v_\infty = 1 - H(\tilde{u} - \theta_v^-)$$

$$w_\infty = (1 - H(\tilde{u} - \theta_o(1 - \tilde{u}/\tau_{w\infty}) + H(\tilde{u} - \theta_o)w_\infty^*.$$

The model parameters used in Chapter 3 are from [21] and reported in Table 2.2.

The Mitchell–Schaeffer ventricular ionic model

The Mitchell–Schaeffer model [88] is a simplification from the Fenton–Karma model [45]. The model contains only one gating variable and just two ionic currents. In this case, the gating variable will be denoted by w (no bold since this is not a vector as it is in

Table 2.2: Minimal ionic model parameters

Parameter	Value	Parameter	Value
u_o	0	τ_{v2}^-	1150
u_u	1.58	τ_v^+	1.4506
θ_v	0.3	τ_{w1}^-	70
θ_w	0.015	τ_{w2}^-	20
θ_v^-	0.015	k_w^-	65
θ_o	0.006	u_w^-	0.03
τ_{v1}^-	60	τ_w^+	280
τ_{fi}	0.11	τ_{s1}	2.7342
τ_{o1}	6	τ_{s2}	3
τ_{o2}	6	k_s	2.0994
τ_{so1}	43	u_s	0.9087
τ_{so2}	0.2	τ_{si}	2.8723
k_{so}	2	$\tau_{w\infty}$	0.07
u_{so}	0.65	w_∞^*	0.94

Table 2.3: Rogers–McCulloch model parameters from [108] and [49].

Parameter	Value [108]	Value [49]	Unit
C_{m}	1	1	$\mu\mathrm{Fcm}^{-2}$
V_{r}	-85	-85	mV
V_{th}	-75	-72	mV
V_{p}	15	15	mV
c_1	0.26	11.54	ms^{-1}
c_2	0.1	4.4	ms^{-1}
b	0.013	0.012	ms^{-1}
d	0.8	1	—

general). The model describes dynamics of the normalized AP $u(t) \in [0, 1]$, it reads

$$I_{\text{ion}}(u, w) = -C_{\text{m}}(J_{\text{in}} + J_{\text{out}})$$

$$J_{\text{in}} = wu^2(1 - u)/\tau_{\text{in}}$$

$$J_{\text{out}} = -u/\tau_{\text{out}} \tag{2.7}$$

$$g(u, w) = \begin{cases} (w - 1)/\tau_{\text{open}} & \text{if } u < v_{\text{gate}} \\ w/\tau_{\text{close}} & \text{if } u > v_{\text{gate}}. \end{cases}$$

Because of its simplicity, this model can be understood analytically, which allows a rather complete study about the dependence of the model features on the model parameters. Moreover, one can derive an explicit formula for the restitution curve from the model.

2.2.3   Phenomenological ionic models

There are some ionic models that aim to simulate only the basic (phenomenological) characteristics of an action potential with limited computational cost. They do not seek to address the underlying processes or reproduce actually the experimentally observed data. It is nature to classify them as phenomenological models. These models are derived from simplification of the Hodgkin–Huxley model and the variables in such models typically have no physical meaning.

The first widely known phenomenological model is the FitzHugh–Nagumo model proposed by FitzHugh [47] and Nagumo et al. [94] independently for a generic excitable medium. Later on, Rogers and McCulloch [116] modified the FitzHugh–Nagumo model with the aim of developing a more realistic action potential. The Rogers–McCuloch model is used in chapter 3–5, and hence it is introduced in the following.

The Rogers–McCulloch ionic model

The Rogers–McCulloch model is based on a cubic polynomial formulation for I_{ion}, and a single gating variable for the simulation of depolarization and repolarization. The gating variable is denoted by the non-bold w. The model reads

$$I_{\mathrm{ion}}(u, w) = C_{\mathrm{m}}[\beta_1(u - V_{\mathrm{r}})(u - V_{\mathrm{th}})(u - V_{\mathrm{p}}) + c_2(u - V_{\mathrm{r}})w]$$

$$g(u, w) = -\beta_2(u - V_{\mathrm{r}}) + bdw$$

(2.8)

where $\beta_1 = \frac{c_1}{(V_{\mathrm{p}} - V_{\mathrm{r}})^2}$, $\beta_2 = \frac{b}{V_{\mathrm{p}} - V_{\mathrm{r}}}$. The model parameters used in the first test of chapter 3 are from [108], whereas the parameters in chapter 5 are from [108] since they create more realistic AP. These parameters are reported in Table 2.3.

It is analyzed in [116] that when the transmembrane potential is over the threshold V_{th} the upstroke of action potential starts and drives the transmembrane potential to the plateau voltage V_{p}, otherwise the transmembrane potential tends to the resting potential V_{r}. By the cubic description of I_{ion} the model captures the most relevant features of an action potential as interpolated here, therefore it can be adopted with adjusted model parameters for patient-specific simulations, when the goal is more like a qualitative study.

2.3 Electrocardiological models in the tissue level

The *bidomain model* is currently considered as the most physiologically founded description for the dynamics of electric potentials—the transmembrane potential and the extracellular potential—at the level of cardiac tissue. It was first proposed by Schmitt in 1969 [121] before being applied to cardiac tissue by Tung, Miller and Geselowitz in 1978 [85, 130]. Since its initial formulation, it has been well-known among researcher. In recent decades, the validation of the bidomian model in vitro [91, 137] and its ability to reproduce cardiac phenomena [117, 129] make the bidomain model a proper candidate for simulating action potential spreading in the myocardium as well as electrocardiograms.

The derivation of the bidomain model is based on several assumptions [108]:

1. as the result of a "homogeneization" procedure the intra- and extracellular domains are coexisting at each point of the cardiac domain, and this is where the name "bidomain" from;

2. there is no direct current flow between the intracellular and extramyocardial spaces;

3. the current flow between the extracellular and extramyocardial spaces occurs through the boundary of the cardiac domain;

4. the quasi-static approximation [107] is applied on the electrical and magnetic activity generated inside the body. Namely, the changes of electric/magnetic fields over time are ignored.

The current density $\mathbf{J}_i$ in the intracellular space can be formulated, by the Ohm's law, as $\mathbf{J}_i = \boldsymbol{\sigma}_i \mathbf{E}_i$. Here $\mathbf{E}_i$ is the electric field strength and $\boldsymbol{\sigma}_i(\mathbf{x})$ is the symmetric conductivity tensor in the intracellular domain. Under the quasi-static assumption on Maxwell's equations, the electric field can be expressed as $\mathbf{E}_i = -\nabla u_i$. We can express the current density $\mathbf{J}_i$ accordingly as

$$\mathbf{J}_i = -\boldsymbol{\sigma}_i \nabla u_i. \tag{2.9}$$

The current density in the extracellular space can be expressed similarly using analogous notations

$$\mathbf{J}_e = -\boldsymbol{\sigma}_e \nabla u_e. \tag{2.10}$$

Under the assumptions 2 and 3, any current that leaves one of the intra- and extracellular domains inside the cardiac tissue must across the membrane and flow into the other domain. This means the change of current density in each domain should be opposite in sign and equal in magnitude. Furthermore, by the conservation of current densities, the change of current density in each domain should be equal to the current I_m flowing

across the membrane. These relations are expressed as

$$\begin{aligned}
\nabla \cdot (\boldsymbol{\sigma}_i \nabla u_i) &= \beta I_m \\
\nabla \cdot (\boldsymbol{\sigma}_e \nabla u_e) &= -\beta I_m
\end{aligned}$$

(2.11)

where β is the surface-to-volume ratio of the membrane.

Recall that the membrane current flow I_m can be described as

$$I_m = C_m \frac{\partial u}{\partial t} + I_{ion}$$

(2.12)

where C_m is the membrane capacitance per unit area and I_{ion} is the total ionic current whose explicit form would be described by a coupled ionic model. Combining (2.11) and (2.11), we obtain the bidomain model in a symmetric form as

$$\begin{cases}
\beta C_m \dfrac{\partial u}{\partial t} - \nabla \cdot (\boldsymbol{\sigma}_i \nabla u_i) + \beta I_{ion} = 0 \\[2mm]
-\beta C_m \dfrac{\partial u}{\partial t} - \nabla \cdot (\boldsymbol{\sigma}_e \nabla u_e) - \beta I_{ion} = 0
\end{cases}$$

(2.13)

Extensive introductions to this model can be found for instance in [33, 69, 108].

If the cardiac tissue is considered in isolation from surrounding tissues, the boundary condition applied is homogeneous

$$\begin{aligned}
(\boldsymbol{\sigma}_i \nabla u_i) \cdot \mathbf{n} &= 0 \\
(\boldsymbol{\sigma}_e \nabla u_e) \cdot \mathbf{n} &= 0
\end{aligned}$$

(2.14)

When external current stimuli (I_{si} and I_{se}) are applied to the intracellular and extracellular spaces, we can introduce them in expression (2.11) as $\nabla \cdot (\boldsymbol{\sigma}_i \nabla u_i) = \beta I_m - I_{si}$ for instance. The resulting bidomain model reshaped in a parabolic-elliptic form (see e.g. [108]) reads

$$
\begin{cases}
\beta C_{\mathrm{m}}\dfrac{\partial u}{\partial t} - \nabla \cdot (\boldsymbol{\sigma}_{\mathrm{i}}\nabla u) - \nabla \cdot (\boldsymbol{\sigma}_{\mathrm{i}}\nabla u_{\mathrm{e}}) + \beta I_{\mathrm{ion}} = I_{\mathrm{si}} & \text{in } Q \\[2ex]
-\nabla \cdot (\boldsymbol{\sigma}_{\mathrm{i}}\nabla u) - \nabla \cdot (\boldsymbol{\sigma}_{\mathrm{i}} + \boldsymbol{\sigma}_{\mathrm{e}})\nabla u_{\mathrm{e}} = I_{\mathrm{si}} - I_{\mathrm{se}} & \text{in } Q \\[2ex]
\boldsymbol{\sigma}_{\mathrm{i}}\nabla u \cdot \mathbf{n} + \boldsymbol{\sigma}_{\mathrm{i}}\nabla u_{\mathrm{e}} \cdot \mathbf{n} = 0, \quad \boldsymbol{\sigma}_{\mathrm{e}}\nabla u_{\mathrm{e}} \cdot \mathbf{n} = 0 & \text{on } \partial Q \\[2ex]
u(\boldsymbol{x},0) = u_0(\boldsymbol{x}) & \text{in } \Omega
\end{cases}
\tag{2.15}
$$

where $\Omega \subset \mathbb{R}^d$ (d = 2 or 3) is a bounded domain denoting the spatial region of interest and $Q = \Omega \times [0,T]$, $\partial Q = \partial \Omega \times [0,T]$ with $[0,T]$ being a fixed time interval.

A convenient way for representing the two conductivity tensors in 3D is to refer to the cardiac fibers:

$$
\boldsymbol{\sigma}_{\mathrm{i}} = \sigma_{\mathrm{il}}\mathbf{a_l}\mathbf{a_l}^T + \sigma_{\mathrm{it}}\mathbf{a_t}\mathbf{a_t}^T + \sigma_{\mathrm{in}}\mathbf{a_n}\mathbf{a_n}^T
$$
$$
\boldsymbol{\sigma}_{\mathrm{e}} = \sigma_{\mathrm{el}}\mathbf{a_l}\mathbf{a_l}^T + \sigma_{\mathrm{et}}\mathbf{a_t}\mathbf{a_t}^T + \sigma_{\mathrm{en}}\mathbf{a_n}\mathbf{a_n}^T.
$$

Here $(\mathbf{a_l}, \mathbf{a_t}, \mathbf{a_n})$ are orthonormal vector fields related to the structure of the myocardium with $\mathbf{a_l}$ along the local fiber direction, $\mathbf{a_t}$ orthogonal to the fiber direction in the fiber sheet, and $\mathbf{a_n}$ orthogonal to the sheet. The symbol σ_{il} (σ_{it}) denotes the longitudinal (tangential) intracellular conductivity while σ_{el} (σ_{et}) is the extracellular counterpart, and their values could depend on space. Sometimes we may further assume that the tissue is axial isotropic (i.e. $\sigma_{\mathrm{in}} = \sigma_{\mathrm{it}}$ and $\sigma_{\mathrm{en}} = \sigma_{\mathrm{et}}$), then we have

$$
\boldsymbol{\sigma}_{\mathrm{i}}(\boldsymbol{x}) = \sigma_{\mathrm{it}}\mathbf{I} + (\sigma_{\mathrm{il}} - \sigma_{\mathrm{it}})\mathbf{a_l}\mathbf{a_l}^T
$$
$$
\boldsymbol{\sigma}_{\mathrm{e}}(\boldsymbol{x}) = \sigma_{\mathrm{et}}\mathbf{I} + (\sigma_{\mathrm{el}} - \sigma_{\mathrm{et}})\mathbf{a_l}\mathbf{a_l}^T.
$$

Notice that u_{e} is uniquely determined by an additional condition $\int_{\Omega} u_{\mathrm{e}}(\boldsymbol{x})d\boldsymbol{x} = 0$. By applying the divergence theorem to the elliptic equation in (2.15), we require the compatibility condition for the bidomain system to be solvable: $\int_{\Omega}(I_{\mathrm{si}} - I_{\mathrm{se}})d\boldsymbol{x} = 0$.

An extensive well-posedness analysis for the system of the macroscopic bidomain model coupled with a microscopic cellular model can be found in [51, 132].

To overcome high computational costs associated with the bidomain problem, a simplified *monodomain model* has been proposed. Its derivation can be obtained in different

ways [50, 97], based upon a proportionality assumption between the intracellular and the extracellular conductivity tensors (the domains are equally anisotropic), namely assuming $\boldsymbol{\sigma}_{\mathrm{e}} = \lambda \boldsymbol{\sigma}_{\mathrm{i}}$, where λ is a constant. A formulation of the monodomain model is then obtained, by assuming $\boldsymbol{\sigma}_{\mathrm{m}} = \frac{\lambda}{1+\lambda} \boldsymbol{\sigma}_{\mathrm{i}}$ and $I_{\mathrm{app}} = \frac{\lambda}{1+\lambda} I_{\mathrm{si}} + \frac{1}{1+\lambda} I_{\mathrm{se}}$, as

$$\beta C_{\mathrm{m}} \frac{\partial u}{\partial t} - \nabla \cdot (\boldsymbol{\sigma}_{\mathrm{m}} \nabla u) + \beta I_{\mathrm{ion}} = I_{\mathrm{app}}. \tag{2.16}$$

In this "equal anisotropy ratio" case, the boundary conditions simplify to

$$\boldsymbol{\sigma}_{\mathrm{m}} \nabla u \cdot \mathbf{n} = 0.$$

Notice that the conductivity tensor $\boldsymbol{\sigma}_{\mathrm{m}}$ is the harmonic average of the intra- and extracellular ones

$$\boldsymbol{\sigma}_{\mathrm{m}} = \frac{\lambda}{1 + \lambda} \boldsymbol{\sigma}_{\mathrm{i}} = (\boldsymbol{\sigma}_{\mathrm{i}}^{-1} + \boldsymbol{\sigma}_{\mathrm{e}}^{-1})^{-1}, \tag{2.17}$$

and the stimulus I_{app} can be formulated as $I_{\mathrm{app}} = I_{\mathrm{se}}$ while taking stimuli such that $I_{\mathrm{se}} = I_{\mathrm{si}}$ or as $I_{\mathrm{app}} = \frac{\sigma_{\mathrm{il}}}{\sigma_{\mathrm{il}} + \sigma_{\mathrm{el}}} I_{\mathrm{se}}$ while taking the stimulus I_{si} as zero. These formulations are consistent with the different derivation of the monodomain model in [50]. Along with (2.16) it is called the adapted monodomain model in [20], whereas we still call it the monodomain model in this thesis.

Chapter 3

Cardiac conductivity estimation by a variational approach

In this chapter we present a variational data assimilation procedure for estimating the cardiac conductivities in ventricular tissue. This part of material is a subject of the paper [139].

3.1   Introduction

Numerical methods have been used for investigating cardiovascular diseases for at least 25 years. Starting from idealized and simplified models, computational tools have been progressively refined and applied to patient-specific geometries retrieved from medical images. However, extensive use of numerical investigations in clinical practice is still difficult for several reasons. One is the uncertainty affecting the models when applied to a specific patient. In practice, mathematical models depend on parameters that typically come from appropriate but empirical constitutive laws and their quantification for a specific patient may be problematic. For this reason, methods of *data assimilation* have been recently investigated in cardiovascular mathematics. By this we mean numerical techniques for merging available patient-specific measures (which we call our *foreground* or

patient-specific knowledge) with mathematical models (the *background* or *general knowledge*) with the twofold aim of filtering the noise in the data and reducing uncertainty in the model by a precise quantification of parameters (see e.g. [40, 134]). This chapter investigates a variational patient-specific estimation of cardiac conductivities based on available measures of cardiac potentials.

Although the importance of a precise patient-specific conductivity estimation has been recognized for a long time [119] and experimental methods based on controlled measurements after an appropriate stimulus of the tissue are quite impractical in clinics, computational methods have been investigated only in the last few years. After the work of Geselowitz [55] in 1971, experimental estimation of the intracellular and extracellular conductivities has been carried out in different ways by several groups [34, 114, 115], leading to different ranges of possible values with no common agreement on the most accurate ones. These values are reported in Table 3.1. It is worth stressing that the bidomain/monodomain model—one of the most popular mathematical models in computational electrocardiology—has been shown to be strongly sensitive to the values of conductivities and in particular to the ratio between the tangential and longitudinal extracellular conductivities [65].

A direct computational model has been explored in [125] based on a multiscale argument, where tissue-scale conductivities are computed from the current density with the simulation of cell-scale models. This computation is however based on empirical values of local conductivities. The so-called *4-leads method* requires the virtual placement of leads at a distance of the order of microns [77, 119] and a variational procedure for extracting the conductivities from a series of controlled current stimuli of the cardiac tissue. More recently, a variational approach for a reliable estimation of conductivities has been proposed in [58]. This method is based on a classical least-squares procedure. Results presented in [58] refer to 2D synthetic cases and clearly show that the variational estimate may provide accurate results, but it is computationally expensive (at least 60 solutions of the 2D bidomain system are required). Moreover, addition of more parameters

Table 3.1: Values of cardiac conductivities proposed in [58] (mS/cm).

Param ↓ \ Ref →	Clerc [34]	Roberts et al. [114]	Roberts and Scher [115]
σ_{il}	1.70	2.80	3.40
σ_{it}	0.19	0.26	0.60
σ_{el}	6.20	2.20	1.20
σ_{et}	2.40	1.30	0.80
σ_{il}/σ_{it}	8.95	10.77	5.67
σ_{el}/σ_{et}	2.58	1.69	1.50
σ_{il}/σ_{el}	0.27	1.27	2.83
σ_{it}/σ_{et}	0.08	0.20	0.75

to estimate (for instance the fiber orientation) may in fact prevent the convergence of the iterative method.

In this chapter we still use a variational procedure for the estimation of cardiac conductivities from measures of the transmembrane and extracellular potentials available at some sites of the tissue. Unlike the least-squares approach in [58], our numerical procedure is a derivative-based optimization method. The gradient of the misfit functional to minimize is computed by resorting to the adjoint equations of the bidomain system. For the challenge presented by differentiating state-dependent discontinuous terms, we use shape calculus for computing those Gâteaux differentials. We pursue both an Optimize-then-Discretize approach in small-scale simulations and a Discretize-then-Optimize approach in large-scale simulations. Results are presented in both 2D idealized and 3D real geometries. The former is used to compare our method with the results in [58]. The latter - at the best of our knowledge this is the first time variational techniques are used in 3D real geometries - to demonstrate the method in cases of clinical interest. We use also two popular ionic models to complete the bidomain system: (i) the well-known Rogers–McCulloch phenomenological model for the simple cases (including the existence analysis in Chapter 4); (ii) the minimal ionic model for more realistic cases - as an appropriate trade-off between reliability and efficiency.

We state the variational formulation of the inverse conductivity problem in Sec. 3.2.

We use a finite element discretization for the bidomain equations and the BFGS algorithm for parameter optimization (Sec. 3.3). Finally, we illustrate several numerical tests with synthetic noisy measures (Sec. 3.4). Results lead to the conclusion that the approach presented significantly improves the least-squares method [58] in terms of efficiency and provides a reliable and potentially practical method for estimating the cardiac conductivities (Sec. 3.5).

Follow-up of this work includes an investigation on possible model reduction techniques which is carried out in Chapter 5, the design of a complete estimation procedure for all patient-dependent parameters (in both healthy and pathological tissues), and an experimental validation of the estimation procedure in view of clinical applications.

3.2 Variational formulation of the inverse problem

Let the admissible domain for control variables be

$$\mathcal{C}_{\mathrm{ad}} = \{\boldsymbol{\sigma} \in \mathbf{L}^\infty(\Omega) : \boldsymbol{\sigma}(\boldsymbol{x}) \in [m, M]^{2d}, \forall \boldsymbol{x} \in \Omega\},$$

where $\mathbf{L}^\infty(\Omega) \equiv (L^\infty(\Omega))^{2d}$, $d = 3$ for 3D problems with $\boldsymbol{\sigma} = (\sigma_{\mathrm{il}}, \sigma_{\mathrm{el}}, \sigma_{\mathrm{it}}, \sigma_{\mathrm{et}}, \sigma_{\mathrm{in}}, \sigma_{\mathrm{en}})$ and $d = 2$ for 2D problems with $\boldsymbol{\sigma} = (\sigma_{\mathrm{il}}, \sigma_{\mathrm{el}}, \sigma_{\mathrm{it}}, \sigma_{\mathrm{et}})$; m and M ($m < M$) are positive constants. The problem we investigate, called the *bidomain inverse conductivity problem* (BICP), reads: find the tensor $\boldsymbol{\sigma} \in \mathcal{C}_{\mathrm{ad}}$ minimizing the misfit functional

$$\mathcal{J}(\boldsymbol{\sigma}) = \frac{1}{2} \int_0^T \int_{\Omega_{\mathrm{obs}}} (u(\boldsymbol{\sigma}) - u_{\mathrm{meas}})^2 + (u_{\mathrm{e}}(\boldsymbol{\sigma}) - u_{\mathrm{e,meas}})^2 \, d\boldsymbol{x} dt + \frac{\alpha}{2} \mathcal{R}(\boldsymbol{\sigma}) \quad (3.1)$$

subject to the bidomain equations (2.15) and a coupled ionic model (2.5). Here u_{meas} and $u_{\mathrm{e,meas}}$ denote the experimental data measured on the observation domain $\Omega_{\mathrm{obs}} \subset \Omega$. They can be obtained *in vitro* using voltage optical mapping [32], or *in vivo* by back-mapping body surface potentials [35, 99] or possibly by potential reconstruction from electrocardiogram phase analysis of standard gated SPECT [31]. The term $\mathcal{R}$ denotes a

Tikhonov-like regularization term and α is the regularization coefficient, used to weigh the impact of the regularization in the minimization procedure. For instance $\mathcal{R}$ could be taken as $\int_\Omega ||\boldsymbol{\sigma} - \hat{\boldsymbol{\sigma}}||^2 d\boldsymbol{x}$, where $\hat{\boldsymbol{\sigma}}$ is an appropriate average of available conductivity values from the literature and $||\cdot||$ denotes the Euclidean norm.

Let us consider the general abstract problem: minimize $\mathcal{J}(\sigma) = \mathcal{J}(u(\sigma), \sigma)$ with a constraint $F(u, \sigma) = 0$ (called *state equation*), where u is the state variable and σ is the control variable. We can introduce the augmented Lagrangian functional $\mathcal{L}(u, \sigma, \lambda) = \mathcal{J}(u, \sigma) - \lambda^* F(u, \sigma)$ where λ is the adjoint variable or Lagrange multiplier and $\lambda^* F(u, \sigma)$ can be regarded as a duality pairing. To find the minimum, we need to totally differentiate this functional with respect to the control variable. To this aim we formulate the *adjoint equation* $\frac{\partial \mathcal{J}}{\partial u} - \lambda^* \frac{\partial F}{\partial u} = 0$. In addition, the state equation $F(u, \sigma) = 0$ yields the *sensitivity equation* $\frac{\partial F}{\partial \sigma} + \frac{\partial F}{\partial u} \frac{du}{d\sigma} = 0$. Eventually we compute the gradient of $\mathcal{J}$ as

$$\frac{\mathcal{D}\mathcal{J}}{\mathcal{D}\sigma} = \frac{\partial \mathcal{J}}{\partial \sigma} + \frac{\partial \mathcal{J}}{\partial u}\frac{du}{d\sigma} = \frac{\partial \mathcal{J}}{\partial \sigma} + \lambda^* \frac{\partial F}{\partial u}\frac{du}{d\sigma} = \frac{\partial \mathcal{J}}{\partial \sigma} - \lambda^* \frac{\partial F}{\partial \sigma} = \frac{\partial \mathcal{L}}{\partial \sigma}.$$

Following this approach, for our BICP we introduce the Lagrangian functional

$$\mathcal{L}(u, u_\mathrm{e}, \mathbf{w}, \boldsymbol{\sigma}, p, q, \mathbf{r}) = \mathcal{J}(\boldsymbol{\sigma})$$

$$- \int_0^T \int_\Omega q(\beta C_\mathrm{m}\frac{\partial u}{\partial t} - \nabla \cdot \boldsymbol{\sigma}_\mathrm{i}\nabla u - \nabla \cdot \boldsymbol{\sigma}_\mathrm{i}\nabla u_\mathrm{e} + \beta I_\mathrm{ion}(u, \mathbf{w}) - I_\mathrm{si}) \, d\boldsymbol{x}dt$$

$$- \int_0^T \int_\Omega p(-\nabla \cdot (\boldsymbol{\sigma}_\mathrm{i} + \boldsymbol{\sigma}_\mathrm{e})\nabla u_\mathrm{e} - \nabla \cdot \boldsymbol{\sigma}_\mathrm{i}\nabla u - I_\mathrm{si} + I_\mathrm{se}) \, d\boldsymbol{x}dt$$

$$- \int_0^T \int_\Omega \mathbf{r} \cdot (\frac{d\mathbf{w}}{dt} + \mathbf{g}(u, \mathbf{w})) \, d\boldsymbol{x}dt$$

$$(3.2)$$

where $q(\boldsymbol{x}, t)$, $p(\boldsymbol{x}, t)$, and $\mathbf{r}(\boldsymbol{x}, t)$ are the Lagrange multipliers.

Setting the partial derivatives $\frac{\partial \mathcal{L}}{\partial u}, \frac{\partial \mathcal{L}}{\partial u_\mathrm{e}}$ and $\frac{\partial \mathcal{L}}{\partial \mathbf{w}}$ equal to zero, we construct the *adjoint*

equations

$$\begin{cases} -\beta C_{\mathrm{m}}\dfrac{\partial q}{\partial t} - \nabla \cdot \boldsymbol{\sigma}_{\mathrm{i}}\nabla q - \nabla \cdot \boldsymbol{\sigma}_{\mathrm{i}}\nabla p + \beta \partial_u I_{\mathrm{ion}} q + \partial_u \mathbf{g} \cdot \mathbf{r} = (u - u_{\mathrm{meas}})\chi_{\Omega_{\mathrm{obs}}} & \text{in } Q \\[2ex] -\nabla \cdot (\boldsymbol{\sigma}_{\mathrm{i}} + \boldsymbol{\sigma}_{\mathrm{e}})\nabla p - \nabla \cdot \boldsymbol{\sigma}_{\mathrm{i}}\nabla q = (u_{\mathrm{e}} - u_{\mathrm{e,meas}})\chi_{\Omega_{\mathrm{obs}}} & \text{in } Q \\[2ex] \dfrac{d\mathbf{r}}{dt} - \partial_{\mathbf{w}}\mathbf{g} \cdot \mathbf{r} - \beta \partial_{\mathbf{w}} I_{\mathrm{ion}} q = \mathbf{0} & \text{in } Q \\[2ex] \boldsymbol{\sigma}_{\mathrm{i}}\nabla p \cdot \mathbf{n} + \boldsymbol{\sigma}_{\mathrm{i}}\nabla q \cdot \mathbf{n} = 0, \ \boldsymbol{\sigma}_{\mathrm{e}}\nabla p \cdot \mathbf{n} = 0 & \text{on } \partial Q \\[2ex] q(\boldsymbol{x}, T) = 0, \quad \mathbf{r}(\boldsymbol{x}, T) = \mathbf{0} & \text{in } \Omega. \end{cases} \tag{3.3}$$

Based on the adjoint equations we get the Gâteaux derivatives of $\mathcal{J}$ as follows

$$\frac{\mathcal{D}\mathcal{J}}{\mathcal{D}\sigma_{\mathrm{ik}}} = \frac{\partial \mathcal{L}}{\partial \sigma_{\mathrm{ik}}} = -\int_0^T \mathbf{a_k}\mathbf{a_k}^T \nabla(u + u_{\mathrm{e}}) \cdot \nabla(p + q)\, dt + \frac{\alpha}{2}\frac{\partial \mathcal{R}}{\partial \sigma_{\mathrm{ik}}} \tag{3.4}$$

$$\frac{\mathcal{D}\mathcal{J}}{\mathcal{D}\sigma_{\mathrm{ek}}} = \frac{\partial \mathcal{L}}{\partial \sigma_{\mathrm{ek}}} = -\int_0^T \mathbf{a_k}\mathbf{a_k}^T \nabla u_{\mathrm{e}} \cdot \nabla p\, dt + \frac{\alpha}{2}\frac{\partial \mathcal{R}}{\partial \sigma_{\mathrm{ek}}}, \tag{3.5}$$

where k stands for $\mathrm{l}, \mathrm{t}, \mathrm{n}$.

3.3 Numerical solver

In this section, we describe the time and space discretization techniques and the linear solver for the state and adjoint equations (Sec. 3.3.1). We will refer to the minimal ionic model since it requires to address specific issues. In particular, we address our approach for differentiating state-dependent discontinuous terms (Sec. 3.3.2). At the end, we describe the optimization algorithm for the bidomain inverse conductivity problem (Sec. 3.3.3).

3.3.1 Time and space discretization

The bidomain equations take the form of a system of PDEs, describing tissue-level action potential propagation, coupled with a system of ODEs, describing cellular-level behavior,

as seen in Sec. 2.2 and 2.3. Following a quite consolidated strategy (see e.g. [56]), we decouple the global system of PDEs and ODEs with the aim of improving computational efficiency and reducing complex dependencies between variables. The time advancing scheme for the ODEs is an implicit backward Euler method. Other methods can be pursued as well [103]. For the PDEs, a semi-implicit time discretization based on the backward differentiation formula (BDF) is used.

Let Δt be the time step, hereafter we use superscript l for those variables at time $t = l\Delta t$ and superscript $l + 1$ for those variables at time $t = (l+1)\Delta t$. We assume in general the final time is T, which will be specially customized in the Discretize-then-Optimize framework (see Sec. 3.3.3), and let $L = T/\Delta t$, $t^l = l\Delta t$. The bidomain system after time discretization reads

$$
\begin{cases}
\beta C_{\mathrm{m}} \frac{\alpha_0}{\Delta t} u^{l+1} - \nabla \cdot \boldsymbol{\sigma}_{\mathrm{i}} \nabla u^{l+1} - \nabla \cdot \boldsymbol{\sigma}_{\mathrm{i}} \nabla u_{\mathrm{e}}^{l+1} \\
\qquad\qquad = I_{\mathrm{si}}^{l+1} - \beta I_{\mathrm{ion}}(\tilde{u}^{l+1}, \mathbf{w}^{l+1}) + \beta C_{\mathrm{m}} \sum_{i=1}^{s} \frac{\alpha_i}{\Delta t} u^{l+1-i} & \text{in } \Omega \\
-\nabla \cdot \boldsymbol{\sigma}_{\mathrm{i}} \nabla u^{l+1} - \nabla \cdot (\boldsymbol{\sigma}_{\mathrm{i}} + \boldsymbol{\sigma}_{\mathrm{e}}) \nabla u_{\mathrm{e}}^{l+1} = I_{\mathrm{si}}^{l+1} - I_{\mathrm{se}}^{l+1} & \text{in } \Omega \\
(\boldsymbol{\sigma}_{\mathrm{i}} \nabla u^{l+1} + \boldsymbol{\sigma}_{\mathrm{i}} \nabla u_{\mathrm{e}}^{l+1}) \cdot \mathbf{n} = 0, \quad \boldsymbol{\sigma}_{\mathrm{e}} \nabla u_{\mathrm{e}}^{l+1} \cdot \mathbf{n} = 0 & \text{on } \partial\Omega
\end{cases}
\tag{3.6}
$$

where the vector of gating variables $\mathbf{w}^{l+1}$ in the ionic model is updated by

$$
\frac{\mathbf{w}^{l+1} - \mathbf{w}^l}{\Delta t} = -\mathbf{g}(\tilde{u}^{l+1}, \mathbf{w}^{l+1})
\tag{3.7}
$$

with given initial condition on $\mathbf{w}^0$. Here α_i's are the coefficients of the BDF, and in a second order BDF particularly they have the values

$$
\alpha_0 = 3/2, \ \alpha_1 = 2, \ \alpha_2 = -1/2.
$$

The term $\tilde{u}^{l+1}$ in the nonlinear functions I_{ion} and $\mathbf{g}$ is a time extrapolation of u^{l+1} in order s formulated by standard Taylor expansion arguments: $\tilde{u}^{l+1} = \sum_{i=0}^{s-1} \beta_i u^{l-i}$. The

second-order time extrapolation, for instance, writes in general

$$\tilde{u}^{l+1} = 2u^l - u^{l-1}$$

and in particular $\tilde{u}^1 = u^0$.

Similarly, the adjoint equations after time discretization read

$$\begin{cases} \beta C_{\mathrm{m}} \frac{\alpha_0}{\Delta t} q^l - \nabla \cdot \boldsymbol{\sigma}_{\mathrm{i}} \nabla p^l - \nabla \cdot \boldsymbol{\sigma}_{\mathrm{i}} \nabla q^l = (u^l - u^l_{\mathrm{meas}}) \chi_{\Omega_{\mathrm{obs}}} \\ \qquad\qquad - \beta \partial_u I_{\mathrm{ion}}(u^l, w^l) \tilde{q}^l - \partial_u \mathbf{g}^l \cdot \mathbf{r}^l + \beta C_{\mathrm{m}} \sum\limits_{i=1}^{s} \frac{\alpha_i}{\Delta t} q^{l+i} \quad \text{in } \Omega \\ -\nabla \cdot \boldsymbol{\sigma}_{\mathrm{i}} \nabla q^l - \nabla \cdot (\boldsymbol{\sigma}_{\mathrm{i}} + \boldsymbol{\sigma}_{\mathrm{e}}) \nabla p^l = 0 \qquad\qquad\qquad\qquad\quad \text{in } \Omega \\ \boldsymbol{\sigma}_{\mathrm{e}} \nabla p^l \cdot \mathbf{n} = 0, \quad \boldsymbol{\sigma}_{\mathrm{i}} \nabla p^l \cdot \mathbf{n} + \boldsymbol{\sigma}_{\mathrm{i}} \nabla q^l \cdot \mathbf{n} = 0 \qquad\qquad\quad \text{on } \partial\Omega \end{cases} \quad (3.8)$$

where $\tilde{q}^l = \sum\limits_{i=0}^{s-1} \beta_i q^{l+1+i}$ is a time extrapolation of q^l in order s. Specially, the second-order time extrapolation writes in general $\tilde{q}^l = 2q^{l+1} - q^{l+2}$ and in particular $\tilde{q}^{L-1} = q^L$. The dual variable $\mathbf{r}^l$ is solved by

$$\frac{\mathbf{r}^{l+1} - \mathbf{r}^l}{\Delta t} = \beta \partial_{\mathbf{w}} I_{\mathrm{ion}}^l \tilde{q}^l + \partial_{\mathbf{w}} \mathbf{g} \cdot \mathbf{r}^l \qquad (3.9)$$

with "initial" condition $\mathbf{r}^L = \mathbf{0}$.

Notice that the time linearization treats the nonlinear terms in explicit, thus leading to a linear time-discrete problem. Other treatments for the nonlinear terms can be employed as well, such as the linearly implicit Rosenbrock method in [92], which are more accurate, yet computationally more demanding. For our purposes, a second order explicit scheme seems to be the best trade-off between accuracy, simplicity, computational costs and stability.

We use the finite element method (FEM) for the space discretization. Let space $H_h^1 = \mathrm{span}\{\phi_j\}_{j=1}^n \subseteq H^1$ be the finite-dimensional subspace of H^1 of piecewise linear functions, where $\{\phi_j\}_{j=1}^n$ are the generic (Lagrange) basis functions of this space. The approximated finite element solutions read $u_h(\boldsymbol{x}, t) = \sum\limits_{j=1}^n u_j(t)\phi_j(\boldsymbol{x})$, $u_{\mathrm{e},h}(\boldsymbol{x}, t) = \sum\limits_{j=1}^n u_{\mathrm{e},j}(t)\phi_j(\boldsymbol{x})$. Let

us denote by $\mathbf{M}$ the mass matrix with entries $[\mathbf{M}]_{jk} = \int_\Omega \phi_k \phi_j d\boldsymbol{x}$ and by $\mathbf{S}_\tau$ the stiffness matrices with entries $[\mathbf{S}_\tau]_{jk} = \int_\Omega \boldsymbol{\sigma}_\tau \nabla \phi_k \cdot \nabla \phi_j d\boldsymbol{x}$, where τ stands for i, e, m. For $\mathbf{u} = [u_j]$ and $\mathbf{u}_e = [u_{e,j}]$, after discretization in time and then in space, the associated algebraic bidomain system reads

$$
\begin{bmatrix} \mathbf{A_b} & \mathbf{S_i} \\ \\ \mathbf{S_i} & \mathbf{S_i} + \mathbf{S_e} \end{bmatrix} \begin{bmatrix} \mathbf{u}^{l+1} \\ \\ \mathbf{u}_e^{l+1} \end{bmatrix} = \begin{bmatrix} \mathbf{b_1}^{l+1} \\ \\ \mathbf{b_2}^{l+1} \end{bmatrix}, \tag{3.10}
$$

where $\mathbf{A_b} = \beta C_\mathrm{m} \frac{\alpha_0}{\Delta t} \mathbf{M} + \mathbf{S_i}$ and the right-hand side writes

$$
\mathbf{b_1}^{l+1} = \left[\langle I_\mathrm{si}^{l+1} - \beta I_\mathrm{ion}(\tilde{u}^{l+1}, \mathbf{w}^{l+1}), \phi_j \rangle_{L^2} \right] + \beta C_\mathrm{m} \mathbf{M} \sum_{i=1}^s \frac{\alpha_i}{\Delta t} \mathbf{u}^{l+1-i}
$$

$$
\mathbf{b_2}^{l+1} = \left[\langle I_\mathrm{si}^{l+1} - I_\mathrm{se}^{l+1}, \phi_j \rangle_{L^2} \right].
$$

Similarly, the algebraic form of the adjoint equations reads

$$
\begin{bmatrix} \mathbf{A_b} & \mathbf{S_i} \\ \\ \mathbf{S_i} & \mathbf{S_i} + \mathbf{S_e} \end{bmatrix} \begin{bmatrix} \mathbf{q}^l \\ \\ \mathbf{p}^l \end{bmatrix} = \begin{bmatrix} \mathbf{d_1}^l \\ \\ \mathbf{d_2}^l \end{bmatrix}, \tag{3.11}
$$

and the right-hand side is formulated as

$$
\mathbf{d_1}^l = [\langle q_*^l, \phi_j \rangle_{L^2}] + [\langle (u^l - u_\mathrm{meas}^l) \chi_{\Omega_\mathrm{obs}}, \phi_j \rangle_{L^2}] + \beta C_\mathrm{m} \mathbf{M} \sum_{i=1}^s \frac{\alpha_i}{\Delta t} \mathbf{q}^{l+i}
$$

$$
\mathbf{d_2}^l = [\langle (u_e^l - u_\mathrm{e,meas}^l) \chi_{\Omega_\mathrm{obs}}, \phi_j \rangle_{L^2}].
$$

where $q_*^l = -\beta \partial_u I_\mathrm{ion}^l \tilde{q}^l - \partial_u \mathbf{g}^l \cdot \mathbf{r}^l$.

Since $\mathbf{u}_e$ is unique up to a constant, the kernel of the algebraic matrix in (3.10) is $\mathrm{span}\{[\mathbf{0}, \mathbf{1}]^T\}$. The singular system (3.10) is solved by an iterative method, in particular the GMRESR method, which is a reliable strategy for elliptic problems with homogeneous Neumann boundary conditions [16]. The GMRESR algorithm is implemented in

the Trilinos package (`www.trilinos.org`). A mass lumping technique ([109], sec. 11.5) is employed for stabilization of the reactive dominating terms presented after time discretization. After solving the bidomain system (3.10), we force the average of $\mathbf{u}_e$ to be zero at each time iteration.

It is worth stressing that the efficient solution and preconditioning of the bidomain equations have been a topic of interest in many papers (see e.g. [56], [101], [106]). Since this is not the main focus here, we resort to a standard ILU preconditioner without entering in further detail.

3.3.2 Computation of derivatives of discontinuous terms

When we adopt the minimal ionic model (or any other biophysics-based models like the TNNP model [131]), the terms $\partial_u I_{\text{ion}}^l$ and $\partial_u \mathbf{g}^l$ in q_*^l contain Gâteaux differentials $DH(u-c)$ of functionals involving $H(u-c)$, where $c \in \mathbb{R}$ is a constant. More specifically, for convenience of the reader we formally rewrite the minimal ionic model as

$$I_{\text{ion}}(u, [v, w, s]^T) = 85.7 C_{\text{m}}(J_{\text{fi}} + J_{\text{so}} + J_{\text{si}})$$

$$J_{\text{fi}}(u, v) = J_{\text{fiH1}}(u, v) H(u - \hat{\theta}_v)$$

$$J_{\text{so}}(u) = J_{\text{soH1}}(u) H(u - \hat{\theta}_o) + J_{\text{soH2}}(u) H(u - \hat{\theta}_w) + J_{\text{soH0}}(u)$$

$$J_{\text{si}}(u, w, s) = J_{\text{siH1}}(w, s) H(u - \hat{\theta}_w)$$

$$\mathbf{g}(u, [v, w, s]^T) = \begin{bmatrix} -g_{1\text{H1}}(v) H(u - \hat{\theta}_v^-) - g_{1\text{H2}}(v) H(u - \hat{\theta}_v) - g_{1\text{H0}}(v) \\ \\ -g_{2\text{H1}}(u) H(u - \hat{\theta}_o) - g_{2\text{H2}}(u, w) H(u - \hat{\theta}_w) - g_{2\text{H0}}(u, w) \\ \\ -g_{3\text{H1}}(u, s) H(u - \hat{\theta}_w) - g_{3\text{H0}}(u, s) \end{bmatrix}$$

where $\hat{\theta}_* = 85.7 \theta_* - 84$ in the above functions, and the terms multiplied by $H(u-c)$ such as J_{fiH1} and $g_{1\text{H1}}$ are smooth functions of the state variables u, v, w, s. Their expressions

are listed below.

$$J_{\text{fiH1}}(u, v) = -v(u - \hat{\theta}_v)(\hat{u}_u - u)/(85.7^2 \tau_{fi})$$

$$J_{\text{soH1}}(u) = (u - \hat{u}_o)(1/\tau_{o2} - 1/\tau_{o1})/85.7$$

$$J_{\text{soH2}}(u) = \{\tau_{so1} + \tfrac{1}{2}(\tau_{so2} - \tau_{so1})[1 + \tanh(k_{so}(\frac{u + 84}{85.7} - u_{so}))]\}^{-1} - (u - \hat{u}_o)/(85.7\tau_{o2})$$

$$J_{\text{soH0}}(u) = (u - \hat{u}_o)/(85.7\tau_{o1})$$

$$J_{\text{siH1}}(w, s) = -ws/\tau_{\text{si}}$$

$$g_{1\text{H1}}(v) = -v/\tau_{v2}^- - (1 - v)/\tau_{v1}^-$$

$$g_{1\text{H2}}(v) = -v/\tau_v^+ + v/\tau_{v2}^-$$

$$g_{1\text{H0}}(v) = (1 - v)/\tau_{v1}^-$$

$$g_{2\text{H1}}(u) = \frac{w_\infty^* - 1 + (u + 84)/(85.7\tau_{w\infty})}{\tau_{w1}^- + \tfrac{1}{2}(\tau_{w2}^- - \tau_{w1}^-)[1 + \tanh(k_w^-(\frac{u+84}{85.7} - u_w^-))]}$$

$$g_{2\text{H2}}(u, w) = -\frac{w}{\tau_w^+} - \frac{w_\infty^* - w}{\tau_{w1}^- + \tfrac{1}{2}(\tau_{w2}^- - \tau_{w1}^-)[1 + \tanh(k_w^-(\frac{u+84}{85.7} - u_w^-))]}$$

$$g_{2\text{H0}}(u, w) = \frac{1 - (u + 84)/(85.7\tau_{w\infty}) - w}{\tau_{w1}^- + \tfrac{1}{2}(\tau_{w2}^- - \tau_{w1}^-)[1 + \tanh(k_w^-(\frac{u+84}{85.7} - u_w^-))]}$$

$$g_{3\text{H1}}(u, s) = [\tfrac{1}{2}(1 + \tanh(k_s(\frac{u+84}{85.7} - u_s))) - s](1/\tau_{s2} - 1/\tau_{s1})$$

$$g_{3\text{H0}}(u, s) = [\tfrac{1}{2}(1 + \tanh(k_s(\frac{u+84}{85.7} - u_s))) - s]/\tau_{s1}.$$

When solving the adjoint equations, we need to compute

$$\langle q_*^l, \phi_i \rangle_{L^2} = \langle -\beta \partial_u I_{\text{ion}}^l \tilde{q}^l - \partial_u \mathbf{g}^l \cdot \mathbf{r}^l, \phi_i \rangle_{L^2}$$

$$= \langle F_1, \phi_i \rangle_{L^2} + \langle F_2 DH(u - \hat{\theta}_v), \phi_i \rangle_{L^2} + \langle F_3 DH(u - \hat{\theta}_o), \phi_i \rangle_{L^2}$$

$$+ \langle F_4 DH(u - \hat{\theta}_w), \phi_i \rangle_{L^2} + \langle F_5 DH(u - \hat{\theta}_v^-), \phi_i \rangle_{L^2} \qquad (3.12)$$

with $\mathbf{r}^l$ and F_1 through F_5 are detailed as

$$\mathbf{r}^l = [r_1^l, r_2^l, r_3^l]^T$$

$$F_1 = -85.7\beta C_{\mathrm{m}}\tilde{q}^l(\partial_u J_{\mathrm{fiH1}}H(u-\hat{\theta}_v) + \partial_u J_{\mathrm{soH1}}H(u-\hat{\theta}_o) + \partial_u J_{\mathrm{soH2}}H(u-\hat{\theta}_w)$$

$$+\partial_u J_{\mathrm{soH0}}) + r_2^l(\partial_u g_{\mathrm{2H1}}H(u-\hat{\theta}_o) + \partial_u g_{\mathrm{2H2}}H(u-\hat{\theta}_w) + \partial_u g_{\mathrm{2H0}})$$

$$+r_3^l(\partial_u g_{\mathrm{3H1}}H(u-\hat{\theta}_w) + \partial_u g_{\mathrm{3H0}})$$

$$F_2 = -85.7\beta C_{\mathrm{m}}\tilde{q}^l J_{\mathrm{fiH1}} + r_1^l g_{\mathrm{1H2}}$$

$$F_3 = -85.7\beta C_{\mathrm{m}}\tilde{q}^l J_{\mathrm{soH1}} + r_2^l g_{\mathrm{2H1}}$$

$$F_4 = -85.7\beta C_{\mathrm{m}}\tilde{q}^l(J_{\mathrm{soH2}} + J_{\mathrm{siH1}}) + r_2^l g_{\mathrm{2H2}} + r_3^l g_{\mathrm{3H1}}$$

$$F_5 = r_1^l g_{\mathrm{1H1}},$$

where the evaluation on state variables u, v, w, s is at time $t = t^l$, but we drop the superscript l here to keep the notations simple.

Regularization of the discontinuities with a smooth approximation like a classical $H(u) \approx \frac{1}{2}(1 + \tanh(u/\varepsilon))$ (where ε is a small number) may prevent the convergence of the inverse solver. We tested this statement by a simulation performed on a slab as described in Sec. 3.4.2. For the sake of clarity, we report here the result in Figure 3.1, which shows that regularization inhibits the convergence to the exact values of conductivity. This non-convergence argument is consistent with the statements in [43] and [92].

For this reason, we need to follow rigorous procedures where Gâteaux differential $DH(u - c)$ is computed with great accuracy. As a general differentiation form in expression (3.12), $\langle b(\boldsymbol{x})DH(u - c), \varphi\rangle_{L^2}$ can be computed through

$$\langle b(\boldsymbol{x})DH(u - c), \varphi\rangle_{L^2} = \int_\Omega b(\boldsymbol{x})D_\varphi H(u - c)d\boldsymbol{x} = D_\varphi j_{b,c}(u), \qquad (3.13)$$

where we denote

$$j_{b,c}(u) = \int_\Omega b(\boldsymbol{x})H(u(\boldsymbol{x}) - c)d\boldsymbol{x}$$
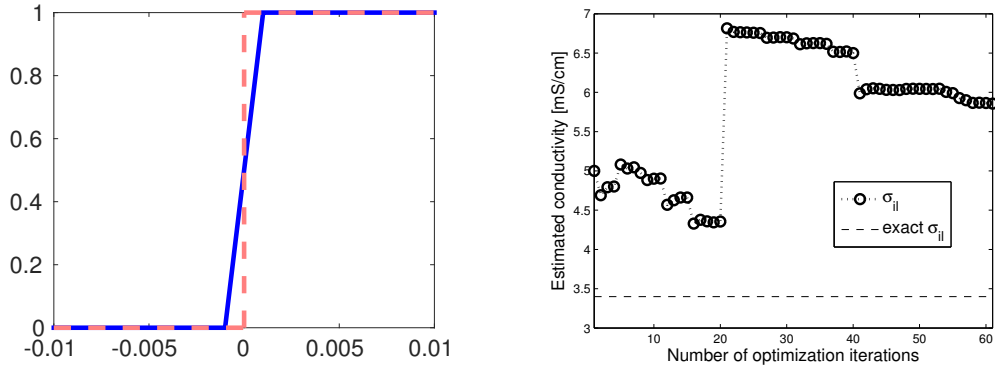
Figure 3.1: Left: Regularization of the step function (dashed) by $H(u) \approx \frac{1}{2}(1 + \tanh(u/10^{-4}))$. Right: History of conductivity estimation using the minimal ionic model with this regularization. The simulation was performed on a slab as described in Sec. 3.4.2. Regularization prevents the convergence to the exact value (identified by the dashed line).

and its Gâteaux derivative in the direction of φ reads

$$D_\varphi j_{b,c}(u) = \lim_{t \to 0} \frac{1}{t}(j_{b,c}(u + t\varphi) - j_{b,c}(u)) = \lim_{t \to 0} \frac{1}{t}\left(\int_{\Omega_t(c)} b(\boldsymbol{x})d\boldsymbol{x} - \int_{\Omega_0(c)} b(\boldsymbol{x})d\boldsymbol{x}\right)$$

with $\Omega_t(c) = \{\boldsymbol{x} : u(\boldsymbol{x}) + t\varphi(\boldsymbol{x}) - c \geq 0\}$.

This suggests to treat $D_\varphi j_{b,c}(u)$ as a shape derivative of $j_{b,c}(u)$ and take advantage of the velocity method from shape optimization [39]. We follow the result by Nagaiah et al. in a related work and provide a proof with slightly refined derivation as follows.

Proposition ([92], prop. 4.1). The Gâteaux derivative of $j_{b,c}(u)$ in the direction φ can be computed as

$$D_\varphi j_{b,c}(u) = \int_{\Gamma_0(c)} \frac{b(\boldsymbol{x})\varphi(\boldsymbol{x})}{|\nabla u(\boldsymbol{x}) \cdot \mathbf{n}|}d\Gamma \tag{3.14}$$

where $\mathbf{n}$ denotes the outward unit normal to the domain $\{\boldsymbol{x} : u(\boldsymbol{x}) \geq c\}$ and we assume that $\nabla u(\boldsymbol{x}) \neq 0$ in a neighbourhood of $\Gamma_0(c) = \{\boldsymbol{x} : u(\boldsymbol{x}) = c\}$.

Proof. The evolution of the boundaries $\Gamma_t(c) = \{\boldsymbol{x} : u(\boldsymbol{x}) + t\varphi(\boldsymbol{x}) - c = 0\}$ of $\Omega_t(c)$ satisfies (by differentiating the equation in $\Gamma_t(c)$)

$$\nabla u(\boldsymbol{x}(t)) \cdot \frac{d\boldsymbol{x}}{dt} + \varphi(\boldsymbol{x}(t)) + t\nabla\varphi(\boldsymbol{x}(t)) \cdot \frac{d\boldsymbol{x}}{dt} = 0. \tag{3.15}$$

To apply the velocity method, we assume that $t \rightarrow \boldsymbol{x}(t)$—which corresponds to a family of transformations on Ω—is determined by the differential equation

$$\frac{d\boldsymbol{x}}{dt} = \mathbf{V}(t, \boldsymbol{x}(t))$$

with velocity fields $\mathbf{V}(t)(\boldsymbol{x}) := \mathbf{V}(t, \boldsymbol{x}(t))$. By the theorem in [39] pg. 483 or [38] pg. 348, the shape derivative $D_\varphi j_{b,c}(u)$ of $j_{b,c}(u)$ in the direction φ can be computed by

$$D_\varphi j_{b,c}(u) = \int_{\Gamma_0(c)} b(\boldsymbol{x}) \mathbf{V}(0) \cdot \mathbf{n} d\Gamma \tag{3.16}$$

where we simply use $\boldsymbol{x}$ denoting $\boldsymbol{x}(t)$ on $\Gamma_0(c)$ for $t = 0$.

In the particular case when the boundaries $\Gamma_t(c)$ with varying c are level sets, the velocity is along the normal direction. At $t = 0$, the normal direction of $\Omega_0(c)$ is given by $\mathbf{n} = \frac{-\nabla u(\boldsymbol{x})}{|\nabla u(\boldsymbol{x})|}$, so we can take $\mathbf{V}(0) = V(\boldsymbol{x})\frac{-\nabla u(\boldsymbol{x})}{|\nabla u(\boldsymbol{x})|}$ where V is a scalar-valued function that can be determined from (3.15). Setting $t = 0$ in (3.15), we have

$$V(\boldsymbol{x})\nabla u(\boldsymbol{x}) \cdot \frac{-\nabla u(\boldsymbol{x})}{|\nabla u(\boldsymbol{x})|} + \varphi(\boldsymbol{x}) = 0.$$

Therefore $\mathbf{V}(0) \cdot \mathbf{n} = V(\boldsymbol{x}) = \frac{\varphi(\boldsymbol{x})}{|\nabla u(\boldsymbol{x})|}$. Finally, the shape derivative is given by

$$D_\varphi j_{b,c}(u) = \int_{\Gamma_0(c)} \frac{b(\boldsymbol{x})\varphi(\boldsymbol{x})}{|\nabla u(\boldsymbol{x})|} d\Gamma. \tag{3.17}$$

Since the tangential component of u on $\Gamma_0(c)$ is zero, the shape derivative can be expressed equivalently in the form (3.14). □

Following (3.13) and (3.14) we then compute in (3.12)

$$\langle F_2 DH(u - \hat{\theta}_v), \phi_i \rangle_{L^2} = D_{\phi_i} j_{F_2, \hat{\theta}_v}(u) = \int_{\Gamma_0(\hat{\theta}_v)} \frac{F_2(\boldsymbol{x})\phi_i(\boldsymbol{x})}{|\nabla u(\boldsymbol{x}) \cdot \mathbf{n}|} d\Gamma$$

and similarly we can compute the other terms involving $DH(u - c)$.

In practice, when working on a (linear) finite element grid, this computation requires
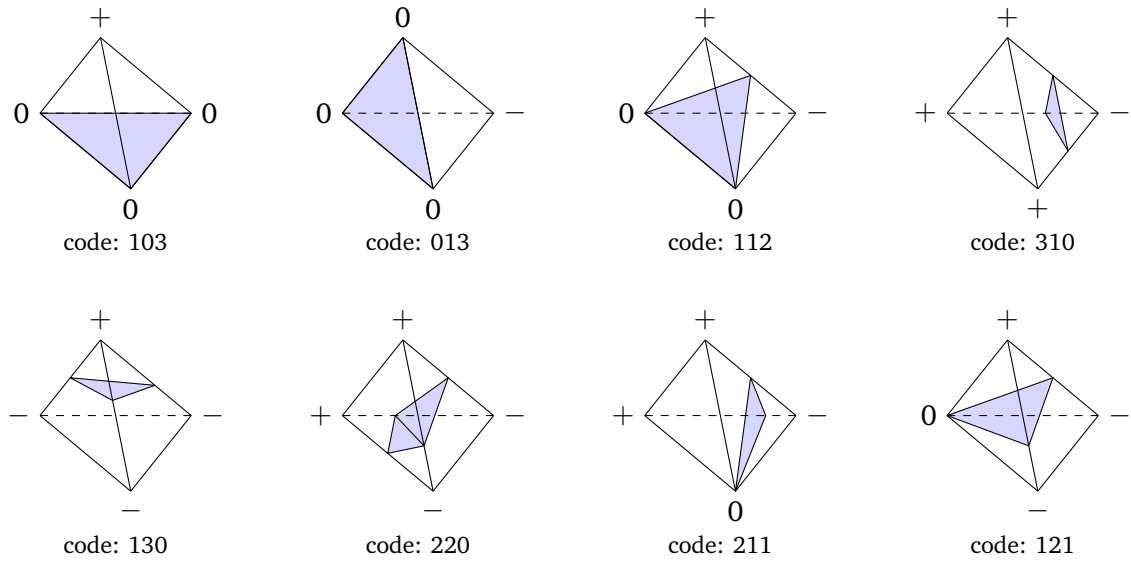
Figure 3.2: Triangle detection of iso-surfaces in different cases.

the detection of the iso-surfaces $\Gamma_0(c)$. To this aim we resort to the *marching tetrahedron method*. At each time step we detect the iso-surfaces in each element of Ω. These are represented by linear functions fitting the piecewise linear approximation. We then compute the integral on these surfaces element-wise. More specifically, we introduce a 3-digit code to identify all the different possible cases, as reported in Figure 3.2. The first digit represents the number of nodes in the current tetrahedron with positive iso-level (i.e. $u(\boldsymbol{x}) - c > 0$), the second digit represents the number of nodes with negative iso-level (i.e. $u(\boldsymbol{x}) - c < 0$), and third digit represents the number of nodes with zero iso-level (i.e. $u(\boldsymbol{x}) - c = 0$).

Integration is carried out on the reference 2D element as illustrated in Figure 3.3. On each iso-surface triangle T, the integral is computed by mapping it to a reference $\hat{T}$ triangle

$$
\int_T \frac{b(\boldsymbol{x})}{|\nabla u(\boldsymbol{x}) \cdot \mathbf{n}|} d\Gamma = \int_{\hat{T}} \frac{b(\Psi(\hat{\boldsymbol{x}}))}{|\nabla u(\Psi(\hat{\boldsymbol{x}}))|} \sqrt{det(g_{\hat{\xi}\hat{\eta}})} d\hat{\xi} d\hat{\eta} = \sum_{ig} \frac{b(\Psi(\hat{\boldsymbol{x}}_{ig}))}{|\nabla u(\boldsymbol{x}_{ig})|} \sqrt{det(g_{\hat{\xi}\hat{\eta}})|_{\hat{\boldsymbol{x}}_{ig}}} w_{ig}
$$
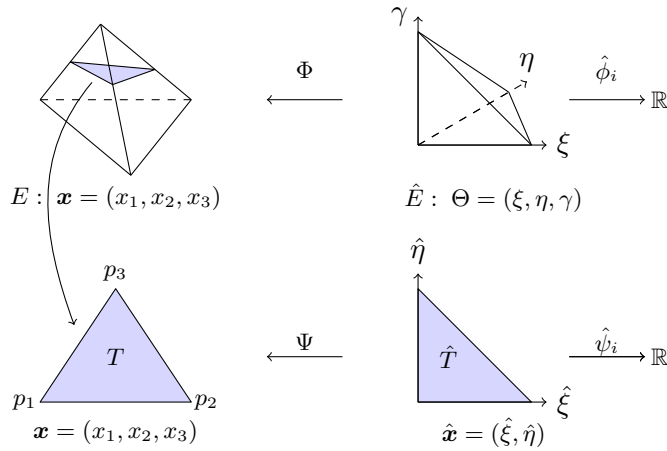
Figure 3.3: Coordinate transformation.

where

$$\nabla u(\boldsymbol{x}_{ig}) = \sum_{i=1}^{n} u_i \nabla \phi_i(\boldsymbol{x}_{ig}) = \sum_{i=1}^{n} u_i J^{-t}(\Theta_{ig}) \nabla \hat{\phi}_i(\Theta_{ig})$$

$$g_{\hat{\xi}\hat{\eta}} = \frac{\partial \Psi}{\partial \hat{\xi}} \cdot \frac{\partial \Psi}{\partial \hat{\eta}} = \sum_{i,j} p_i^T p_j \frac{\partial \hat{\psi}_i}{\partial \hat{\xi}} \cdot \frac{\partial \hat{\psi}_j}{\partial \hat{\eta}}$$

J is the Jacobian matrix of Φ, ig is the index for the quadrature rule and w_{ig} is the weight in the quadrature rule.

3.3.3   Interplay between optimization and time discretization

Given optimization time step dt_{opt} that we will specify later, we define

$$\mathcal{J}^i(\boldsymbol{\sigma}) = \frac{1}{2} \int_{t^0 + i dt_{\mathrm{opt}}}^{t^0 + (i+1) dt_{\mathrm{opt}}} \int_{\Omega_{\mathrm{obs}}} (u(\boldsymbol{\sigma}) - u_{\mathrm{meas}})^2 + (u_{\mathrm{e}}(\boldsymbol{\sigma}) - u_{\mathrm{e,meas}})^2 \, d\boldsymbol{x} dt + \frac{\alpha}{2} \mathcal{R}(\boldsymbol{\sigma})$$

where $i = 0, \cdots, (\frac{T}{dt_{\mathrm{opt}}} - 1)$. The optimization algorithm for solving the bidomain inverse conductivity problem is described in Algorithm 1, in which $\mathcal{Q}$ denotes the queue of estimates we find for the conductivities along the procedure.

More precisely in Algorithm 1 the misfit function $\mathcal{J}^i(\boldsymbol{\sigma}^k)$ and its gradient $\nabla \mathcal{J}^i(\boldsymbol{\sigma}^k)$ are computed through the following scheme

---

Algorithm 1 BFGS Optimization

Input: initial guess $\boldsymbol{\sigma}^0$, optimization step dt_{opt}, average number a
Output: estimated conductivity values
 1: Initialize queue $\mathcal{Q} \leftarrow \{\}$
 2: **for** $i = 0, \cdots, (\frac{T}{dt_{\mathrm{opt}}} - 1)$ **do**
 3:     Initialize inverse Hessian $\boldsymbol{H}_0 \leftarrow \frac{1}{||\nabla \mathcal{J}^i(\boldsymbol{\sigma}^0)||}\mathbf{I}$
 4:     $k \leftarrow 0$
 5:     **while** stopping criterion not satisfied **do**
 6:         Compute search direction $\boldsymbol{v}^k = -\boldsymbol{H}_k \nabla \mathcal{J}^i(\boldsymbol{\sigma}^k)$
 7:         Set $\boldsymbol{\sigma}^{k+1} = \boldsymbol{\sigma}^k + \gamma_k \boldsymbol{v}^k$ with $\gamma_k \in (0, \infty)$ computed from a line search
 8:         Define $\mathbf{s}_k = \boldsymbol{\sigma}^{k+1} - \boldsymbol{\sigma}^k$, $\mathbf{y}_k = \nabla \mathcal{J}^i(\boldsymbol{\sigma}^{k+1}) - \nabla \mathcal{J}^i(\boldsymbol{\sigma}^k)$, $\rho_k = \frac{1}{\mathbf{y}_k^T \mathbf{s}_k}$
 9:         Update the inverse Hessian
               $\boldsymbol{H}_{k+1} = (\mathbf{I} - \rho_k \mathbf{s}_k \mathbf{y}_k^T)\mathbf{H}_k(\mathbf{I} - \rho_k \mathbf{y}_k \mathbf{s}_k^T) + \rho_k \mathbf{s}_k \mathbf{s}_k^T$ (BFGS [98])
10:         $k \leftarrow k + 1$
11:     **end while**
12:     Push $\boldsymbol{\sigma}^k$ into $\mathcal{Q}$; pop $\mathcal{Q}$ if $i \geq a$
13:     $\boldsymbol{\sigma}^0 \leftarrow \sum\limits_{\boldsymbol{\sigma} \in \mathcal{Q}} \boldsymbol{\sigma}/a$
14: **end for**
15: **return** $\boldsymbol{\sigma}^0$

---

1. Solve (u, u_{e}) from $t^0 + i dt_{\mathrm{opt}}$ to $t^0 + (i+1)dt_{\mathrm{opt}}$ with $\boldsymbol{\sigma}^k$; Store (u, u_{e})

2. Evaluate the misfit function $\mathcal{J}^i(\boldsymbol{\sigma}^k)$

3. Solve (q, p) from $t^0 + (i+1)dt_{\mathrm{opt}}$ to $t^0 + i dt_{\mathrm{opt}}$ with $\boldsymbol{\sigma}^k$ and stored (u, u_{e})

4. Compute $\nabla \mathcal{J}^i(\boldsymbol{\sigma}^k)$ by

$$\frac{\mathcal{D}\mathcal{J}^i}{\mathcal{D}\sigma_{\mathrm{ik}}} = -\int_{t^0+idt_{\mathrm{opt}}}^{t^0+(i+1)dt_{\mathrm{opt}}} \mathbf{a_k}\mathbf{a_k}^T \nabla(u + u_{\mathrm{e}}) \cdot \nabla(p + q) \, dt + \frac{\alpha}{2}\frac{\partial \mathcal{R}}{\partial \sigma_{\mathrm{ik}}}$$

$$\frac{\mathcal{D}\mathcal{J}^i}{\mathcal{D}\sigma_{\mathrm{ek}}} = -\int_{t^0+idt_{\mathrm{opt}}}^{t^0+(i+1)dt_{\mathrm{opt}}} \mathbf{a_k}\mathbf{a_k}^T \nabla u_{\mathrm{e}} \cdot \nabla p \, dt + \frac{\alpha}{2}\frac{\partial \mathcal{R}}{\partial \sigma_{\mathrm{ek}}},$$

where k stands for l, t, n.

The line search in Step 7 of Algorithm 1 is based on a cubic interpolation of the misfit function and on the Armijo condition ([98]). The curvature condition (see [98] p.33) is not adopted since they use derivatives, as such they are more expensive to compute than function values. In reality, under the Armijo condition alone, the line search performs

well enough with a maximum iteration number two.

Here, we summarized all the possible combinations between the discretization and the optimization steps we considered. In particular, we consider three possible approaches.

To be specific, while performing simulations on relatively coarse meshes, we use an *Optimize-then-Discretize* (OD) scheme. This means that we formulate the optimization procedure at the continuous level ($dt_{\mathrm{opt}} = T$ and hence $a = 1$) and then we discretize the problem. This is the most accurate and efficient way in a small-scale simulation. However, it is not feasible for large-scale optimization due to the requirement on memory size. The reason is that we need to solve a backward-in-time dual problem, which is demanding on the storage of the bidomain solution over the entire time interval of interest.

While performing simulations on fine meshes, two alternative schemes are considered for memory saving, *checkpointing* and *Discretize-then-Optimize* (DO). In the former, we perform again the optimization procedure globally on the time interval T and hence we set $a = 1$. To solve the adjoint system, we first solve the bidomain system once. However, state variables are stored only at some checking points equispaced with step dt_{check}, which is taken to be $\geq 20\Delta t$. Then while solving the adjoint system, the bidomain solver runs again in each time interval of length dt_{check}, using initial conditions from stored checkpoints. Finally the dual solver on this time interval is applied.

In the Discretize-then-Optimize scheme, we perform the optimization procedure over every shorter time slot of length dt_{opt}, instead of the full time interval T. Estimated conductivity tensors in general change at each time step dt_{opt}. In order to smoothen the convergence sequence, we take an average of the estimated values in the previous time slots, and use the average as an initial guess for the optimization over next time slot, as was done in [14]. This averaging step helps lower the risk that a possible bad estimate in previous time slot could significantly bias the following ones. In particular, we set empirically $a = 5$.

3.4 Numerical results

Similar to the experimental assumption in [115], we hereby assume that the conductivity parameters are uniform in the domain Ω and the tissue is axial isotropic (i.e. $\sigma_{\text{in}} = \sigma_{\text{it}}$ and $\sigma_{\text{en}} = \sigma_{\text{et}}$). We denote $\boldsymbol{\sigma}_{\text{exact}} = (\sigma_{\text{il}}, \sigma_{\text{el}}, \sigma_{\text{it}}, \sigma_{\text{et}})$.

Two sets of numerical tests are presented in this section. The first one is intended to compare our approach with tests in the literature, to assess the performance of our method. This test is therefore in 2D, as taken from the literature. For this test, we implemented the bidomain solver, coupled with the Rogers–McCulloch model, and its dual in the well-known FreemFem++ environment [60].

The 3D test cases are then presented to demonstrate that the method can run on real geometries, beyond the proof-of-concept stage. For these cases, we needed a more effective software environment and we resorted to LifeV, an object oriented C++ finite element library developed by different groups worldwide [100]. In these tests, we used also geometries retrieved from real patients and in particular from SPECT images, as we will detail later on. For the sake of reliability and efficiency the minimal ionic model was used.

In Tests 1–5 conductivities were assumed to be constant (so clearly belonging to $\mathcal{C}_{\text{ad}}$), as it is reasonable for a healthy heart. In Test 6 we assumed a piecewise constant conductivities (again clearly in $\mathcal{C}_{\text{ad}}$), as we may have in a pathological case with a region - called "scar" - featuring altered values and strongly affecting the regular potential dynamics.

3.4.1 Two-dimensional test

We present a 2D test inspired by [58]. The computational domain was $\Omega = [0, 1] \times [0, 1] \subset \mathbb{R}^2$ of size 1 cm^2. The sites for measurements were arranged into an array over the tissue domain, which consisted of 6×6 electrodes with spacing of 1.667 mm. The experimental mean conductivity values were taken as $\hat{\boldsymbol{\sigma}} = (2.63, 3.2, 0.35, 1.5)$. Following [58], a constant fibre angle was chosen as $\theta = -48°$. In the test, four stimuli of $I_{\text{si}} = I_{\text{se}} = 10^5 \mu\text{A/cm}^3$ were applied in the domain for a duration of 1 ms. Synthetic data was
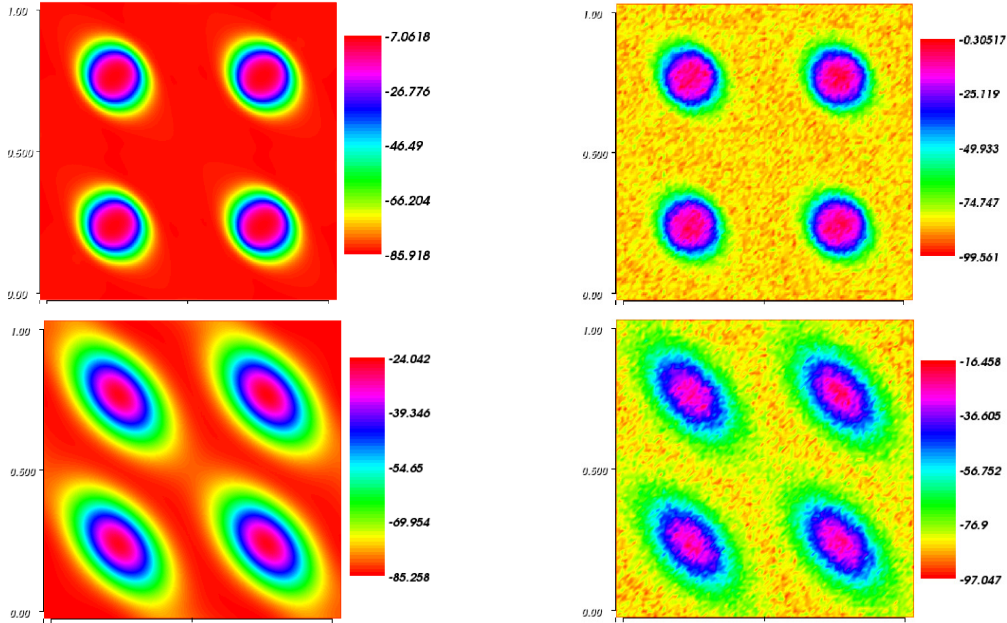
Figure 3.4: Upper left: u_{meas} at $t = 2$ ms. Lower left: u_{meas} at $t = 12$ ms. Upper right: u_{meas} at $t = 2$ ms with 15% noise. Lower right: u_{meas} at $t = 12$ ms with 15% noise

Table 3.2: 2D test on a square: 51 nodes on each boundary, $\alpha = 10^{-5}, T = 25$ ms, $\Delta t = 0.025$ ms, and $dt_{\text{snap}} = 0.5$ ms. $\boldsymbol{\sigma}_{\text{exact}} = (2.8, 2.2, 0.26, 1.3)$.

noise	0%	10%	15%
$\sigma_{\text{il}} \mid e_{\text{il}}$	2.75040 | 0.04960	2.72529 | 0.07471	2.71204 | 0.08796
$\sigma_{\text{el}} \mid e_{\text{el}}$	2.22046 | 0.02046	2.23888 | 0.03888	2.24965 | 0.04965
$\sigma_{\text{it}} \mid e_{\text{it}}$	0.20800 | 0.05200	0.21023 | 0.04977	0.21134 | 0.04866
$\sigma_{\text{et}} \mid e_{\text{et}}$	1.31297 | 0.01297	1.32505 | 0.02505	1.33751 | 0.03751
Initial $\mathcal{J}$	0.442516	0.457430	0.477920
Final $\mathcal{J}$	0.0016164	0.0187802	0.0403941
# fwd | bwd	18 | 16	21 | 18	19 | 18

generated with the conductivity parameters $\boldsymbol{\sigma}_{\text{exact}} = (2.8, 2.2, 0.26, 1.3)$. The stopping criterion used in the BFGS algorithm was $\|\nabla \mathcal{J}(\boldsymbol{\sigma}^k)\| < 10^{-6}$. To compare our results with [58], the noise added to the synthetic data at each time step had a Gaussian normal distribution with a zero mean, and its standard deviation was $(\sqrt{2}/2) \cdot 33p$, where p is the percentage of noise. The synthetic measure of transmembrane potential is shown in Figure 3.4.

Test 1: Accuracy and efficiency check. The space discretization method for generating
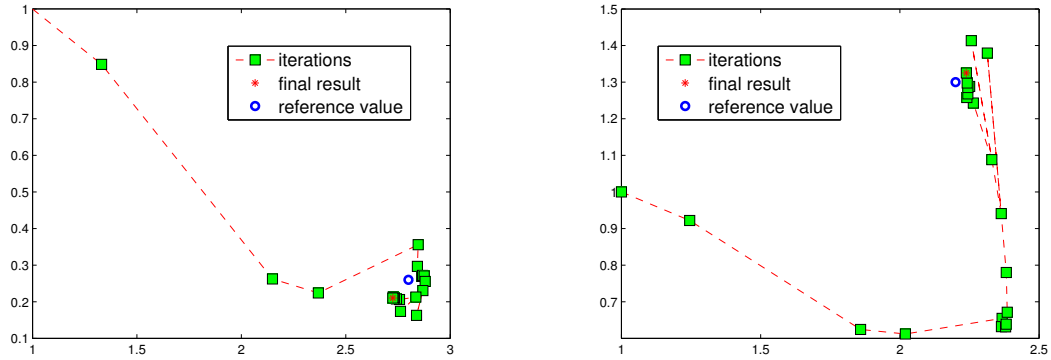
Figure 3.5: Left: Iterations for $(\sigma_{\mathrm{il}}, \sigma_{\mathrm{it}})$;   Right: Iterations for $(\sigma_{\mathrm{el}}, \sigma_{\mathrm{et}})$

measurement data was FEM P2 with 251 nodes on each boundary, the simulation time step was $\Delta t = 0.0025$ ms, and the time step dt_{snap} postulated between two measurements was 0.5 ms. For the forward problem during the optimization procedure, we used FEM P1 with 51 nodes on each boundary and $\Delta t = 0.025$ ms. By selecting two different discretization schemes we prevent any "inverse crime", since the approximation for solving the inverse problem is different from the one for generating the data.

Simulation with each searched value $\boldsymbol{\sigma}$ was run for $T = 25$ ms. The initial guess was $\boldsymbol{\sigma}_{\mathrm{initial}} = (1, 1, 1, 1)$ and the result is shown in Table 3.2. Quantities e refer to the corresponding error $|\sigma_{\mathrm{estimated}} - \sigma_{\mathrm{exact}}|$. From the table we can see, with 15% noisy data, the final estimate obtained features an error (0.08796, 0.04965, 0.04866, 0.03751). Relative to $\|\boldsymbol{\sigma}_{\mathrm{exact}}\|_\infty = 2.8$ the error is (3.14%, 1.77%, 1.74%, 1.34%). The numbers of solves of the state equations (# fwd) and the adjoint equations (# bwd) are listed in the last row of Table 3.2. The optimization process requires only 39 solves of the linear system in the 10%-noise case and 37 solves in the 15%-noise case, which is a significant reduction on the number of linear solvers as comparison with the results of [58]. In [58], 84 bidomain model runs (with the Beeler–Reuter ionic model [13]) were needed in the 10%-noise case and 62 runs were required in the 15%-noise case. We mention that the comparison is not based on the total execution time, it is rather on the count of direct problem solves, which is independent of the choice of ionic models.

To have a better insight into the efficiency of the optimization method, we plot the

searched value at each optimization iteration (including line search) in Figure 3.5. The conductivity value searched at each iteration is denoted by a (green) box, connected by dashed (red) lines. This figure corresponds to 15% noisy data. The exact value is denoted by a circle. From Figure 3.5 we can see that after about 15 iterations the searched values approach the exact ones.

3.4.2   Three-dimensional tests

We present several test cases to investigate different aspects of our method. In Test 2, 3 and 4 the computational domain was a slab $\Omega = [0,5] \times [0,5] \times [0,0.5] \subseteq \mathbb{R}^3$ with 11516 mesh nodes and the OD scheme was adopted. In each simulation, five stimuli of $I_{\text{si}} = I_{\text{se}} = 10^5$ μA/cm^3 were applied with four at the corners and one at the center of the domain for a duration of 1 ms. With these test cases we want to show (a) the importance of extracellular potential measures in the accuracy of our method; (b) the impact of the regularization parameter α; (c) the sensitivity of the final results to an imperfect knowledge of other parameters of the problem.

Test 5 demonstrates the accuracy of the method on a real geometry with a realistic arrangement of the cardiac fibers. In particular, we discuss the performances of the different approaches, OD with check-pointing and DO. Finally, Test 6 illustrates the result of the method in a case where conductivities are piecewise constant. This may occur in pathological cases, where a scar of the cardiac tissue (for instance after surgery) is present.

As the bidomain solver is much more computational demanding in 3D than in 2D and we want to focus on the specific aspects of the method that are pointed out above, we use the same discretization scheme for the optimization simulation as for generating the measures. However, at each time step, noise was added into the synthetic data uniformly distributed as $U(0, p \max |u|)$, where p is the percentage of noise. The BFGS stopping

Table 3.3: $T = 20$ ms, $\Delta t = 0.1$ ms, $dt_{\text{snap}} = 2$ ms, noise $= 10\%$, # sites $= 1000$, $\boldsymbol{\sigma}_{\text{exact}} = (3.4, 1.2, 0.6, 0.8)$

$\boldsymbol{\sigma}_{\text{initial}}$	(5, 5, 3, 3)			(2, 2, 1, 1)		
measure	u	$u \& u_{\text{e}}$	u_{e}	u	$u \& u_{\text{e}}$	u_{e}
σ_{il}	3.03510	3.36350	3.40531	2.06524	3.36997	3.37996
σ_{el}	1.02949	1.20955	1.20866	1.51519	1.18705	1.21091
σ_{it}	0.32207	0.59114	0.59581	0.45420	0.59954	0.57659
σ_{et}	1.67832	0.80093	0.79820	1.38055	0.82652	0.79027
# fwd | bwd	16 | 12	27 | 16	24 | 19	26 | 15	28 | 17	18 | 12

criterion used was

$$\frac{\|\nabla \mathcal{J}(\boldsymbol{\sigma}^k)\|}{\|\nabla \mathcal{J}(\boldsymbol{\sigma}^0)\|} < 10^{-5} \text{ or } \frac{\|\mathcal{J}^k - \mathcal{J}^{k-1}\|}{\|\mathcal{J}^0\|} < 10^{-5} \text{ or } \frac{\|\boldsymbol{\sigma}^k - \boldsymbol{\sigma}^{k-1}\|}{\|\boldsymbol{\sigma}^{k-1}\|} < 10^{-5}.$$

Test 2: Necessity of extracellular potential measurement. In Test 1 of the previous section, we assumed to have measures of the transmembrane potential only. As a matter of fact, the transmembrane potential data are easier to measure in experiments than the extracellular one. We actually obtained good results in 2D and in the 3D slab as well in the case $\boldsymbol{\sigma}_{\text{exact}} = (2.8, 2.2, 0.26, 1.3)$. Unfortunately, the same circumstance has not been confirmed for other exact values. For instance for reference values $\boldsymbol{\sigma}_{\text{exact}} = (3.4, 1.2, 0.6, 0.8)$, the estimates are significantly less accurate as shown in the second and fifth columns of Table 3.3. In general, extracellular potential data are necessary for reliable estimates. In fact, if we use both measurements from transmembrane and extracellular potentials, or even just the extracellular potential, we find much more accurate results, as reported in Table 3.3.

Test 3: Sensitivity to Tikhonov regularization. We have several choices of the Tikhonov-like regularization term. In this test, we compare four different uses of regularization. Let

$$\mathcal{R}_a = \int_{\Omega} \|\boldsymbol{\sigma} - \hat{\boldsymbol{\sigma}}\|^2 dx, \quad \mathcal{R}_b = \int_{\Omega} (\frac{\sigma_{\text{el}}\sigma_{\text{it}}}{\sigma_{\text{il}}\sigma_{\text{et}}} - \epsilon)^2 dx$$

where $\hat{\boldsymbol{\sigma}}$ is the mean of conductivity values from literatures as used in the two-dimensional test and $\epsilon = 0.24$ is the fairly consistent measurement value of $\frac{\sigma_{\text{el}}\sigma_{\text{it}}}{\sigma_{\text{il}}\sigma_{\text{et}}}$ in the literature,
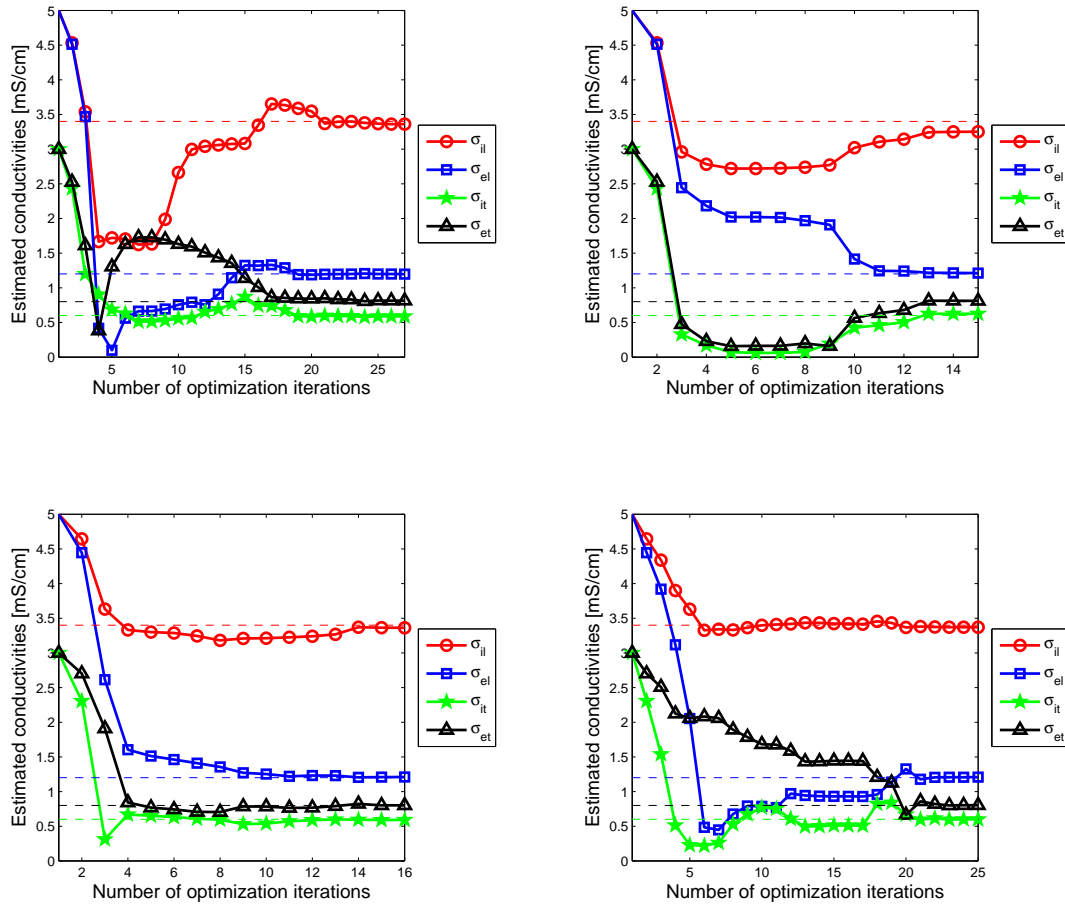
Figure 3.6: Upper left: $\mathcal{M}1$. Upper right: $\mathcal{M}2$. Lower left: $\mathcal{M}3$. Lower right: $\mathcal{M}4$.

which indicates that cardiac tissue has unequal anisotropy ratios. The four ways we use regularization (including the Tikhonov regularization coefficients) are

$$\mathcal{M}1 : \mathcal{R} = 0 \qquad\qquad \mathcal{M}2 : \mathcal{R} = 1/2 \cdot 10^{-4}\mathcal{R}_a$$
$$\mathcal{M}3 : \mathcal{R} = 1/2 \cdot 10^{-3}\mathcal{R}_b \quad \mathcal{M}4 : \mathcal{R} = 1/2 \cdot 10^{-4}\mathcal{R}_a + 1/2 \cdot 10^{-3}\mathcal{R}_b$$

In Figure 3.6 we report the history of estimated $\boldsymbol{\sigma}$ in the optimization iteration process with respect to the number of iterations. In this test, adding regularization terms speeds up the optimization process, as expected. Specifically, the inverse solver with $\mathcal{M}1$ converges in about 20 iterations, while with both $\mathcal{M}2$ and $\mathcal{M}3$ it converges in about 14 steps. The combination of $\mathcal{M}2$ and $\mathcal{M}3$ does not bring any advantage as shown by the
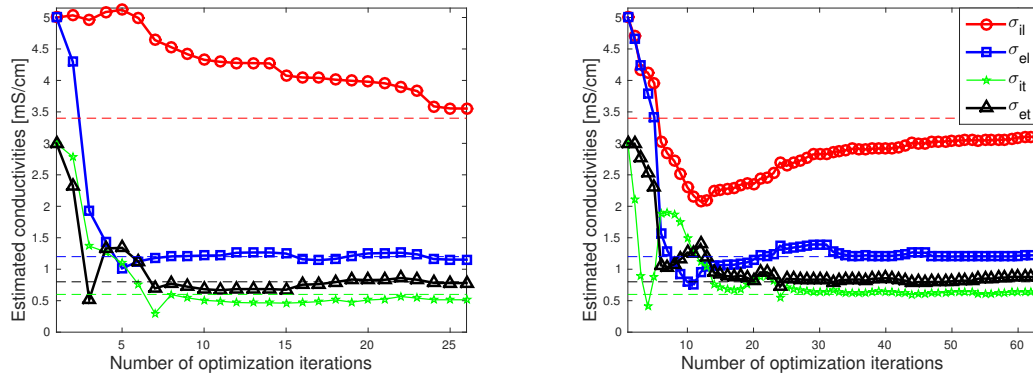
Figure 3.7: In measurement generation the fiber angle is $\theta = -48°$. Inexact fiber directions and ionic model parameters are used in conductivity estimation. Left: fiber angle $\theta = -53°$ and ionic model parameters have 1% noise. Right: fiber angle is spatial dependent with 10% noise and ionic model parameters have 1% noise.

performance of $\mathcal{M}4$. We can also see from the plots that the optimization algorithm is stable even without regularization. This result hints at a broader application of the $\mathcal{M}1$ scheme in consideration of spatial dependent conductivities in pathological tissues (see the example in Test 6), while $\mathcal{M}2$ and $\mathcal{M}3$ are not appropriate because of the uncertainty on $\hat{\boldsymbol{\sigma}}$ in $\mathcal{R}_a$ and ϵ in $\mathcal{R}_b$ when we have more conductivity parameters.

Test 4: Impact of the fiber direction and ionic model parameters. In the clinical application of cardiac potential modeling, not only the cardiac conductivities, but also the cardiac fiber orientation and ionic model parameters vary among patients. The work in this chapter is under the assumption that the ionic model parameters were previously optimized by fitting experimental data using a genetic algorithm [127] or other gradient-based optimization methods like sequential quadratic programming (SQP) [21]. It has been shown that ionic model parameters can be estimated successfully for arbitrary action potential waveforms, and possibly with an error of only 0.03% [127].

Here we focus only on the conductivity parameter estimation and in previous tests the fiber direction and ionic model parameters were the same as those used in measurement data generation. A complete procedure for estimating more patient-dependent parameters, such as fiber angles and conductivities in pathological tissues, is considered as a

continuing work in the future as we discuss in Section 3.5. In this test we check the sensitivity of the conductivity estimation procedure by using inexact fiber direction and ionic model parameters. This test was conducted on the slab as in Test 2 and Test 3. The synthetic measurement data was generated with a constant fiber angle $\theta = -48°$, and 10% noise was then added to the measured potentials. In the simulation for conductivity estimation, we used inexact ionic model parameters: they were changed randomly by at most 1% compared to parameters used in measurement generation. In our first consideration, we used a constant fiber angle $\theta = -53°$ during the inverse solver and the conductivity estimation process is reported in Figure 3.7 (left). In our second consideration, the fiber direction was spatial dependent. The fiber angle at each spatial grid was randomly changed from $-48°$ by at most 10%. Notice that the fiber vector field $(\mathbf{a_l}, \mathbf{a_t}, \mathbf{a_n})$ was not smooth in this case because of the noise, while in the real case the fiber orientation has been known to smoothly rotate between endocardium and epicardium [126]. This may explain the result reported in Figure 3.7 (right). We slightly loose accuracy on the σ_{il} parameter, but the overall result is acceptable, especially in consideration of the good estimation values of σ_{el}, σ_{it}, and σ_{et}.

Test 5: Checkpointing vs Discretize-then-Optimize. In this test, we compare the performance of the checkpointing scheme and the Discretize-then-Optimize scheme. The simulations were performed on a real left ventricular geometry reconstructed from SPECT images. We display some screenshots of the action potential propagation in Figure 3.8. An analytical representation of the fiber orientation was opted for to mimic the main features of the actual cardiac fibers field (shown in Figure 3.9), as originally proposed in [49] eqn. (6.2) for an ellipsoid domain and properly adapted to a real domain retrieved from SPECT images (as already done in [56]). Other computational models of cardiac fibers are also available, such as [11].

We solved the bidomain inverse conductivity problem on a mesh with 22470 degrees of freedom. Δt was chosen as 0.05 ms, and T was 24 ms. We plot the conductivity estimation iterations in Figure 3.10. The execution time using checkpointing (Figure 3.10,
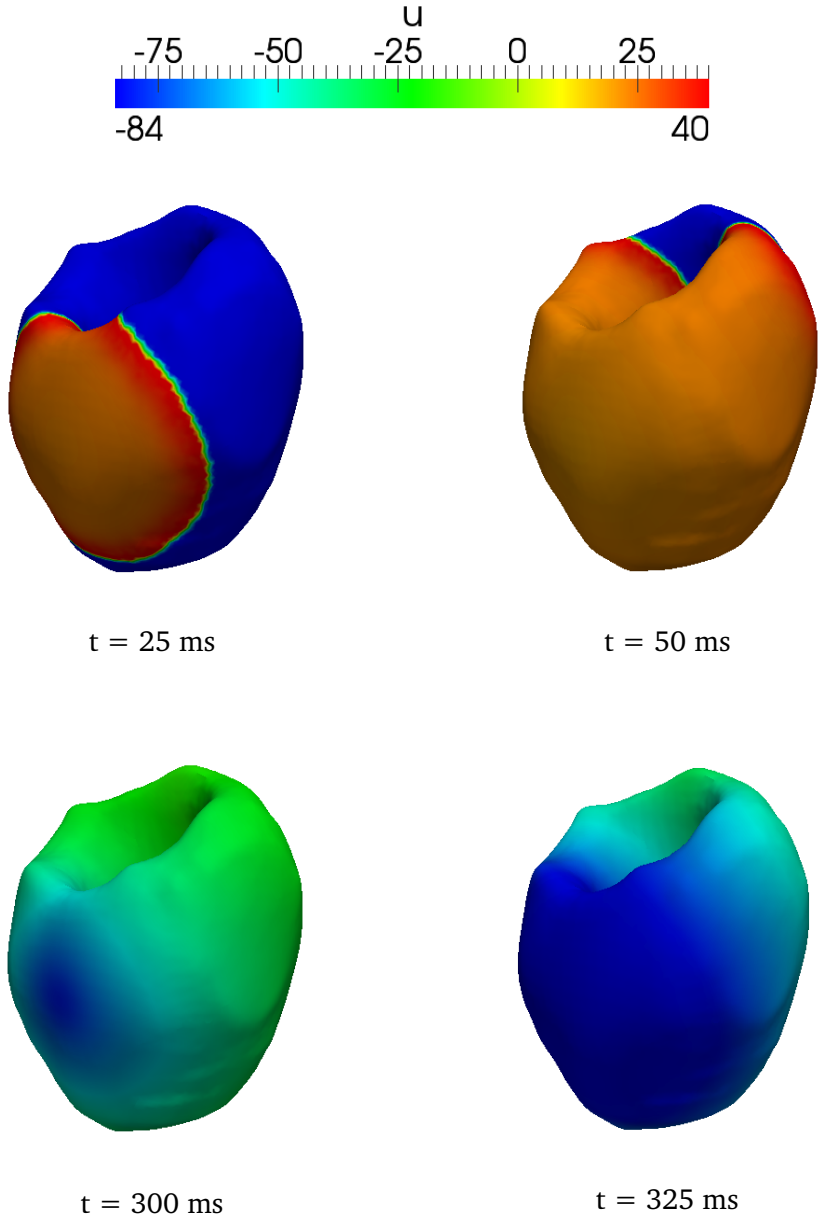
Figure 3.8: Screenshots of the action potential propagation (in mV) at t=25 ms, t=50 ms, t=300 ms, and t=325 ms, computed on a real left ventricular geometry reconstructed from SPECT images.
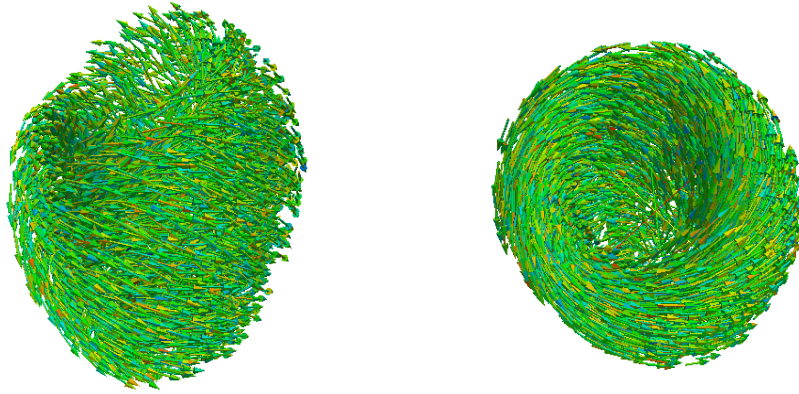
Figure 3.9: Myocardial fiber orientation used in simulation. Left: front view; Right: top view.
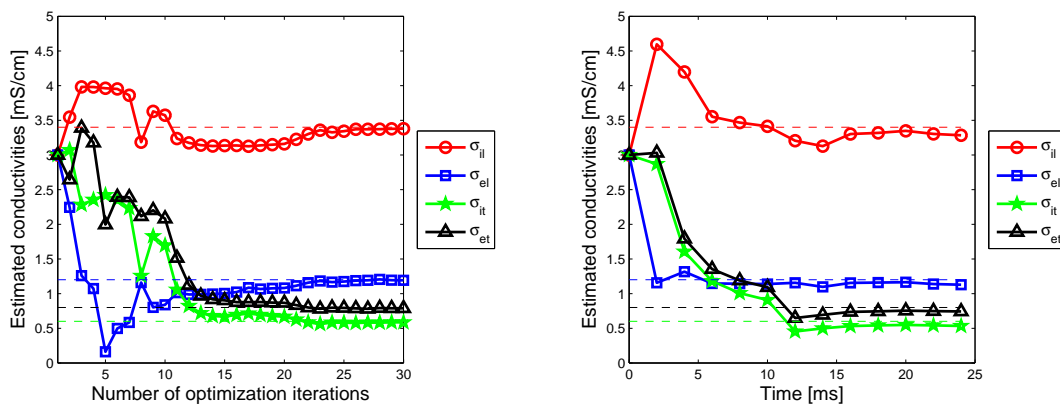
Figure 3.10: Left: Iterations using checkpointing with $dt_{\mathrm{check}} = 1$ ms and $dt_{\mathrm{snap}} = 2$ ms. Right: Iterations by Discretize-then-Optimize with $dt_{\mathrm{opt}} = 2$ ms and $dt_{\mathrm{snap}} = 2$ ms.

Left) is 12.94 h, while the execution time using Discretize-then-Optimize is 5.46 h with $dt_{\mathrm{opt}} = 2$ ms (Figure 3.10, Right). Each simulation was perfomed on four processors with each processor having an Intel(R) Xeon(R) CPU L5420 @ 2.50GHz. Compared with the checkpointing scheme, the Discretize-then-Optimize scheme improves the computation speed by 50% while keeping high accuracy.

Test 6: An example of pathological tissue. In this test, we simply assume that there is a scar inside the cardiac tissue, as shown in Figure 3.11 (left). A scar is included here to
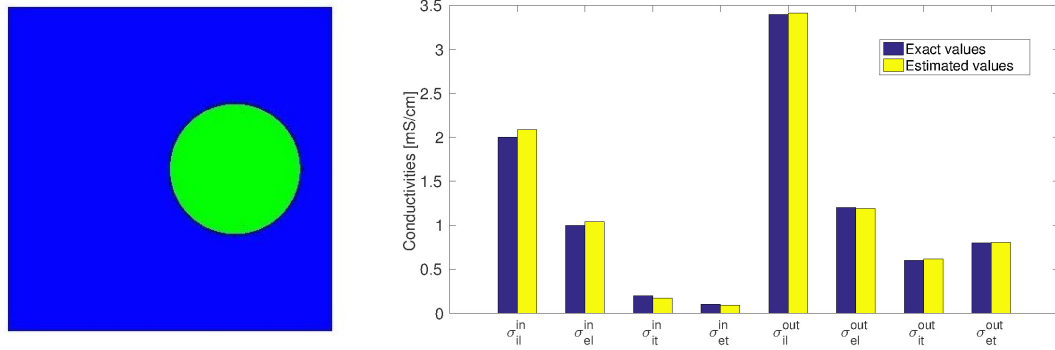
Figure 3.11: Left: A slab tissue with a scar (in green color) inside. Right: Estimated conductivities of the synthetic pathological tissue. The initial guess for estimation is $\boldsymbol{\sigma}_{\mathrm{initial}} = (2, 2, 2, 2, 2, 2, 2, 2)$.

represent a small region with anomalous values of conductivities. The presence of a scar in real patients may trigger pathological patterns in the cardiac potential propagation. The slab tissue in this test had dimension $5 \mathrm{~cm} \times 5 \mathrm{~cm} \times 0.5 \mathrm{~cm}$ and the scar was assumed having radius $1 \mathrm{~cm}$. The conductivity values inside the tissue are different from those outside the tissue. We denote $\boldsymbol{\sigma}_{\mathrm{exact}} = (\sigma_{\mathrm{il}}^{in}, \sigma_{\mathrm{el}}^{in}, \sigma_{\mathrm{it}}^{in}, \sigma_{\mathrm{et}}^{in}, \sigma_{\mathrm{il}}^{out}, \sigma_{\mathrm{el}}^{out}, \sigma_{\mathrm{it}}^{out}, \sigma_{\mathrm{et}}^{out})$, where σ_{*}^{in} (σ_{*}^{out}) are the conductivity values inside (outside) the scar. Synthetic measurements were generated with the conductivity parameters $\boldsymbol{\sigma}_{\mathrm{exact}} = (2, 1, 0.2, 0.1, 3.4, 1.2, 0.6, 0.8)$ and 10% noise was then added. While the number of conductivity parameters are doubled in this circumstance, the optimization procedure still provides highly accurate estimation as illustrated in Figure 3.11 (right). Nevertheless, we stress that the computational costs substantially increase due to the significant growth of number of optimization iterations. The estimation process needs 208 solves of the state system and 100 solves of the adjoint system. This motivates us to further work on a model reduction investigation with the aim of reducing the computational cost, as we will see in Chapter 5.

3.5 Chapter conclusions and developments

The accurate quantification of cardiac conductivities is crucial for extending computational electrocardiology from medical research to clinical practice in a patient-specific

setting. With this motivation, we have investigated a data assimilation approach for providing conductivity estimates from potential measurements. Other approaches are possible, like the one based on Kalman filtering techniques (see e.g. [89]).

We pursue the augmented Lagrangian formulation to compute the gradient of the misfit function needed in the BFGS optimization approach. Technical issues and discretization have been carefully addressed. Some simulations were performed in 2D to compare with results available in the literature. Compared with a least-squares approach [58], the derivative-based optimization method we adopt here is more effective, since we need to solve the adjoint system with a searched set of parameters only once for computing all the Gâteaux derivatives of $\mathcal{J}$. We also presented results in 3D on a slab and on a left ventricular geometry reconstructed from SPECT images using the minimal ionic model as our trade-off between reliability and computational efficiency. The next step of the present work will be to perform validation with *in vitro* experiments.

In future work, we would like to consider more patient-dependent parameters, like the elevation angle and the transverse angle of the fibers, piecewise-constant conductivities, conductivities in different anatomical structures such as the Purkinje fiber and the bundle of His, conductivities in pathological tissues. In general, the more parameters to be estimated, the more optimization iterations are needed and then the slower the personalization procedure.

Since the iterated solution of the bidomain system and its dual in real geometries is fairly demanding [56, 86], it is no surprise that we face formidable computational costs, in particular while estimating the conductivities of pathological tissues when the number of solves of the bidomain system substantially increase, as reported in Test 6 of Section 3.4.2. To handle this issue, we will investigate possible model reduction techniques and then replace the full order model in the optimization process with a low-dimensional model, as done, for instance, in [14] for the estimation of compliance in arteries. This investigation on model reduction is carried out in Chapter 5.

Another important direction we intend to pursue is the rigorous quantification of un-

certainty induced by the presence of noise. In this case, the conductivities estimated will be defined by a probability density function whose moments depend on the noise and the bidomain problem (see e.g. for fluid dynamics [133]).

Chapter 4

Existence analysis for the inverse conductivity problem

In this chapter we prove the existence of a minimizer for the inverse conductivity problem. The proof is largely inspired by Kunisch et al. [93] for the optimization problem concerning pacemaker stimuli.

4.1 Preliminary

Notations. We follow the notations in [93] and denote $V = H^1(\Omega), H = L^2(\Omega), U = V/\mathbb{R}$. The quotient space is used because the solution u_e is determined up to an additive constant. To simplify the notations, we use $L^2(V)$ instead of $L^2(0,T;V)$ (analogous for other function spaces) and $u(t)$ instead of $u(\boldsymbol{x},t)$ (similarly for $u_\mathrm{e}(t)$ and $w(t)$). Here V^* denotes the dual space of V. $\mathcal{D}(0,T)$ is the space of C^∞ functions on $\mathbb{R}$ with compact support in $(0,T)$. The space of all distributions on $\mathcal{D}(0,T)$ is denoted by $\mathcal{D}'(0,T)$. Let us introduce the space $\mathbf{L}^2(\Omega)$ being the space $(L^2(\Omega))^{2d}$, the space $\mathbf{L}^2(\Omega;\mathbb{R}^d)$ being $(L^2(\Omega;\mathbb{R}^d))^{2d}$ and the space $\mathbf{H}^1(\Omega)$ being $(H^1(\Omega))^{2d}$ ($d = 3$ or $d = 2$ for 3D and 2D cases respectively).

We postulate the following assumptions.

1. Ω is a bounded domain in $\mathbb{R}^d$ with Lipschitz boundary $\partial\Omega$.

2. The conductivity tensors $\boldsymbol{\sigma}_{\mathrm{i}}$ and $\boldsymbol{\sigma}_{\mathrm{e}}$ are uniformly elliptic. Namely, there exist constants $m,\ M > 0$ such that

$$\forall \xi \in \mathbb{R}^d,\ m|\xi|^2 \leq \xi^T \boldsymbol{\sigma}_{\mathrm{i,e}}(\boldsymbol{x})\xi \leq M|\xi|^2,\ \text{for all } \boldsymbol{x} \in \Omega. \tag{4.1}$$

3. We assume in particular to work with the Rogers–McCulloch ionic model.

4. I_{si} and I_{se} belong to $L^2(0,T;V^*)$. The initial data u_0 and w_0 belong to $L^2(\Omega)$. We also assume that the stimuli and the initial condition are chosen to ensure that $u_{\mathrm{e}}(0)$ is independent of $\boldsymbol{\sigma}$ (for instance, $u_0 = \text{const.}$ and $I_{\mathrm{si}} - I_{\mathrm{se}} = 0$ a.e.).

Definition 4.1.1 (Weak Solution). $(u, u_{\mathrm{e}}, w) \in (L^2(V) \cap L^4(Q) \cap C(H)) \times L^2(U) \times C(H)$ *is called a weak solution of system (2.15), if* $u(0) = u_0, w(0) = w_0,$ *and* (u, u_{e}, w) *verify in* $\mathcal{D}'(0,T)$:

$$\frac{\partial}{\partial t} \int_\Omega \beta C_{\mathrm{m}} u(t)\varphi + \int_\Omega \boldsymbol{\sigma}_{\mathrm{i}} \nabla(u(t) + u_{\mathrm{e}}(t)) \cdot \nabla\varphi + \int_\Omega \beta I_{\mathrm{ion}}(u(t), w(t))\varphi$$
$$= \int_\Omega I_{\mathrm{si}}(t)\varphi,\ \forall \varphi \in V \tag{4.2}$$

$$\int_\Omega \boldsymbol{\sigma}_{\mathrm{i}} \nabla u(t) \cdot \nabla\phi + \int_\Omega (\boldsymbol{\sigma}_{\mathrm{i}} + \boldsymbol{\sigma}_{\mathrm{e}}) \nabla u_{\mathrm{e}}(t) \cdot \nabla\phi = \int_\Omega (I_{\mathrm{si}}(t) - I_{\mathrm{se}}(t))\phi,\ \forall \phi \in U \tag{4.3}$$

$$\frac{d}{dt} \int_\Omega w(t)\psi + \int_\Omega g(u(t), w(t))\psi = 0,\ \forall \psi \in H \tag{4.4}$$

We recall some results of the literature relevant to our analysis.

Theorem 4.1.2 ([19] thm. 30, [75] thm. 2.8). *Under the assumptions (i)-(iv) above, the bidomain system (2.15) has a unique weak solution* (u, u_{e}, w).

Lemma 4.1.3 (*A priori* estimate, [93] lem. 3.5). *Under the same assumptions (i)-(iv) of*

the previous Theorem, there exist positive constants $\tilde{C}$ and $\tilde{c}$, such that

$$|u|_{C(H)} + |u|_{L^2(V)} + |u|_{L^4(Q)} + |\partial_t u|_{L^{4/3}(V^*)} + |u_{\mathrm{e}}|_{L^2(U)} + |w|_{C(H)} + |\partial_t w|_{L^2(H)}$$

$$\leq \tilde{C}(|u_0| + |u_{\mathrm{e},0}| + \tilde{c}|\Omega| + |I_{\mathrm{si}}|_{L^2(V^*)} + |I_{\mathrm{si}} - I_{\mathrm{se}}|_{L^2(U^*)}) \tag{4.5}$$

where $\tilde{c}$ depends on the ionic model, $\tilde{C}$ depends on the constants m and M in (4.1) and the ionic model, but $\tilde{C}$ is independent of (u_0, w_0), $(I_{\mathrm{si}}, I_{\mathrm{se}})$ and $\boldsymbol{\sigma}_{\mathrm{i,e}}$.

4.2 The existence proof

Theorem 4.2.1 (Existence of minimizer). *Under the previous assumptions, for the regularization parameter $\alpha \geq 0$, there exists at least one minimizer for the bidomain inverse conductivity problem.*

Proof. Since $\mathcal{J}$ is bounded from below, $\inf_{\boldsymbol{\sigma} \in \mathcal{C}_{\mathrm{ad}}} \mathcal{J}(\boldsymbol{\sigma}) \in \mathbb{R}$ and there exists a minimizing sequence $\boldsymbol{\sigma}^{(k)} \in \mathcal{C}_{\mathrm{ad}}$ such that

$$\lim_{k \to \infty} \mathcal{J}(\boldsymbol{\sigma}^{(k)}) = \inf_{\boldsymbol{\sigma} \in \mathcal{C}_{\mathrm{ad}}} \mathcal{J}(\boldsymbol{\sigma}).$$

Since the terms $\{\boldsymbol{\sigma}^{(k)}\}$ are bounded in $\mathbf{L}^\infty(\Omega)$, it follows from the sequential Banach–Alaoglu theorem that there exists a subsequence of $\boldsymbol{\sigma}^{(k)}$, which we denote by the same symbol, such that

$$\boldsymbol{\sigma}^{(k)} \to \boldsymbol{\sigma}^* \quad \text{weakly-}* \text{ in } \mathbf{L}^\infty(\Omega). \tag{4.6}$$

We claim that $\boldsymbol{\sigma}^* \in \mathcal{C}_{\mathrm{ad}}$. Indeed, if for example $\Gamma = \{\boldsymbol{x} : \sigma_{\mathrm{il}}^*(x) > M\}$ has positive measure, then $\int_\Omega (\sigma_{\mathrm{il}}^*(\boldsymbol{x}) - \sigma_{\mathrm{il}}^{(k)})\chi_\Gamma d\boldsymbol{x} \geq \int_\Gamma (\sigma_{\mathrm{il}}^*(\boldsymbol{x}) - M)d\boldsymbol{x} > 0$, which leads to a contradiction, since, for $k \to \infty$, the left hand side should be zero. The case for the other entries of the conductivity tensors and the lower bound m is the same.

Let $(u^{(k)}, u_{\mathrm{e}}^{(k)}, w^{(k)})$ be the associated solution of the bidomain model with $\boldsymbol{\sigma}^{(k)}$, by the *a priori* estimate and the weak compactness property, there exists a subsequence of $(u^{(k)}, u_{\mathrm{e}}^{(k)}, w^{(k)}, \boldsymbol{\sigma}^{(k)}) \in (L^2(V) \cap L^4(Q)) \times L^2(U) \times C(H) \times \mathbf{L}^\infty(\Omega)$, denoted by the same

sequence, such that

$$u^{(k)} \rightharpoonup u \text{ in } L^2(V) \cap L^4(Q), \quad u_e^{(k)} \rightharpoonup u_e \text{ in } L^2(U), \quad w^{(k)} \rightharpoonup w \text{ in } L^2(H) \tag{4.7}$$

$$\frac{\partial}{\partial t} u^{(k)} \rightharpoonup \frac{\partial}{\partial t} u \text{ in } L^{4/3}(V^*), \quad \frac{d}{dt} w^{(k)} \rightharpoonup \frac{d}{dt} w \text{ in } L^2(H) \tag{4.8}$$

Let the corresponding bilinear forms associated with $\{\boldsymbol{\sigma}^{(k)}, \boldsymbol{\sigma}^*\}$ be $\{a_{i,e}^k, a_{i,e}^*\}$:

$$a_{i,e}^k(u, v) = \int_\Omega \boldsymbol{\sigma}_{i,e}^{(k)} \nabla u \cdot \nabla v, \quad a_{i,e}^*(u, v) = \int_\Omega \boldsymbol{\sigma}_{i,e}^* \nabla u \cdot \nabla v.$$

Since the conductivity tensors are uniformly elliptic, $|a_i^*(u, v)| \leq M\|u\|_V \|v\|_V$. This means for fixed $v \in V$, we have $a_i^* \in V^*$. Since $u^{(k)}$ is weakly convergent and $\phi v \in L^4(Q) \cap L^2(V)$ for any $\phi \in \mathcal{D}(0, T)$, we have

$$\int_0^T a_i^*(u^{(k)}, \phi v) dt \to \int_0^T a_i^*(u, \phi v) dt, \quad \forall \phi \in \mathcal{D}(0, T), \ v \in V. \tag{4.9}$$

For any fixed $\phi \in \mathcal{D}(0, T)$ and $\psi \in \mathcal{C}_0^\infty(\mathbb{R}^d)$, we have

$$\int_0^T a_i^k(u^{(k)}, \phi\psi) dt - \int_0^T a_i^*(u^{(k)}, \phi\psi) dt$$

$$= \int_0^T \int_\Omega (\sigma_{il}^{(k)} - \sigma_{il}^*) \mathbf{a_l a_l}^T \nabla u^{(k)} \cdot \nabla(\phi\psi) + \int_0^T \int_\Omega (\sigma_{it}^{(k)} - \sigma_{it}^*) \mathbf{a_t a_t}^T \nabla u^{(k)} \cdot \nabla(\phi\psi)$$

$$+ \int_0^T \int_\Omega (\sigma_{in}^{(k)} - \sigma_{in}^*) \mathbf{a_n a_n}^T \nabla u^{(k)} \cdot \nabla(\phi\psi)$$

$$= \int_0^T \int_\Omega (\sigma_{il}^{(k)} - \sigma_{il}^*) \mathbf{a_l}^T \nabla(\phi\psi) \mathbf{a_l}^T \nabla u^{(k)} + \int_0^T \int_\Omega (\sigma_{it}^{(k)} - \sigma_{it}^*) \mathbf{a_t}^T \nabla(\phi\psi) \mathbf{a_t}^T \nabla u^{(k)}$$

$$+ \int_0^T \int_\Omega (\sigma_{in}^{(k)} - \sigma_{in}^*) \mathbf{a_n}^T \nabla(\phi\psi) \mathbf{a_n}^T \nabla u^{(k)}$$

Notice that $\mathbf{a_l}$ has unit length and $\nabla(\phi\psi)$ is in $L^\infty(Q; \mathbb{R}^d)$. While $\{\boldsymbol{\sigma}^{(k)}\}$ can be treated as weakly-$*$ convergent to $\boldsymbol{\sigma}^*$ in $\mathbf{L}^\infty(Q)$, we have $\{\boldsymbol{\sigma}^{(k)} \mathbf{a_l}^T \nabla(\phi\psi)\}$ weakly-$*$ convergent to

$\sigma^* \mathbf{a_l}^T \nabla(\phi\psi)$ in $\mathbf{L}^\infty(Q)$. From

$$||\nabla u^{(k)}||_{L^1(Q;\mathbb{R}^d)} \leq (|\Omega|T)^{1/2}||\nabla u^{(k)}||_{L^2(Q;\mathbb{R}^d)}$$

and the *a priori* estimate of Lemma 3.3, we conclude that $\{\nabla u^{(k)}\}$ is bounded in $L^1(Q;\mathbb{R}^d)$. Therefore, by passing to a subsequence, we can require $\nabla u^k \rightharpoonup \nabla u$ in $L^1(Q;\mathbb{R}^d)$. The Dunford–Pettis property of $L^1(Q)$ (see [78], sec. 1.6) thus leads to the following convergence

$$\int_0^T \int_\Omega (\sigma_{il}^{(k)} - \sigma_{il}^*)\mathbf{a_l}^T \nabla(\phi\psi)\mathbf{a_l}^T \nabla u^{(k)} \to 0, \text{ as } k \to \infty. \tag{4.10}$$

The convergence follows also for the other two terms in the same way, we then have

$$\int_0^T a_i^k(u^{(k)}, \phi\psi)dt - \int_0^T a_i^*(u^{(k)}, \phi\psi)dt \to 0, \text{ as } k \to \infty \quad \forall \phi \in \mathcal{D}(0,T), \ \psi \in \mathcal{C}_0^\infty(\mathbb{R}^d).$$

Since Ω has Lipschitz boundary, it then satisfies the segment condition (see [2], def. 3.21). We say $\mathcal{C}_0^\infty(\mathbb{R}^d)$ is dense in V (see [2], thm. 3.22). Therefore we have

$$\int_0^T a_i^k(u^{(k)}, \phi v)dt - \int_0^T a_i^*(u^{(k)}, \phi v)dt \to 0, \text{ as } k \to \infty, \quad \forall \phi \in \mathcal{D}(0,T), \ v \in V.$$

Combined with limit (4.9) this convergence implies

$$\int_0^T a_i^k(u^{(k)}, \phi v)dt - \int_0^T a_i^*(u, \phi v)dt \to 0, \text{ as } k \to \infty, \quad \forall \phi \in \mathcal{D}(0,T), \ v \in V. \tag{4.11}$$

Similarly, we can show

$$\int_0^T a_i^k(u_e^{(k)}, \phi v)dt - \int_0^T a_i^*(u_e, \phi v)dt \to 0, \text{ as } k \to \infty, \quad \forall \phi \in \mathcal{D}(0,T), \ v \in V \tag{4.12}$$

$$\int_0^T a_e^k(u_e^{(k)}, \phi v)dt - \int_0^T a_e^*(u_e, \phi v)dt \to 0, \text{ as } k \to \infty, \quad \forall \phi \in \mathcal{D}(0,T), \ v \in V. \tag{4.13}$$

The proof for the convergence of the other terms in equations (4.2)–(4.4) is standard, and we refer to [19] p.477. By passing to the limit in the equations satisfied by $(u^{(k)}, u_e^{(k)}, w^{(k)},$

$\boldsymbol{\sigma}^{(k)}$), we argue that $(u, u_e, w, \boldsymbol{\sigma}^*)$ is a solution to the bidomain equations.

We then conclude that $\boldsymbol{\sigma}^*$ realizes the minimum of $\mathcal{J}$. Since $u^{(k)}$ are bounded in $L^2(V)$ and $u_e^{(k)}$ are bounded in $L^2(U)$, by the Rellich–Kondrachov selection theorem, we can assume that $u^{(k)}$ converges strongly to u in $L^2(Q)$ and $u_e^{(k)}$ converge strongly to u_e in $L^2(Q)$. In fact, from convergence (4.6) it follows that $\{\boldsymbol{\sigma}^{(k)}\}$ is also weakly convergent in $\mathbf{L}^2(\Omega)$. The weak lower semicontinuity of $\int_\Omega ||\boldsymbol{\sigma}^{(k)} - \hat{\boldsymbol{\sigma}}||^2 d\boldsymbol{x}$ in $\mathbf{L}^2(\Omega)$ then implies that

$$
\begin{aligned}
\mathcal{J}(\boldsymbol{\sigma}^*) &= \frac{1}{2} \int_0^T \int_\Omega (u - u_{\text{meas}})^2 + (u_e - u_{e,\text{meas}})^2 d\boldsymbol{x} dt + \frac{\alpha}{2} \int_\Omega ||\boldsymbol{\sigma}^* - \hat{\boldsymbol{\sigma}}||^2 d\boldsymbol{x} \\
&\leq \frac{1}{2} \lim_{k \to \infty} \int_0^T \int_\Omega (u^{(k)} - u_{\text{meas}})^2 + (u_e^{(k)} - u_{e,\text{meas}})^2 d\boldsymbol{x} dt + \frac{\alpha}{2} \liminf_{k \to \infty} \int_\Omega ||\boldsymbol{\sigma}^{(k)} - \hat{\boldsymbol{\sigma}}||^2 d\boldsymbol{x} \\
&\leq \liminf_{k \to \infty} \left(\frac{1}{2} \int_0^T \int_\Omega (u^{(k)} - u_{\text{meas}})^2 + (u_e^{(k)} - u_{e,\text{meas}})^2 d\boldsymbol{x} dt + \frac{\alpha}{2} \int_\Omega ||\boldsymbol{\sigma}^{(k)} - \hat{\boldsymbol{\sigma}}||^2 d\boldsymbol{x} \right) \\
&= \lim_{k \to \infty} \mathcal{J}(\boldsymbol{\sigma}^{(k)}) = \inf_{\boldsymbol{\sigma} \in \mathcal{C}_{\text{ad}}} \mathcal{J}(\boldsymbol{\sigma}),
\end{aligned}
$$

and the existence of a minimizer is proved.   □

Remark 1. When $\mathcal{J}$ has a minimum at $\boldsymbol{\sigma}^*$ belonging to the interior of $\mathcal{C}_{\text{ad}}$, the derivatives of J in any direction are zero, which leads to the KKT system [59]. However, $\boldsymbol{\sigma}^*$ could be on the boundary $\partial \mathcal{C}_{\text{ad}}$. In this case, the solution is not a stationary point of the mismatch functional. Nevertheless, there are some special choices of the regularization term to make sure $\boldsymbol{\sigma}^*$ belongs to the interior of $\mathcal{C}_{\text{ad}}$. For example, we can choose $\mathcal{R} = \int_\Omega ||\log \boldsymbol{\sigma} - \log \hat{\boldsymbol{\sigma}}||^2 d\boldsymbol{x}$ as the regularization term, since the conductivity parameters are strictly positive. In this case,

$$
\mathcal{R} = \int_\Omega ||\log \boldsymbol{\sigma} - \log \hat{\boldsymbol{\sigma}}||^2 d\boldsymbol{x} \to \infty, \text{ as } \boldsymbol{\sigma} \to 0 \text{ or } \boldsymbol{\sigma} \to \infty.
$$

Notice that the first term in $\mathcal{J}$ is non-negative, so for proper values of m and M guarantees that the minimum of $\mathcal{J}$ will not be on the boundary $\partial \mathcal{C}_{\text{ad}}$ (see also [104]).

Remark 2. If we can refer to the more restrictive admissible domain for control variables

$\mathcal{C}_{\mathrm{ad}}^* = \{\boldsymbol{\sigma} = (\sigma_{\mathrm{il}}, \sigma_{\mathrm{el}}, \sigma_{\mathrm{it}}, \sigma_{\mathrm{et}}, \sigma_{\mathrm{in}}, \sigma_{en}) \in \mathbf{H}^1(\Omega) : \boldsymbol{\sigma}(\boldsymbol{x}) \in [m, M]^{2d}, \forall \boldsymbol{x} \in \Omega\}$, we can actually prove the existence without using the Dunford–Pettis property. For the minimizing sequence $\boldsymbol{\sigma}^{(k)} \rightharpoonup \boldsymbol{\sigma}^*$ in $\mathbf{L}^2(\Omega)$, we also have $\nabla\boldsymbol{\sigma}^{(k)} \rightharpoonup \nabla\boldsymbol{\sigma}^*$ in $\mathbf{L}^2(\Omega; \mathbb{R}^d)$ by the uniform boundedness principle. Therefore $\{\boldsymbol{\sigma}^{(k)}\}$ is bounded in $\mathbf{H}^1(\Omega)$, which then implies a subsequence strongly convergent in $\mathbf{L}^2(\Omega)$. So with the admissible domain $\mathcal{C}_{\mathrm{ad}}^*$ we may assume $\boldsymbol{\sigma}^{(k)} \to \boldsymbol{\sigma}^*$ pointwise a.e.

In the course of proving convergence (4.10), we obtain

$$\int_0^T \int_\Omega (\sigma_{\mathrm{il}}^{(k)} - \sigma_{\mathrm{il}}^*)\mathbf{a_l}^T \nabla(\phi\psi)\mathbf{a_l}^T \nabla u^{(k)} \leq ||(\sigma_{\mathrm{il}}^{(k)} - \sigma_{\mathrm{il}}^*)\mathbf{a_l}^T \nabla(\phi\psi)||_{L^2(Q)} \cdot ||\mathbf{a_l}^T \nabla u^{(k)}||_{L^2(Q)}.$$

Notice that $\{||\mathbf{a_l}^T \nabla u^{(k)}||_{L^2(Q)}\}$ is uniformly bounded since $|\mathbf{a_l}| = 1$ and $\{\nabla u^{(k)}\}$ are bounded in $L^2(Q; \mathbb{R}^d)$. By the Dominated Convergence theorem,

$$||(\sigma_{\mathrm{il}}^{(k)} - \sigma_{\mathrm{il}}^*)\mathbf{a_l}^T \nabla(\phi\psi)||_{L^2(Q)} \to 0 \text{ as } k \to \infty.$$

Remark 3. Finally, from the theoretical point of view, uniqueness analysis of the solution to the BICP remains an open problem.

Chapter 5

Reduced-order modeling for cardiac conductivity estimation

5.1 Introduction

Solution of a large scale inverse problem, such as the inverse conductivity problem, is usually computationally demanding. High computational cost arises in many "queries" of forward simulations with different model parameters. The computation is particularly intensive in biomedical simulations, when the mesh and time constraints are expected to be significant in clinical applications. In this chapter, we apply model reduction techniques that are expected to dramatically decrease the computational cost of solving the inverse conductivity problem.

Several strategies are available to cope with the challenge of reducing computational costs (see e.g. [15]). One of these is the *physical model reduction*. Basically, this consists of an educated downscaling of the forward problem into simpler system under a physical assumption, yet hopefully retaining the main features of the forward problem. In view of this, in this chapter we use the monodomain model as a surrogate of the bidomain model, following the *potential oriented line*. Specifically, we evaluate the reliability of the monodomain model when reproducing the potential propagation with the estimated

tensor $\boldsymbol{\sigma}_{\mathrm{m}}$. Assumptions of the monodomain model are not necessarily realistic, never-theless, we speculate that an appropriate estimate of the conductivity tensor $\boldsymbol{\sigma}_{\mathrm{m}}$ based on our variational procedure can still lead to an accurate reconstruction of the potential. This potentially has a great impact on reducing the computational cost for practical applications (e.g. pace-maker leads placement optimization).

Another widely used approach in reduced order modeling is the *mathematical model reduction* based on the definition of a "surrogate" solution for the forward problem. A numerical solution to the forward problem by Galerkin projection can be represented, in general terms, as an expansion

$$u_h(\boldsymbol{x}, t) = \sum_{j=1}^{n} u_j(t)\phi_j(\boldsymbol{x}, t).$$

In finite elements, the basis function set $\{\phi_j(\boldsymbol{x}, t)\}$ is given for instance by piecewise polynomial functions. They are generally time-independent (apart from moving-domain problems) and do not rely upon the specific problem. This guarantees versatility to the method such that it can be applied to a vast class of differential problems. However, versatility means that the basis is of general purpose, it does not contain any information on the problem at hand and this generally leads to a large number of degrees of free-dom n to get an accurate solution. Mathematical model reduction aims at cheaply solve the forward equations in a low-dimensional space still by a Galerkin projection process. We construct a different set of basis functions (known as *reduced basis*), that we define "educated", since it include features of the solutions to the forward problem considered. This allows to represent a solution with a low number of degrees of freedom n. However, the computation of an appropriate educated basis may be computationally expensive. An *offline-online decomposition* is often adopted by model reduction techniques accordingly, which includes an offline process for reduced basis construction and an online process to solve the degrees of freedom u_j cheaply, thanks to the small size n.

Among various techniques for the reduced basis construction, typical ones are the *Proper Orthogonal Decomposition* (POD) approach [17, 48, 73, 136], the *Greedy Reduced*

Basis (GRB) approach [22, 46, 110], and their combination [68, 96]. In these approaches, the reduced basis is constructed from a set of parameter-induced solutions of the original full-order model. The POD approach, which is also named as the *Karhunen–Loéve transform* (KLT) in signal processing and the *Principal Component Analysis* (PCA) in statistics, has drawn widespread attention for its optimal ability to approximate the snapshots with minimized error by the selection of the most energetic modes. We therefore employ the POD approach in this chapter as a starting point. The GRB approach selects the snapshots carefully with a greedy selection process according to a rule controlled by a sharp and effective *a posteriori* error estimator. Although decent in the small number of snapshot computations, the requirement of a rigorous error estimator makes it applicable only to a limited class of problems where an error estimator is achievable.

In the particular circumstance of having a nonlinear forward model, as the models in electrocardiology considered in this thesis, the reduced-order model obtained by Galerkin projection has a computational complexity still depending on the order of the full system. Therefore, the dimension of the full-order model is not thoroughly reduced. Several techniques have been proposed in the literature to reduce the computational cost of evaluating the nonlinear terms. One is to take schemes used in general function approximation, such as the multi-linear forms of polynomial nonlinearities [8, 26, 41, 113]. A typical example is the *trajectory piecewise-linear* (TPWL) approach developed by Rewienski and White [113]. Although it was successfully applied to some practical problems [12, 112], this approach may not be effective or efficient for systems with high order of nonlinearity. Other techniques for nonlinear model reduction include the *Best Point Interpolation Method* (BPIM) introduced by Nguyen et al. [95], the *Missing Point Estimation* (MPE) proposed by Astrid [6], the *Empirical Interpolation Method* (EIM) developed by Barrault et al. [9] and its discrete variant *Discrete Empirical Interpolation Method* (DEIM) proposed by Chaturantabut and Sorensen [30]. These approaches are similar in the sense that they select a small set of spatial points to avoid the expensive calculation of inner products required in nonlinear evaluation. However, they differ in the fundamental procedures for

obtaining the reduced system and for selecting the spatial points. MPE extracts certain equations of the full system before the POD projection corresponding to a specially chosen spatial points, whereas BPIM and EIM use the selected spatial interpolation points for approximating the nonlinear terms. The BPIM and EIM approaches are similar [54] in approximating the nonlinear term as a linear combination of spatial dependent basis functions with time (or parameter) dependent coefficients. BPIM is optimal in the point selection and gains a little improvement on accuracy as compared to EIM, but it is far more computational expensive. As a result, we resort to EIM and use its discrete variant DEIM in this chapter.

Besides physical and mathematical model reduction techniques, *statistical model reduction* techniques relying on machine learning (often referred to as *meta-modeling*) have been investigated in particular in the chemometrics community. The idea is to fit a statistical model that is able to predict the output of a nonlinear computational model which has complex dynamics, while being expressed with fewer parameters and being extremely computationally efficient [128]. This statistical approach has been employed in [138] for atria electrophysiology modeling and the work is presented in Chapter 6.

In this chapter, we apply the POD-DEIM model reduction approach for the inverse problem of cardiac conductivity estimation. The POD approach has been used in numerous fields of science and engineering such as fluid-structure interaction [14] and aerodynamics [23], but its practical application in electrocardiology only starts from [17] in 2011 and [18] in 2012. Although it allows reasonable estimation of ionic model parameters in [17] and [18], a proper technique for nonlinear approximation was not carried out and no study on the improvement of efficiency was reported. The POD-DEIM approach for the effective solution of the FitzHugh–Nagumo system arising in neuron modeling—which is equivalent to the monodomain equation in 1D coupled with the FitzHugh–Nagumo ionic model—has been investigated by Chaturantabut [29]. In that paper it is shown that the POD-DEIM approach with both the POD and DEIM dimensions being 30 gives good approximation to the original full-order finite difference system (in

1D). The model parameters were fixed in that study. The present work in this Chapter is an application of the POD-DEIM method on the parameterized monodomain model in 3D for conductivity estimation.

After a brief statement of the full-order *monodomain inverse conductivity problem* (MICP) in a discrete form (Sec. 5.2), the POD-DEIM is introduced (Sec. 5.3) and applied to solve a reduced MICP (Sec. 5.4). The reduced-order model is tested in Sec. 5.5: we investigate both the efficiency and accuracy of the POD-DEIM approach in conductivity estimation. A failure-and-success attribute specially for the system in electrocardiology is reported. We obtain a rather small set of samples by sampling the parameter space based on polar coordinates and densifying the "boundary layer" of the sample space utilizing Gauss–Lobatto nodes. In usage of the POD-DEIM reduced order model, the computational effort can be reduced by at least 90% in conductivity estimation.

5.2   The full-order monodomain inverse conductivity problem

The bidomain model—popular for its physiological foundation—is widely used to simulate action potential spreading in the myocardium, as has been used in Chapter 3. However, simulations of the cardiac electrical activity with the bidomain model require high computational cost, since the model takes the form of a degenerate system of PDEs and the mesh and time constraints are significant in order to simulate fast potential variation. As introduced in Sec. 2.3, the monodomain model as a heuristic approximation of the bidomain model has been proposed to provide computational improvements.

Although the assumption on its derivation lacks physiological foundation, the monodomain model has been drastically used in clinic-oriented simulations [10, 67, 135]. One reason is that it requires significantly less computational efforts than the bidomain model. Another motivation to the interest in the monodomain model is that, as an approximation of the bidomain model, it may serve as a powerful auxiliary tool to efficiently solve the bidomain model [56,57,86]. Most importantly, a comparison between the bidomain and monodomain models in [50] showed a strong qualitative agreement between
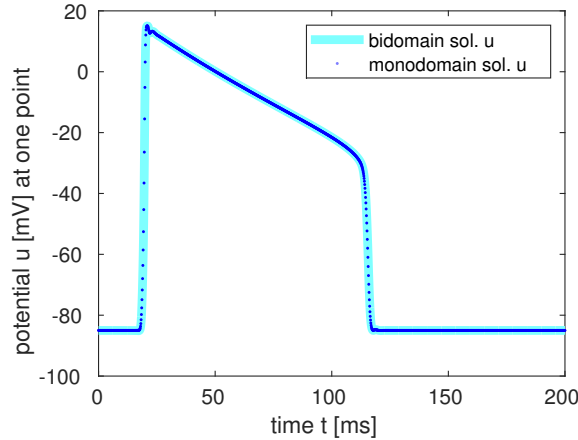
Figure 5.1: The reconstruction of potential by the monodomain solver, computed with the estimated conductivity $\sigma_m = [1.704, 0.3551]$, gives an excellent matching with the bidomain solution, which is computed with $[\sigma_{il}, \sigma_{el}, \sigma_{it}, \sigma_{et}] = [3.5, 3, 0.3, 1.8]$.

the two models and reported a quantitative difference with 5 to 10 % relative error on the activation time. It is further concluded in [20] that the discrepancy between the models at the continuous level is quite small: of order 1% or even below in terms of activation time relative error. The work in [20] also allows to estimate the discretization error so providing necessary grid resolution in order to run accurate enough simulation.

We resort to the monodomain model in this chapter for the cardiac conductivity estimation, following the potential oriented line. Namely, we speculate that an appropriate estimate of the conductivity tensor σ_m based on our variational procedure can still lead to an accurate reconstruction of the potential propagation. This is demonstrated by the numerical result shown in Fig. 5.1, where the bidomain solution u was computed on a slab mesh with $[\sigma_{il}, \sigma_{el}, \sigma_{it}, \sigma_{et}] = [3.5, 3, 0.3, 1.8]$ and was used as synthetic measure to estimate the conductivity σ_m in the monodomain solver. The reconstruction of potential by the monodomain solver with the estimated conductivity $\sigma_m = [1.704, 0.3551]$ gives an excellent matching with the bidomain solution.

In the following, we describe the time and space discretization schemes for the monodomain model, and state the monodomain inverse conductivity problem in a discrete version. As a starting point of thorough studies on reduced order modeling for conduc-

tivity estimation, here we simply use the Rogers–McCulloch ionic model.

Time and space discretization

Let us recall the monodomain equation coupled with the Rogers–McCulloch ionic model

$$
\begin{cases}
\beta C_{\mathrm{m}} \dfrac{\partial u}{\partial t} - \nabla \cdot (\boldsymbol{\sigma}_{\mathrm{m}} \nabla u) + \beta I_{\mathrm{ion}}(u, w) = I_{\mathrm{app}} & \text{in } Q \\[2ex]
\dfrac{\partial w}{\partial t} + g(u, w) = 0 & \text{in } Q \\[2ex]
\boldsymbol{\sigma}_{\mathrm{m}} \nabla u \cdot \mathbf{n} = 0 & \text{on } \partial Q \\[2ex]
u(\boldsymbol{x}, 0) = u_0(\boldsymbol{x}) \quad w(\boldsymbol{x}, 0) = w_0(\boldsymbol{x}) & \text{in } \Omega.
\end{cases}
\tag{5.1}
$$

We apply the same discretization techniques as in Sec. 3.3.1 to the monodomain system, and in particular a second-order time extrapolation is employed in nonlinearity. The notations here are similar as before so we will not redefine them. Specially, bold symbols will denote the spacial variables in discrete form. The gating variable $\mathbf{w}^{l+1}$ in the ionic model at time $t = t^{l+1}$ is updated by

$$
\frac{\mathbf{w}^{l+1} - \mathbf{w}^l}{\Delta t} = -g(\tilde{\mathbf{u}}^{l+1}, \mathbf{w}^{l+1})
\tag{5.2}
$$

where $\tilde{\mathbf{u}}^{l+1} = 2\mathbf{u}^l - \mathbf{u}^{l-1}$ is the second-order time extrapolation of $\mathbf{u}^{l+1}$, $g(\cdot)$ is evaluated point-wise. The algebraic monodomain system reads

$$
\mathbf{A}_{\mathrm{m}} \mathbf{u}^{l+1} = \mathbf{b}^{l+1}
\tag{5.3}
$$

where $\mathbf{A}_{\mathrm{m}} = \beta C_{\mathrm{m}} \frac{\alpha_0}{\Delta t} \mathbf{M} + \mathbf{S_m}$, and the right-hand side is evaluated as

$$
\mathbf{b}^{l+1} = \left[\langle I_{\mathrm{app}}^{l+1} - \beta I_{\mathrm{ion}}(\tilde{u}^{l+1}, w^{l+1}), \phi_j \rangle_{L^2} \right] + \beta C_{\mathrm{m}} \mathbf{M} \sum_{i=1}^{2} \frac{\alpha_i}{\Delta t} \mathbf{u}^{l+1-i}.
\tag{5.4}
$$

For computational efficiency and for the convenience to apply model reduction which we will see in Sec. 5.4, we approximate the nonlinear function I_{ion} and the stimulus I_{app}

piecewise linearly. Under this assumption, the right hand side is evaluated as

$$\mathbf{b}^{l+1} = \mathbf{M}\mathbf{I}_{\mathrm{app}}^{l+1} - \beta\mathbf{M}I_{\mathrm{ion}}(\tilde{\mathbf{u}}^{l+1}, \mathbf{w}^{l+1}) + \beta C_{\mathrm{m}}\mathbf{M}\sum_{i=1}^{2}\frac{\alpha_i}{\Delta t}\mathbf{u}^{l+1-i}. \tag{5.5}$$

In this computation, $I_{\mathrm{ion}}(\tilde{\mathbf{u}}^{l+1}, \mathbf{w}^{l+1})$ is a point-wise evaluation. We state that this point-wise assumption would highly improve computational efficiency without much lose of accuracy as compared with the exact finite element approximation in (5.4). This will be confirmed in Sec. 5.5.3.

The inverse problem

As we start, we assume that the conductivities σ_{ml} and σ_{mt} are constant. A further study will be carried out in the future assuming the conductivities are piece-wise constant. The *monodomain inverse conductivity problem* (MICP) is formulated as: find $\boldsymbol{\sigma} = [\sigma_{\mathrm{ml}}, \sigma_{\mathrm{mt}}] \in [m_b, M_b]^2$ that minimizes the functional

$$\mathcal{J}_{\mathrm{m}}(\boldsymbol{\sigma}) = \frac{1}{2}\sum_{l=1}^{L}(\mathbf{u}^l - \mathbf{u}_{\mathrm{meas}}^l)^T\mathbb{X}_{\mathrm{site}}(\mathbf{u}^l - \mathbf{u}_{\mathrm{meas}}^l)\chi_{\mathrm{snap}}^l + \frac{\alpha}{2}\mathcal{R}(\boldsymbol{\sigma}) \tag{5.6}$$

subject to the monodomain system (5.3) coupled with (5.2). Here m_b and M_b ($m_b < M_b$) are positive constants. We assume that the measurement sites are always grid points and $\mathbb{X}_{\mathrm{site}} \in \mathbb{R}^{n \times n}$ is the matrix recording observation sites. The off-diagonal entries in $\mathbb{X}_{\mathrm{site}}$ are zeros; in the diagonal, $[\mathbb{X}_{\mathrm{site}}]_{ii} = 1$ if the spatial grid x_i is an observation site and 0 otherwise. The snapshot marker χ_{snap}^l equals 1 if t^l is an observation moment and 0 otherwise.

To tackle the constrained minimization problem, we introduce the Lagrange multipliers $\mathbf{q}^l$ and $\mathbf{r}^l$, $l \in \{1, \cdots, L\}$, define the Lagrangian function

$$\begin{aligned}\mathcal{L}_{\mathrm{m}} = {}&\mathcal{J}_{\mathrm{m}} \\ &- \sum_{l=1}^{L}(\mathbf{q}^l)^T(\mathbf{A}_{\mathrm{m}}\mathbf{u}^l - \mathbf{M}\mathbf{I}_{\mathrm{app}}^l + \beta\mathbf{M}I_{\mathrm{ion}}(\tilde{\mathbf{u}}^l, \mathbf{w}^l) - \beta C_{\mathrm{m}}\mathbf{M}\sum_{i=1}^{2}\frac{\alpha_i}{\Delta t}\mathbf{u}^{l-i})\end{aligned}$$

$$-\sum_{l=1}^{L}(\mathbf{r}^l)^T\left(\frac{\mathbf{w}^l-\mathbf{w}^{l-1}}{\Delta t}+g(\tilde{\mathbf{u}}^l,\mathbf{w}^l)\right), \tag{5.7}$$

and then differentiate with respect to the state variables $\mathbf{u}^l$ and $\mathbf{w}^l$ to get the adjoint system. The adjoint algebraic form of the monodomain system (5.3) reads

$$\mathbf{A}_\mathrm{m}\mathbf{q}^l = \mathbf{d}^l \tag{5.8}$$

where the right hand side $\mathbf{d}^l$ is obtained by

$$\mathbf{d}^l = \beta(\mathbf{M}\mathbf{q}^{l+2})\circ\partial_u I_\mathrm{ion}(\tilde{\mathbf{u}}^{l+2},\mathbf{w}^{l+2}) - 2\beta(\mathbf{M}\mathbf{q}^{l+1})\circ\partial_u I_\mathrm{ion}(\tilde{\mathbf{u}}^{l+1},\mathbf{w}^{l+1})$$

$$- \partial_u g\mathbf{r}^l + \mathbb{X}_\mathrm{site}(\mathbf{u}^l-\mathbf{u}^l_\mathrm{meas})\chi^l_\mathrm{snap} + \beta C_\mathrm{m}\mathbf{M}\sum_{i=1}^{2}\frac{\alpha_i}{\Delta t}\mathbf{q}^{l+i}.$$

In particular $\mathbf{q}^{L+1} = \mathbf{0} = \mathbf{q}^{L+2}$. The operation $\circ$ means entry-wise product. The dual gating variable $\mathbf{r}^l$ is updated by

$$\frac{\mathbf{r}^{l+1}-\mathbf{r}^l}{\Delta t} = \partial_w g\mathbf{r}^l + \beta(\mathbf{M}\mathbf{q}^l_\mathbf{r})\circ\partial_w I_\mathrm{ion}(\tilde{\mathbf{u}}^l) \tag{5.9}$$

In particular $\mathbf{r}^{L+1} = \mathbf{0} = \mathbf{r}^{L+2}$.

Then based on the adjoint equations we get the derivatives of $\mathcal{J}_\mathrm{m}$ as follows

$$\frac{\mathcal{D}\mathcal{J}_\mathrm{m}}{\mathcal{D}\sigma_\mathrm{ml}} = -\sum_{l=1}^{L}(\mathbf{q}^l)^T\mathbf{S}_\mathbf{l}\mathbf{u}^l_\mathbf{r} + \frac{\alpha}{2}\frac{\partial\mathcal{R}}{\partial\sigma_\mathrm{ml}} \tag{5.10}$$

$$\frac{\mathcal{D}\mathcal{J}_\mathrm{m}}{\mathcal{D}\sigma_\mathrm{mt}} = -\sum_{l=1}^{L}(\mathbf{q}^l)^T\mathbf{S}_\mathbf{t}\mathbf{u}^l_\mathbf{r} + \frac{\alpha}{2}\frac{\partial\mathcal{R}}{\partial\sigma_\mathrm{mt}}. \tag{5.11}$$

Here $\mathbf{S}_\mathbf{l}$ and $\mathbf{S}_\mathbf{t}$ are stiffness matrices with entries

$$[\mathbf{S}_\mathbf{l}]_{jk} = \int_\Omega \mathbf{a}_\mathbf{l}\mathbf{a}_\mathbf{l}^T\nabla\phi_k\cdot\nabla\phi_j d\boldsymbol{x}, \quad [\mathbf{S}_\mathbf{t}]_{jk} = \int_\Omega(\mathbf{I}-\mathbf{a}_\mathbf{l}\mathbf{a}_\mathbf{l}^T)\nabla\phi_k\cdot\nabla\phi_j d\boldsymbol{x}.$$

Notice that the stiffness matrix $\mathbf{S}_\mathbf{m}$ actually can be computed as $\mathbf{S}_\mathbf{m} = \sigma_\mathrm{ml}\mathbf{S}_\mathbf{l} + \sigma_\mathrm{mt}\mathbf{S}_\mathbf{t}$.

The MICP can be solved by the BFGS optimization approach as stated in Chapter 3. However, the computation is intensive since each "query" of the forward system or its adjoint counterpart is performed in the full-order n by solving large-scale algebraic systems and computing high-dimensional matrix-vector operations. Moreover, if later we would like to extend the application to a pathological tissue where a scar inside has different (anomalous) values of conductivities, the number of "queries" will substantially increase due to the increase of the total number of parameters. This has been demonstrated in Sec. 3.4.2: Test 6. Altogether, in the current scenario, the MICP is too computationally expensive to be applied in clinic. This motivates us to work on a model reduction investigation with the aim of reducing the computational cost.

5.3   Model order reduction for nonlinear system

We consider in general the discrete system of a parameterized nonlinear steady differential equation

$$\mathbf{A}_\tau \mathbf{y}(\tau) = \mathbf{F}(\mathbf{y}(\tau); \tau) \tag{5.12}$$

where τ denotes the model parameter of interest in an inverse problem and is contained in a closed bounded domain $\mathcal{D}$. In case of working with an unsteady differential equation, the time t can also be treated as a parameter except for the physical parameters in the system. To simplify the notations, we consider the steady case in the description below. We assume that the matrix $\mathbf{A}_\tau \in \mathbb{R}^{n \times n}$ has affine dependence on τ, and $\mathbf{F}(\cdot)$ is a nonlinear function evaluated at the solution $\mathbf{y}(\tau) = [y_1(\tau), \cdots, y_n(\tau)]^T \in \mathbb{R}^n$ componentwise, i.e.

$$\mathbf{F}(\mathbf{y}(\tau); \tau) = [F(y_1(\tau); \tau), \cdots, F(y_n(\tau); \tau)]^T$$

with $F(\cdot)$ being a nonlinear scalar-valued function. This componentwise-evaluation form on the nonlinearity is natural in the context of finite difference (FD) discretized systems, and often in the finite element (FE) discretized systems as well for computational efficiency. In particular for a linear FE discretization, the componentwise evaluation cor-

responds to a piecewise linear approximation on the nonlinear term.

The dimension n of the full-order system (5.12), which reflects the number of *degrees of freedom* (DOF) in the finite elements, is typically very large for high-fidelity simulation. Therefore, simply solving (5.12) can be computationally demanding on execution time and memory storage.

On the other hand, even though the trajectory of solution $\mathbf{y}(\tau)$ along parameter τ belongs to the high dimensional space $\mathbb{R}^n$, the intrinsic structure of the solution manifold could features a very low dimension. We desire to construct a small set of "educated" basis functions $\{\boldsymbol{\varphi}_i\}_{i=1}^N$ (known as *reduced basis*), which should include features of the solution and therefore depends on the current problem, such that the solution $\mathbf{y}(\tau)$ can be well approximated in the space $\mathrm{span}\{\boldsymbol{\varphi}_i\}$ (called *reduced space*). Namely, the solution an be represented as

$$\mathbf{y}(\tau) = \sum_{i=1}^{N} [\mathbf{y_r}(\tau)]_i \boldsymbol{\varphi}_i$$

where $\mathbf{y_r}(\tau)$ is the vector of coordinates in the reduced space of dimension N ($N \ll n$), and without lose of generality $\{\boldsymbol{\varphi}_i\}$ is orthonormal. Let

$$\mathbb{Z}_\mathrm{y} = [\boldsymbol{\varphi}_1, \cdots, \boldsymbol{\varphi}_N] \in \mathbb{R}^{n \times N}$$

be the matrix containing the reduced basis (RB), we can rewrite the solution representation as

$$\mathbf{y}(\tau) = \mathbb{Z}_\mathrm{y} \mathbf{y_r}(\tau). \tag{5.13}$$

Mathematical model reduction aims at efficiently solving (5.12) in the reduced space $\mathrm{span}\{\boldsymbol{\varphi}_i\}$ by a Galerkin projection process. This can be achieved by plugging (5.13) into the *full-order model* (FOM) (5.12) and projecting (5.12) onto $\mathbb{Z}_\mathrm{y}$. A *reduced order model* (ROM) is then obtained

$$\underbrace{\mathbb{Z}_\mathrm{y}^T \mathbf{A}_\tau \mathbb{Z}_\mathrm{y}}_{\mathbf{A_r}} \mathbf{y_r}(\tau) = \mathbb{Z}_\mathrm{y}^T \mathbf{F}(\mathbb{Z}_\mathrm{y} \mathbf{y_r}(\tau); \tau) \tag{5.14}$$

Notice that $\mathbf{A_r} = \mathbb{Z}_y^T \mathbf{A}_\tau \mathbb{Z}_y \in \mathbb{R}^{N \times N}$ is a dense matrix but in general it features a very small size, hence the linear system (5.14) can be tackled with a direct solver. We simply omit the subscript τ here since $\mathbf{A_r}$ has affine parameter dependence.

The "educated" RB is constructed from the FOM (5.12) which is in large scale, thus the computation is usually expensive. This leads to approaches based on the *offline-online paradigm*. In the offline phase, accurate and computationally intensive simulations are performed to construct the RB. In the online phase, the ROM (5.14) is solved many times for different parameter values with remarkably lower computational costs than the FOM, by taking advantage of the "educated" basis.

Techniques for RB construction start from a sampling on the parameter τ. We introduce here a sample

$$ S = \{\tau_1, \cdots, \tau_s\} $$

consisting of s distinct parameter points in $\mathcal{D}$. Provided that the sample is proper enough, the solutions $\{\mathbf{y}(\tau_i)\}$ corresponding to the sample parameters can well represent the solution space. A RB is constructed to guarantee that for each $\tau_i \in S$ the error of approximating $\mathbf{y}(\tau_i)$ in the reduced space is controlled by a desired tolerance. We follow the POD approach, which usually constructs an "optimal" reduced basis as specified below.

5.3.1 Proper Orthogonal Decomposition (POD)

Given the sample S of parameters, we solve the FOM (5.12) for each parameter in S. The solutions are called *snapshots* and denoted by $\{\mathbf{y}_i\}_{i=1}^m$ ($m = s$ in current setting). The Proper Orthogonal Decomposition (POD) approach seeks an orthonormal *POD basis* $\{\boldsymbol{\varphi}_1, \cdots, \boldsymbol{\varphi}_N\}$ (a set of *POD modes*) in $\mathbb{R}^n$ of a given rank N ($N << m$) that can best approximate the training space $X^{trn} = \mathrm{span}\{\mathbf{y}_i\}_{i=1}^m$. The "best" means the POD basis solves the following minimizing problem

$$ \min_{\{\boldsymbol{\psi}_i\}} \sum_{j=1}^m \|\mathbf{y}_j - \sum_{i=1}^N \langle \mathbf{y}_j, \boldsymbol{\psi}_i \rangle \boldsymbol{\psi}_i\|^2 \qquad \text{s.t.} \ \langle \boldsymbol{\psi}_i, \boldsymbol{\psi}_j \rangle = \delta_{ij}. $$

Here $\sum_{i=1}^{N} \langle \mathbf{y}_j, \boldsymbol{\psi}_i \rangle \boldsymbol{\psi}_i$ is the projection of the snapshot $\mathbf{y}_j$ into the reduced space $\mathrm{span}\{\boldsymbol{\psi}_i\}_{i=1}^{N}$.

If we gather the snapshots into the so called *snapshot matrix* $\mathbf{Y} = [\mathbf{y}_1, \cdots, \mathbf{y}_{\mathrm{m}}] \in \mathbb{R}^{n \times m}$ and denote the *reduced basis matrix* by $\boldsymbol{\Psi} = [\boldsymbol{\psi}_1, \cdots, \boldsymbol{\psi}_N] \in \mathbb{R}^{n \times N}$, the minimizing problem can be rewritten as

$$\min_{\boldsymbol{\Psi}} ||\mathbf{Y} - \boldsymbol{\Psi}\boldsymbol{\Psi}^T\mathbf{Y}||_F^2 \qquad \text{s.t. } \boldsymbol{\Psi}^T\boldsymbol{\Psi} = \mathbf{I}_N.$$

We denote still by $\mathbb{Z}_y$ the matrix of the optimal basis $[\boldsymbol{\varphi}_1, \cdots, \boldsymbol{\varphi}_N] \in \mathbb{R}^{n \times N}$, classical result on low-rank approximation [87] shows that $\mathbb{Z}_y \mathbb{Z}_y^T \mathbf{Y}$ should be given by the truncated *singular value decomposition* (SVD) of $\mathbf{Y}$. To be specific, let

$$\mathbf{Y} = \mathbf{U}\boldsymbol{\Sigma}\mathbf{V}^T$$

be the SVD of $\mathbf{Y}$, where $\mathbf{U} = [\mathbf{u}_1, \cdots, \mathbf{u}_n] \in \mathbb{R}^{n \times n}$ and $\mathbf{V} = [\mathbf{v}_1, \cdots, \mathbf{v}_n] \in \mathbb{R}^{m \times m}$ are orthogonal matrices and $\boldsymbol{\Sigma} \in \mathbb{R}^{n \times m}$ has zero entries everywhere except $\boldsymbol{\Sigma}_{ii} = s_i$ with $s_1 \geq s_2 \geq \cdots \geq s_d \geq 0$ ($d = \min\{m, n\}$). The numbers s_i are called the *singular values* of $\mathbf{Y}$ and the columns of $\mathbf{U}$ ($\mathbf{V}$) are called the left (right) *singular vectors*. We can decompose the matrices as

$$\mathbf{U}\boldsymbol{\Sigma}\mathbf{V}^T = \begin{bmatrix} \mathbf{U}_N & \mathbf{U}_{n-N} \end{bmatrix} \begin{bmatrix} \boldsymbol{\Sigma}_N & \mathbf{0} \\ \mathbf{0} & \boldsymbol{\Sigma}_r \end{bmatrix} \begin{bmatrix} \mathbf{V}_N^T \\ \mathbf{V}_{m-N}^T \end{bmatrix},$$

where $\mathbf{U}_N \in \mathbb{R}^{n \times N}$ and $\mathbf{V}_N \in \mathbb{R}^{m \times N}$ contain the first N left and right singular vectors of $\mathbf{Y}$ respectively, while $\mathbf{U}_{n-N} \in \mathbb{R}^{n \times (n-N)}$ and $\mathbf{V}_{m-N} \in \mathbb{R}^{m \times (m-N)}$ contain the remaining. The matrix $\boldsymbol{\Sigma}_N \in \mathbb{R}^{N \times N}$ is diagonal. The truncated SVD of $\mathbf{Y}$ of length N is

$$\mathbf{Y}_N = \mathbf{U}_N \boldsymbol{\Sigma}_N \mathbf{V}_N^T,$$

which solves the minimizing problem as $\mathbb{Z}_y \mathbb{Z}_y^T \mathbf{Y} = \mathbf{Y}_N$. This gives $\mathbb{Z}_y^T \mathbf{Y} = \mathbb{Z}_y^T \mathbf{Y}_N$ and

leads to the solution

$$\mathbb{Z}_y = \mathbf{U}_N,$$

since $\mathbf{Y} = \mathbf{U}_N \mathbf{\Sigma}_N \mathbf{V}_N^T + \mathbf{U}_{n-N} \mathbf{\Sigma}_{n-N} \mathbf{V}_{n-N}^T$ and $\mathbf{U}_N^T \mathbf{U}_{n-N} = \mathbf{0}$. In summary, the POD modes are the first N left singular vectors of the snapshot matrix. We also have the error formula given by the low-rank approximation

$$\sum_{j=1}^{m} ||\mathbf{y}_j - \sum_{i=1}^{N} \langle \mathbf{y}_j, \boldsymbol{\varphi}_i \rangle \boldsymbol{\varphi}_i||^2 = \sum_{i=N+1}^{d} s_i^2. \tag{5.15}$$

In practice, we usually have $n >> m$, the correlation matrix $\mathbf{Y}^T\mathbf{Y} \in \mathbb{R}^{m \times m}$ is in small size and its eigen-pairs are given by $(s_i^2, \mathbf{v}_i)$. To compute the POD modes, we can compute the eigen-decomposition of $\mathbf{Y}^T\mathbf{Y}$ first and then provide

$$\boldsymbol{\varphi}_i = \mathbf{u_i} = \frac{1}{s_i} \mathbf{Y} \mathbf{v}_i \qquad i = 1, \cdots, N. \tag{5.16}$$

If $n << m$ in a special case, the correlation matrix $\mathbf{Y}\mathbf{Y}^T$ should be considered instead, and the POD modes are the eigenvectors of $\mathbf{Y}\mathbf{Y}^T$.

Alternatively, an efficient way for computing the POD modes through snapshot matrix $\mathbf{Y}$ is to first compute the *thin QR factorization* of $\mathbf{Y}$ as $\mathbf{Y} = \mathbf{QR}$, and then compute the SVD of the small matrix $\mathbf{R} \in \mathbb{R}^{m \times m}$ as $\mathbf{R} = \mathbf{U}_R \mathbf{S}_R \mathbf{V}_R^T$. Finally the POD modes can be extracted in order from the columns of $\mathbf{Q}\mathbf{U}_R$.

Snapshots selection / Sampling

In practice, it is often easier to capture the fluctuations if we subtract the mean $\bar{\mathbf{y}} = \frac{1}{m} \sum_{i=1}^{m} \mathbf{y}_i$ from each snapshot. That is, we compute the POD basis $\mathbb{Z}_y$ from the shifted snapshot matrix $\mathbf{Y} = [\mathbf{y}_1 - \bar{\mathbf{y}}, \cdots, \mathbf{y}_m - \bar{\mathbf{y}}]$. In this case, the full-order solution will be reconstructed as $\mathbf{y}(\tau) = \bar{\mathbf{y}} + \mathbb{Z}_y \mathbf{y_r}(\tau)$. Without lose of generality, we assume later that the snapshot mean is zero.

In constructing the POD basis, the choice of parameters over which snapshots are

computed can greatly affect the quality of the resulting ROM. This is because the scope of snapshots determines the domain of effectiveness of the reduced basis. Sampling is thus a crucial issue that needs to be addressed in reduced basis construction.

Standard sampling schemes used in the offline phase include uniform sampling, random sampling, the Latin hypercube sampling (LHS) method [82], and the centroidal voronoi tessellation (CVT) sampling method [42]. When sampling a high-dimensional parameter space, which is obviously challenging, the greedy sampling method was used [24, 68, 110]. The key feature of greedy sampling is to adaptively select a parameter at which the estimate of the solution error in the ROM is maximized. The error is either estimated by a rigorous and effective *a posteriori* error estimator [68, 110] or by solving a model-constrained optimization problem [24]. The previous one is applicable only to a limited class of problems where an error estimator is achievable.

For optimal control applications, several online adaptive sampling procedures have been proposed to let the sampling procedure take into account the optimization trajectory. The Trust Region POD [4] approach proposed by Arian et al. constructs successively improved POD bases according to parameter values (control values) updated during optimization. The updating procedure was embedded with the trust region method which determines whether after an optimization step the POD basis should be updated. Kunisch and Volkwein introduced the Optimality System POD (OS-POD, [74]) which also successively updates the POD basis, but the main feature lies in the fact that the associated POD-reduced system is computed from the trajectory corresponding to the optimal control value. This was achieved by adding the full-order system as a constraint in the reduced optimization problem. Carlberg and Farhat proposed a goal-oriented framework called Compact POD [27] using snapshots of the full-order model solutions as well as their derivatives (known as *sensitivities*) with respect to the model parameters of interest. That is

$$\left[\mathbf{y}(\tau_1), \frac{d\mathbf{y}}{d\tau}(\tau_1), \cdots, \mathbf{y}(\tau_s), \frac{d\mathbf{y}}{d\tau}(\tau_s) \right]. \tag{5.17}$$

Remark. In the field of statistics, the POD is also called the *Principal component analysis*

(PCA). Descriptions concerning the PCA date from 1901 given by Karl Pearson [102]. It is a statistical tool mostly used in exploratory data analysis and dimensionality reduction.

In the PCA terminology, data are gathered in the observation matrix $\mathbf{Y} \in \mathbb{R}^{n \times m}$ usually with the columns denoting m random variables and the rows denoting n observations on the random variables. This matrix corresponds to the transpose of the snapshot matrix that we have mentioned in describing POD. The purpose of PCA is to identify the intrinsic structure behind a set of multivariate interrelated observations in order to obtain a compact description of it. This is achieved by transforming the observations to a set of values of linearly uncorrelated variables called *principal components*, which are orthogonal and ordered so that the first few have the largest possible variances. These principal components are given by the eigenvectors of the covariance matrix.

5.3.2   Discrete Empirical Interpolation Method (DEIM)

In the reduced system (5.14) obtained by the POD projection, we have to evaluate the nonlinear term

$$\mathbf{n}(\tau) = \underbrace{\mathbb{Z}_{\mathrm{y}}^T}_{N \times n} \underbrace{\mathbf{F}(\mathbb{Z}_{\mathrm{y}}\mathbf{y}_{\mathbf{r}}(\tau); \tau)}_{n \times 1}. \tag{5.18}$$

This requires a matrix-vector multiplication $\mathbb{Z}_{\mathrm{y}}\mathbf{y}_{\mathbf{r}}(\tau)$ for reconstructing the full-order solution, an evaluation of the nonlinearity $\mathbf{F}(\cdot)$, and a matrix-vector multiplication $\mathbb{Z}_{\mathrm{y}}^T\mathbf{F}(\cdot)$ for projection. All these operations have computational complexity depending on the size n of the full-order system (5.12), which is possibly in the magnitude of hundred thousand. Therefore, solving the ROM (5.14) is almost as expensive as solving the full one. This inefficiency exists as well while solving the adjoint system of (5.14).

The complexity of evaluating (5.18) can be made independent of the full order size n by using the Discrete Empirical Interpolation Method (DEIM). The DEIM provides an interpolation approximation for the nonlinear term $\mathbf{F}(\mathbb{Z}_{\mathrm{y}}\mathbf{y}_{\mathbf{r}}(\tau); \tau)$ (simply denoted as $\mathbf{f}(\tau)$) by a projection onto a low-dimensional subspace. For this purpose, we require a subspace with basis $\{\mathbf{z}_1, \cdots, \mathbf{z}_M\}$ such that $\mathbf{f}(\tau)$ is approximately contained in $\mathrm{span}\{\mathbf{z}_1, \cdots, \mathbf{z}_M\}$

for the arguments τ of interest. Typically, one can sample τ, take snapshots of $\mathbf{f}(\tau)$ computed from the FOM with the samples, and then apply the POD on the snapshots to extract a projection basis $\{\mathbf{z}_1, \cdots, \mathbf{z}_M\}$. We need that $M << n$ to guarantee a computationally efficient DEIM approximation of $\mathbf{f}$.

Let $\mathbb{Z}_{\mathrm{f}} = [\mathbf{z}_1, \cdots, \mathbf{z}_M] \in \mathbb{R}^{n \times M}$, the approximation of $\mathbf{f}$ is in the form

$$\mathbf{f} \approx \hat{\mathbf{f}} = \mathbb{Z}_{\mathrm{f}}\mathbf{c}.$$

To determine the coefficient vector $\mathbf{c}$, the DEIM optimally extracts M distinguished rows from the over-determined system $\mathbf{f} = \mathbb{Z}_{\mathrm{f}}\mathbf{c}$. Specifically, the DEIM computes row indices $p_1, \cdots, p_M$ in $\{1, ..., n\}$ and requires:

$$[\mathbf{f}]_{p_i} = [\hat{\mathbf{f}}]_{p_i}. \tag{5.19}$$

If we denote $\mathrm{P} = [\mathbf{e}_{p_1}, \cdots, \mathbf{e}_{p_M}] \in \mathbb{R}^{n \times M}$ with $\mathbf{e}_{p_i}$ being the p_i-th unit vector in $\mathbb{R}^n$, the coefficient vector $\mathbf{c}$ is solved from above interpolation property by

$$\mathrm{P}^T\mathbf{f} = (\mathrm{P}^T\mathbb{Z}_{\mathrm{f}})\mathbf{c}$$

while $\mathrm{P}^T\mathbb{Z}_{\mathrm{f}}$ is nonsingular. Finally the approximation of $\mathbf{f}$ writes

$$\mathbf{f} \approx \hat{\mathbf{f}} = \mathbb{Z}_{\mathrm{f}}\mathbf{c} = \mathbb{Z}_{\mathrm{f}}(\mathrm{P}^T\mathbb{Z}_{\mathrm{f}})^{-1}\mathrm{P}^T\mathbf{f} = \mathbb{Z}_{\mathrm{f}}(\mathrm{P}^T\mathbb{Z}_{\mathrm{f}})^{-1}\mathbf{F}(\mathrm{P}^T\mathbb{Z}_{\mathbf{y}_{\mathbf{r}}}(\tau); \tau). \tag{5.20}$$

The last equality in (5.20) follows from the assumption that the function $\mathbf{F}(\cdot)$ evaluates component-wise at its input vector. The nonlinear term mentioned in (5.18) can then be efficiently computed through

$$\mathbf{n}(\tau) \approx \underbrace{\mathbb{Z}_{\mathrm{y}}^T\mathbb{Z}_{\mathrm{f}}(\mathrm{P}^T\mathbb{Z}_{\mathrm{f}})^{-1}}_{N \times M}\underbrace{\mathbf{F}(\mathrm{P}^T\mathbb{Z}_{\mathrm{y}}\mathbf{y}_{\mathbf{r}}(\tau); \tau)}_{M \times 1} \tag{5.21}$$

Notice that the matrices $\mathbb{Z}_{\mathrm{y}}^T\mathbb{Z}_{\mathrm{f}}(\mathrm{P}^T\mathbb{Z}_{\mathrm{f}})^{-1} \in \mathbb{R}^{N \times M}$ and $\mathrm{P}^T\mathbb{Z}_{\mathrm{y}} \in \mathbb{R}^{M \times N}$ are in low dimen-

---

Algorithm 2 DEIM [30]

Input: $\{\mathbf{z}_l\}_{l=1}^M \subseteq \mathbb{R}^n$ linear independent
Output: indices $\mathbf{p} = [p_1, \cdots, p_M]^T \in \mathbb{R}^M$, $\mathbf{M}$ as the inverse of $\mathrm{P}^T \mathbb{Z}_\mathrm{f}$
 1: $[|\rho|, p_1] = \max\{|\mathbf{z}_1|\}$
 2: $\mathbb{Z}_\mathrm{f} \leftarrow [\mathbf{z}_1]$, $\mathrm{P} \leftarrow [\mathbf{e}_{p_1}]$, $\mathbf{p} \leftarrow [p_1]$, $\mathbf{M} \leftarrow \rho^{-1}$
 3: **for** $l = 2, \cdots, M$ **do**
 4: $\quad$ Solve $(\mathrm{P}^T \mathbb{Z}_\mathrm{f})\mathbf{c} = \mathrm{P}^T \mathbf{z}_l$
 5: $\quad$ $\mathbf{r} = \mathbf{z}_l - \mathbb{Z}_\mathrm{f}\mathbf{c}$
 6: $\quad$ $[|\rho|, p_l] = \max\{|\mathbf{r}|\}$
 7: $\quad$ $\mathbf{a}^T = \mathbf{e}_{p_l}^T \mathbb{Z}_\mathrm{f}$
 8:

$$
\mathbf{M} \leftarrow
\begin{bmatrix}
\mathbf{I} & -\mathbf{c} \\
\mathbf{0} & 1
\end{bmatrix}
\begin{bmatrix}
\mathbf{M} & \mathbf{0} \\
-\rho^{-1}\mathbf{a}^T\mathbf{M} & \rho^{-1}
\end{bmatrix}
$$

 9: $\quad$ $\mathbb{Z}_\mathrm{f} \leftarrow [\mathbb{Z}_\mathrm{f}\ \mathbf{z}_l]$, $\mathrm{P} \leftarrow [\mathrm{P}\ \mathbf{e}_{p_l}]$, $\mathbf{p} \leftarrow [\mathbf{p}^T\ p_l]^T$
10: **end for**

---

sions (usually in a magnitude of ten) and they can be precomputed so that afterwards the computational complexity of evaluating $\mathbf{n}(\tau)$ is in the order of only $\mathcal{O}(MN)$.

The interpolation indices $\mathbf{e}_{p_1}, \cdots, \mathbf{e}_{p_M}$ are selected inductively from the projection basis $\{\mathbf{z}_1, \cdots, \mathbf{z}_M\}$ by the DEIM algorithm (Algorithm 2). At each iteration, an interpolation index is selected to limit growth of the error bound of the approximation $\hat{\mathbf{f}}$. In particular, the first index p_1 is the index on which $\mathbf{z}_1$ has the largest magnitude; each of the remaining indices p_l is the index on which the residual of approximating $\mathbf{z}_l$ by the first $l-1$ basis vectors $\{\mathbf{z}_1, \cdots, \mathbf{z}_{l-1}\}$ has the largest magnitude.

It is demonstrated that the DEIM algorithm is well-defined ([30], lem. 2.2.2): $\mathrm{P}^T\mathbf{Z}_\mathrm{f}$ is non-singular in each iteration of Algorithm 2 and the interpolation indices are non-repeated. The selection of the interpolation points depends on the basis $\{\mathbf{z}_i\}_{i=1}^M$, however, once the set of DEIM interpolation indices $\{p_i\}_{i=1}^M$ is determined from $\{\mathbf{z}_i\}_{i=1}^M$, the DEIM approximation is independent of the choice of basis spanning the space $\mathrm{Range}(\mathbf{Z}_\mathrm{f})$ [30].

5.4   POD-DEIM for the inverse conductivity problem

In this section, we apply the POD-DEIM approach to the monodomain inverse conductivity problem.

5.4.1   POD-DEIM on the monodomain model

The POD basis

In construction of reduced basis for the parameterized monodomain model, two ways can be followed as mentioned in [17]. One is to store a set of solutions of the full-order model computed at different instants in time with a set of different parameters in a given sample space, then collect all these solutions to build a unique snapshot matrix, upon which the POD basis is finally built. In other words, we treat the conductivity parameter σ and also the time t as parameters of the model. Another way for the reduced basis construction is to build multiple POD bases instead of a unique one. Each POD basis is constructed from the snapshots of solutions computed with a particular conductivity parameter, which we call generating parameter and denote by σ_{gen}. In a generic use of the bases for the monodomain model with a given parameter σ_{giv}, the POD basis whose generating parameter is the closest to σ_{giv} among all will be selected.

We point out that the dynamic of the transmembrane potential u is not quite smooth in time, due to the wavefront propagation or the upstroke (depolarization) spreading. Therefore, the singular values of the snapshot matrix of u do not decay fast. We confirm this by a numerical experiment shown in Fig. 5.2 (left). In this test, the time step $\Delta t = 0.05$ ms and the full-order model dimension is 24272. We collected snapshots of the transmembrane potential u (and the ionic current I_{ion}) computed with a fixed conductivity parameter $\sigma = [3, 1]$ for 500 time steps. The feature of slow decay shown by Fig. 5.2 (left) is exceptional as compared with classical problems, in which singular values of a snapshot matrix usually decrease fast hence few POD modes are enough to give an accurate approximation of the solution considered. For example, the singular val-
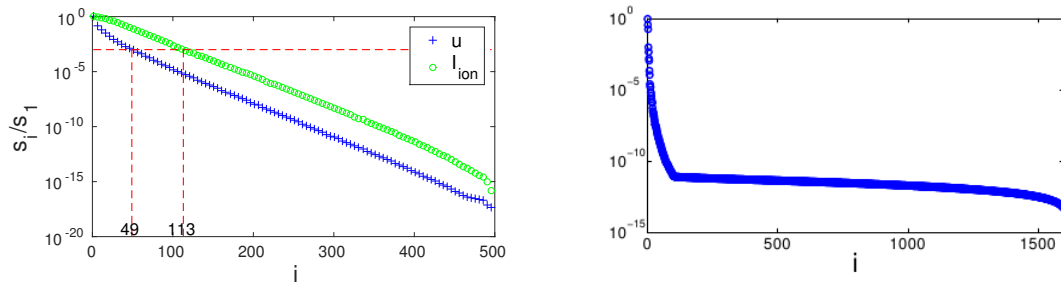
Figure 5.2: Left: singular values of snapshot matrices of the transmembrane potential u and ionic current I_{ion} generated by one parameter. Right: singular values of a snapshot matrix of the fluid velocity in the Navier–Stokes equation generated by multiple parameters [14].

ues of a snapshot matrix of the fluid velocity, computed in a fluid-structure interaction problem [14] with different values of the Young modulus at different time instants, are displayed in Fig. 5.2 right. In this singular-value plot, there is an obvious kink which does not exist in Fig. 5.2 left.

Fig. 5.2 (left) shows that the singular value s_i of snapshots of the transmembrane potential relative to the leading singular value s_1 decays to 10^{-3} (red dash line in Fig. 5.2) when i is 49 (113 for the ionic current). Referring to the error formula (5.15) this corresponds to a "cut" of POD modes where the relative approximation error has a magnitude of 10^{-6}, since the error is the sum of squares of insignificant s_i's. It suggests that u (I_{ion}) can still be well approximated by a POD basis of dimension less than 50 (120), if the model parameter is close to the generating parameter of the POD basis. We also observe that the ionic current I_{ion} features even more complex nonlinearity than the transmembrane potential u, since more POD modes are needed for approximating the ionic current with the same accuracy as approximating the transmembrane potential.

We stress here that the way to build a unique POD basis actually provides worthless results. This can be identified from Fig. 5.3, in which the leading 500 singular values of snapshots generated by four different conductivity parameters are reported. The relative singular value s_i/s_1 of snapshots of the transmembrane u decays to 10^{-3} (red dash line in Fig. 5.3) when i is 136 (399 for the ionic current). Compared with the one-parameter case shown in Fig. 5.2, a combination of snapshots from different parameters does not
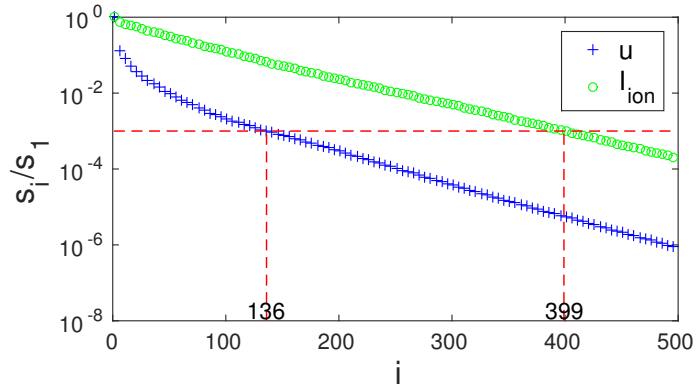
Figure 5.3: Singular values of snapshot matrices of u and I_{ion} generated by four parameters.

reduce the number of POD modes necessary for accurate POD approximation.

Snapshots of sensitivities

It is also interesting to investigate the effectiveness of adding snapshots of sensitivities in POD basis construction aimed at improving approximation accuracy. For this purpose, we describe below the sensitivity equation of the monodomain model.

Applying differentiation with respect to σ_{ml} on the monodomain model ((5.3) and (5.5) coupled with (5.2)), we have

$$\frac{\partial \mathbf{A}_{\mathrm{m}}}{\partial \sigma_{\mathrm{ml}}} \mathbf{u}^{l+1} + \mathbf{A}_{\mathrm{m}} \frac{\partial \mathbf{u}^{l+1}}{\partial \sigma_{\mathrm{ml}}} = \frac{\partial \mathbf{b}^{l+1}}{\partial \sigma_{\mathrm{ml}}}. \tag{5.22}$$

If we detail those derivatives involved, the sensitivity $\dfrac{\partial \mathbf{u}^{l+1}}{\partial \sigma_{\mathrm{ml}}}$ can then be solved from

$$\mathbf{A}_{\mathrm{m}} \frac{\partial \mathbf{u}^{l+1}}{\partial \sigma_{\mathrm{ml}}} = \beta C_{\mathrm{m}} \mathbf{M} \sum_{i=1}^{2} \frac{\alpha_i}{\Delta t} \frac{\partial \mathbf{u}^{l+1-i}}{\partial \sigma_{\mathrm{ml}}} - \mathbf{S}_{\mathrm{l}} \mathbf{u}^{l+1}$$
$$- \beta \mathbf{M}[\partial_u I_{\mathrm{ion}}(\tilde{\mathbf{u}}^{l+1}, \mathbf{w}^{l+1}) \circ \frac{\partial \tilde{\mathbf{u}}^{l+1}}{\partial \sigma_{\mathrm{ml}}} + \partial_w I_{\mathrm{ion}}(\tilde{\mathbf{u}}^{l+1}, \mathbf{w}^{l+1}) \circ \frac{\partial \mathbf{w}^{l+1}}{\partial \sigma_{\mathrm{ml}}}], \tag{5.23}$$

where $\dfrac{\partial \mathbf{w}^{l+1}}{\partial \sigma_{\mathrm{ml}}}$ is updated by

$$\frac{\frac{\partial \mathbf{w}^{l+1}}{\partial \sigma_{ml}} - \frac{\partial \mathbf{w}^{l}}{\partial \sigma_{ml}}}{\Delta t} + \partial_u g \frac{\partial \tilde{\mathbf{u}}^{l+1}}{\partial \sigma_{\mathrm{ml}}} + \partial_w g \frac{\partial \mathbf{w}^{l+1}}{\partial \sigma_{\mathrm{ml}}} = \mathbf{0}. \tag{5.24}$$

The sensitivity $\dfrac{\partial \mathbf{u}^{l+1}}{\partial \sigma_{\mathrm{mt}}}$ is solved very similarly. The sensitivity of the ionic current, stated in the continuous form without lose of generality, can be evaluated through

$$\frac{\partial I_{\mathrm{ion}}}{\partial \sigma_{\mathrm{mk}}} = \partial_u I_{\mathrm{ion}} \frac{\partial u}{\partial \sigma_{\mathrm{mk}}} + \partial_w I_{\mathrm{ion}} \frac{\partial w}{\partial \sigma_{\mathrm{mk}}}$$

where k stands for l or t.

Application of DEIM

To start, we assume that the reduced bases for the transmembrane potential u and the ionic current I_{ion} have been built at hand as $\mathbb{Z}_{\mathrm{u}}$ and $\mathbb{Z}_{\mathrm{ion}}$ respectively. If we project the discrete monodomain system (5.3, 5.5) onto the reduced space $\mathbb{Z}_{\mathrm{u}}$, we obtain

$$\begin{cases} \mathbb{Z}_{\mathrm{u}}^T \mathbf{A}_{\mathrm{m}} \mathbb{Z}_{\mathrm{u}} \mathbf{u}_{\mathbf{r}}^{l+1} = \mathbf{b}_{\mathbf{r}}^{l+1} \qquad l \in \{0, 1, \cdots, L-1\} \\[2mm] \text{with} \quad \mathbf{b}_{\mathbf{r}}^{l+1} = \mathbb{Z}_{\mathrm{u}}^T \mathbf{b}^{l+1} = \underbrace{\mathbb{Z}_{\mathrm{u}}^T \mathbf{M} \mathbf{I}_{\mathrm{app}}^{l+1}}_{N \times 1} + \beta C_{\mathrm{m}} \underbrace{\mathbb{Z}_{\mathrm{u}}^T \mathbf{M} \mathbb{Z}_{\mathrm{u}}}_{N \times N} \sum_{i=1}^{2} \frac{\alpha_i}{\Delta t} \underbrace{\mathbf{u}_{\mathbf{r}}^{l+1-i}}_{N \times 1} \\[2mm] \qquad\qquad -\beta \underbrace{\mathbb{Z}_{\mathrm{u}}^T \mathbf{M}}_{N \times n} \underbrace{I_{\mathrm{ion}}(\mathbb{Z}_{\mathrm{u}} \tilde{\mathbf{u}}_{\mathbf{r}}^{l+1}, \mathbf{w}^{l+1})}_{n \times 1} \end{cases} \tag{5.25}$$

where $\mathbf{u}_{\mathbf{r}}^{l+1}$ is the solution at time $t = t^l$ in the reduced space and $\tilde{\mathbf{u}}_{\mathbf{r}}^{l+1}$ is its second-order extrapolation.

As pointed out previously, although the system is in a reduced form, for the presence of the nonlinear terms the computational cost still depends on the number of degrees of freedom n of the full-order system. To be specific, the complexity in computing the nonlinear term I_{ion} in the right hand side is $\mathcal{O}(n)$, and the complexity in multiplying I_{ion} by $\mathbb{Z}_{\mathrm{u}} \mathbf{M} \in \mathbb{R}^{N \times n}$ is $\mathcal{O}(Nn)$. As discussed in Sec. 5.3.2, the complexity mainly results from the fact that $I_{\mathrm{ion}}(\mathbb{Z}_{\mathrm{u}} \tilde{\mathbf{u}}_{\mathbf{r}}^{l+1}, \mathbf{w}^{l+1})$ cannot be precomputed, since it depends nonlin-

early on the full-order vector $\mathbb{Z}_\mathrm{u}\widetilde{\mathbf{u}}_\mathbf{r}^{l+1}$ and $\mathbf{w}^{l+1}$. We will apply DEIM approximation to $I_\mathrm{ion}(\mathbb{Z}_\mathrm{u}\widetilde{\mathbf{u}}_\mathbf{r}^{l+1}, \mathbf{w}^{l+1})$ in the following.

We use the POD basis $\mathbb{Z}_\mathrm{ion} \in \mathbb{R}^{n \times M}$ of snapshots of I_ion as an input basis for the DEIM algorithm, where M is the number of POD modes. The DEIM algorithm generates interpolation indices $\mathbf{p} = [p_1, \cdots, p_M]^T$ for constructing the extraction matrix P. The DEIM approximation is then

$$I_\mathrm{ion}(\mathbb{Z}_\mathrm{u}\widetilde{\mathbf{u}}_\mathbf{r}^{l+1}, \mathbf{w}^{l+1}) \approx \underbrace{\mathbb{Z}_\mathrm{ion}(\mathrm{P}^T\mathbb{Z}_\mathrm{ion})^{-1}}_{n \times M} I_\mathrm{ion}(\underbrace{\mathrm{P}^T\mathbb{Z}_u\widetilde{\mathbf{u}}_\mathbf{r}^{l+1}}_{M \times 1}, \underbrace{\mathrm{P}^T\mathbf{w}^{l+1}}_{M \times 1}). \quad (5.26)$$

If we set

$$\mathbf{A}_\mathbf{r} = \mathbb{Z}_\mathrm{u}^T\mathbf{A}_\mathrm{m}\mathbb{Z}_\mathrm{u} \in \mathbb{R}^{N \times N}, \ \mathbf{I}_\mathbf{r}^{l+1} = \mathbb{Z}_\mathrm{u}^T\mathbf{M}\mathbf{I}_\mathrm{app}^{l+1} \in \mathbb{R}^{N \times 1}, \ \mathbf{M}_\mathrm{u} = \mathbb{Z}_\mathrm{u}^T\mathbf{M}\mathbb{Z}_\mathrm{u} \in \mathbb{R}^{N \times N},$$

$$\mathbf{M}_\mathrm{iu} = \underbrace{\mathbb{Z}_\mathrm{u}^T\mathbf{M}}_{N \times n}\underbrace{\mathbb{Z}_\mathrm{ion}(\mathrm{P}^T\mathbb{Z}_\mathrm{ion})^{-1}}_{n \times M} \in \mathbb{R}^{N \times M}, \ \mathrm{U} = \mathrm{P}^T\mathbb{Z}_\mathrm{u} \in \mathbb{R}^{M \times N}, \ \mathbf{w}_\mathbf{r}^{l+1} = \mathrm{P}^T\mathbf{w}^{l+1} \in \mathbb{R}^{M \times 1},$$

the reduced monodomain system is then formulated as

$$\begin{cases} \mathbf{A}_\mathbf{r}\mathbf{u}_\mathbf{r}^{l+1} = \mathbf{I}_\mathbf{r}^{l+1} + \beta C_\mathrm{m}\mathbf{M}_\mathrm{u} \sum_{i=1}^{2} \frac{\alpha_i}{\Delta t}\mathbf{u}_\mathbf{r}^{l+1-i} - \beta\mathbf{M}_\mathrm{iu}I_\mathrm{ion}(\mathrm{U}\widetilde{\mathbf{u}}_\mathbf{r}^{l+1}, \mathbf{w}_\mathbf{r}^{l+1}) \\ \frac{\mathbf{w}_\mathbf{r}^{l+1} - \mathbf{w}_\mathbf{r}^l}{\Delta t} = -g(\mathrm{U}\widetilde{\mathbf{u}}_\mathbf{r}^{l+1}, \mathbf{w}_\mathbf{r}^{l+1}). \end{cases} \quad (5.27)$$

5.4.2 The reduced monodomain inverse conductivity problem

After the monodomain model reduction, we can then formulate the reduced MICP as: find $\boldsymbol{\sigma} = [\sigma_\mathrm{ml}, \sigma_\mathrm{mt}] \in [m_b, M_b]^2$ that minimizes the functional

$$\mathcal{J}_\mathrm{r}(\boldsymbol{\sigma}) = \frac{1}{2}\sum_{l=1}^{L}(\mathbb{Z}_\mathrm{u}\mathbf{u}_\mathbf{r}^l - \mathbf{u}_\mathrm{meas}^l)^T\mathbb{X}_\mathrm{site}(\mathbb{Z}_\mathrm{u}\mathbf{u}_\mathbf{r}^l - \mathbf{u}_\mathrm{meas}^l)\chi_\mathrm{snap}^l + \frac{\alpha}{2}\mathcal{R}(\boldsymbol{\sigma}) \quad (5.28)$$

subject to the reduced monodomain system (5.27). In order to have linear algebra operations of complexity only $\mathcal{O}(N)$ in computing the values of this cost function $\mathcal{J}_\mathrm{r}$, we can

rewrite

$$\mathcal{J}_{\mathrm{r}}(\boldsymbol{\sigma}) = \frac{1}{2} \sum_{l=1}^{L} ((\mathbf{u}_{\mathbf{r}}^l)^T \mathbf{X}_{\mathrm{u}} \mathbf{u}_{\mathbf{r}}^l - 2(\widehat{\mathbf{u}}_{\mathrm{meas}}^l)^T \mathbf{u}_{\mathbf{r}}^l + \|\widehat{\widehat{\mathbf{u}}}_{\mathrm{meas}}^l\|^2) \chi_{\mathrm{snap}}^l + \frac{\alpha}{2} \mathcal{R}(\boldsymbol{\sigma}) \tag{5.29}$$

where $\mathbf{X}_{\mathrm{u}} = \mathbb{Z}_{\mathrm{u}}^T \mathbb{X}_{\mathrm{site}} \mathbb{Z}_{\mathrm{u}} \in \mathbb{R}^{N \times N}$. The projected measurements $\widehat{\mathbf{u}}_{\mathrm{meas}}^l = \mathbb{Z}_{\mathrm{u}}^T \mathbb{X}_{\mathrm{site}} \mathbf{u}_{\mathrm{meas}}^l \in \mathbb{R}^{N \times 1}$ and $\widehat{\widehat{\mathbf{u}}}_{\mathrm{meas}}^l = \mathbb{X}_{\mathrm{site}} \mathbf{u}_{\mathrm{meas}}^l \in \mathbb{R}^{n \times 1}$ can be precomputed.

We still follow the Lagrange argument to acquire the adjoint system. Let us denote

$$\mathbf{u}_{\mathbf{r}}^{1 \cdots L} = \begin{bmatrix} \mathbf{u}_{\mathbf{r}}^1 \\ \vdots \\ \mathbf{u}_{\mathbf{r}}^L \end{bmatrix} \qquad \mathbf{w}_{\mathbf{r}}^{1 \cdots L} = \begin{bmatrix} \mathbf{w}_{\mathbf{r}}^1 \\ \vdots \\ \mathbf{w}_{\mathbf{r}}^L \end{bmatrix} \qquad \mathbf{q}_{\mathbf{r}}^{1 \cdots L} = \begin{bmatrix} \mathbf{q}_{\mathbf{r}}^1 \\ \vdots \\ \mathbf{u}_{\mathbf{q}}^L \end{bmatrix} \qquad \mathbf{r}_{\mathbf{r}}^{1 \cdots L} = \begin{bmatrix} \mathbf{r}_{\mathbf{r}}^1 \\ \vdots \\ \mathbf{r}_{\mathbf{r}}^L \end{bmatrix}$$

where $\mathbf{q}_{\mathbf{r}}^{1 \cdots L}$ and $\mathbf{r}_{\mathbf{r}}^{1 \cdots L}$ are the Lagrange multipliers. We define the Lagrangian functional

$$\mathcal{L}_{\mathrm{r}}(\mathbf{u}_{\mathbf{r}}^{1 \cdots L}, \mathbf{w}_{\mathbf{r}}^{1 \cdots L}, \boldsymbol{\sigma}, \mathbf{q}_{\mathbf{r}}^{1 \cdots L}, \mathbf{r}_{\mathbf{r}}^{1 \cdots L}) = \mathcal{J}_{\mathrm{r}}(\boldsymbol{\sigma})$$

$$- \sum_{l=1}^{L} (\mathbf{q}_{\mathbf{r}}^l)^T (\mathbf{A}_{\mathbf{r}} \mathbf{u}_{\mathbf{r}}^l - \mathbf{I}_{\mathbf{r}}^l - \beta C_{\mathrm{m}} \mathbf{M}_{\mathrm{u}} \sum_{i=1}^{2} \frac{\alpha_i}{\Delta t} \mathbf{u}_{\mathbf{r}}^{l-i} + \beta \mathbf{M}_{\mathrm{iu}} I_{\mathrm{ion}}(\mathrm{U}\widetilde{\mathbf{u}}_{\mathbf{r}}^l, \mathbf{w}_{\mathbf{r}}^l))$$

$$- \sum_{l=1}^{L} (\mathbf{r}_{\mathbf{r}}^l)^T (\frac{\mathbf{w}_{\mathbf{r}}^l - \mathbf{w}_{\mathbf{r}}^{l-1}}{\Delta t} + g(\mathrm{U}\widetilde{\mathbf{u}}_{\mathbf{r}}^l, \mathbf{w}_{\mathbf{r}}^l)) \tag{5.30}$$

The adjoint form of the reduced discretized monodomain system can be constructed by setting $\frac{\partial \mathcal{L}_{\mathrm{r}}}{\partial \mathbf{u}_{\mathbf{r}}^l} = 0$ for $l = 1, \cdots, L$. It reads

$$\mathbb{Z}_{\mathrm{u}}^T \mathbf{A} \mathbb{Z}_{\mathrm{u}} \mathbf{q}_{\mathbf{r}}^l = \mathbf{d}_{\mathbf{r}}^l \qquad l \in \{1, \cdots, L\} \tag{5.31}$$

with

$$\mathbf{d}_{\mathbf{r}}^l = \beta \mathrm{U}^T \{\mathbf{M}_{\mathrm{iu}}^T \mathbf{q}_{\mathbf{r}}^{l+2}\} \circ \partial_u I_{\mathrm{ion}}(\mathrm{U}\widetilde{\mathbf{u}}_{\mathbf{r}}^{l+2}, \mathbf{w}_{\mathbf{r}}^{l+2}) - 2\beta \mathrm{U}^T \{\mathbf{M}_{\mathrm{iu}}^T \mathbf{q}_{\mathbf{r}}^{l+1}\} \circ \partial_u I_{\mathrm{ion}}(\mathrm{U}\widetilde{\mathbf{u}}_{\mathbf{r}}^{l+1}, \mathbf{w}_{\mathbf{r}}^{l+1})$$

$$- \partial_u g \mathrm{U}^T \widetilde{\mathbf{r}}_{\mathbf{r}}^l + (\mathbf{X}_{\mathrm{u}} \mathbf{u}_{\mathbf{r}}^l - \widehat{\mathbf{u}}_{\mathrm{meas}}^l) \chi_{\mathrm{snap}}^l + \beta C_{\mathrm{m}} \mathbf{M}_{\mathrm{u}} \sum_{i=1}^{2} \frac{\alpha_i}{\Delta t} \mathbf{q}_{\mathbf{r}}^{l+i}.$$

Algorithm 3 Optimization-POD-DEIM

Input: initial guess $\boldsymbol{\sigma}^0$, POD basis $\{\mathbb{Z}_u^i\}_{i=1}^s$ and $\{\mathbb{Z}_{\text{ion}}^i\}_{i=1}^s$, POD bases generating parameters $\{\boldsymbol{\sigma}_{\text{gen}}^i\}_{i=1}^s$

Output: estimated conductivity values $\boldsymbol{\sigma}$

1: $\boldsymbol{\sigma} \leftarrow \boldsymbol{\sigma}^0$
2: $k \leftarrow 0, i_0 \leftarrow -1$
3: **while** $k < k_{\text{max}}$ and not converged **do**
4:     Search $i_* = arg \min\limits_{1 \le j \le s} ||\boldsymbol{\sigma} - \boldsymbol{\sigma}_{\text{gen}}^j||$
5:     **if** $(i_* \ne i_0)$ **then**
6:         Import the POD basis $\mathbb{Z}_u^{i_*}$ and $\mathbb{Z}_{\text{ion}}^{i_*}$
7:         $i_0 \leftarrow i_*$
8:     **end if**
9:     Solve $\mathbf{u_r}^{1 \cdots L}$ with $\boldsymbol{\sigma}$ from t^1 to t^L, using bases $\mathbb{Z}_u^{i_*}$ and $\mathbb{Z}_{\text{ion}}^{i_*}$
10:    Compute the cost function value $\mathcal{J}_r(\boldsymbol{\sigma})$
11:    Solve $\mathbf{q_r}^{1 \cdots L}$ with $\boldsymbol{\sigma}$ from t^L to t^1, using bases $\mathbb{Z}_u^{i_*}$ and $\mathbb{Z}_{\text{ion}}^{i_*}$
12:    Compute the gradient $\nabla \mathcal{J}_r(\boldsymbol{\sigma})$ of $\mathcal{J}_r$ using (5.33)–(5.34)
13:    Update the inverse Hessian approximation and compute the search direction $\boldsymbol{v}^k$ (BFGS [98])
14:    Set $\boldsymbol{\sigma} = \boldsymbol{\sigma} + \gamma_k \boldsymbol{v}^k$ where $\gamma_k \in (0, \infty)$ is computed from an Armijo line search
15:    $k \leftarrow k + 1$
16: **end while**

The dual gating variable $\mathbf{r}_\mathbf{r}^l$ is updated by the equation below derived from setting $\frac{\partial \mathcal{L}_r}{\partial \mathbf{w}_\mathbf{r}^l} = 0$ for $l = 1, \cdots, L$:

$$\frac{\mathbf{r}_\mathbf{r}^{l+1} - \mathbf{r}_\mathbf{r}^l}{\Delta t} = \partial_w g \mathbf{r}_\mathbf{r}^l + \beta \{\mathbf{M}_{\text{iu}}^T \mathbf{q}_\mathbf{r}^l\} \circ \partial_w I_{\text{ion}}(\mathrm{U}\tilde{\mathbf{u}}_\mathbf{r}^l, \mathbf{w}_\mathbf{r}^l). \tag{5.32}$$

In particular for the superscripts exceeding L, we have $\mathbf{q}_\mathbf{r}^{L+1} = \mathbf{0} = \mathbf{q}_\mathbf{r}^{L+2}$ and $\mathbf{r}_\mathbf{r}^{L+1} = \mathbf{0} = \mathbf{r}_\mathbf{r}^{L+2}$.

Based on the adjoint equations we then get the derivatives of $\mathcal{J}_r$

$$\frac{\mathcal{D}\mathcal{J}_r}{\mathcal{D}\sigma_{\text{ml}}} = -\sum_{l=1}^{L} (\mathbf{q}_\mathbf{r}^l)^T \mathbf{S}_{\text{lu}} \mathbf{u}_\mathbf{r}^l + \frac{\alpha}{2} \frac{\partial \mathcal{R}}{\partial \sigma_{\text{ml}}} \tag{5.33}$$

$$\frac{\mathcal{D}\mathcal{J}_r}{\mathcal{D}\sigma_{\text{mt}}} = -\sum_{l=1}^{L} (\mathbf{q}_\mathbf{r}^l)^T \mathbf{S}_{\text{tu}} \mathbf{u}_\mathbf{r}^l + \frac{\alpha}{2} \frac{\partial \mathcal{R}}{\partial \sigma_{\text{mt}}} \tag{5.34}$$

where $\mathbf{S}_{\text{lu}} = \mathbb{Z}_u^T \mathbf{S_l} \mathbb{Z}_u \in \mathbb{R}^{N \times N}$, $\mathbf{S}_{\text{tu}} = \mathbb{Z}_u^T \mathbf{S_t} \mathbb{Z}_u \in \mathbb{R}^{N \times N}$. Notice that $\mathbf{A_r} = \mathbb{Z}_u^T \mathbf{A}_\text{m} \mathbb{Z}_u = \mathbb{Z}_u^T (\beta C_\text{m} \frac{\alpha_0}{\Delta t} \mathbf{M} + \mathbf{S_m}) \mathbb{Z}_u = \beta C_\text{m} \frac{\alpha_0}{\Delta t} \mathbf{M}_\text{u} + \sigma_{\text{ml}} \mathbf{S}_{\text{lu}} + \sigma_{\text{mt}} \mathbf{S}_{\text{tu}}$.

The reduced inverse conductivity problem is eventually solved by Algorithm 3. In particular, the norm $|| \cdot ||$ in step 4 of Algorithm 3 could be customized.

5.5   Numerical results

5.5.1   POD-DEIM on the forward problem

To investigate the performance of the POD-DEIM model reduction technique on the monodomain system, we solved the ROM on a slab $\Omega = [0, 5] \times [0, 5] \times [0, 0.5] \subseteq \mathbb{R}^3$ with 24272 mesh nodes. In each simulation, five stimuli of $I_{\mathrm{app}} = 10^5$ μA/cm^3 were applied with four at the corners and one at the center of the domain for a duration of 1 ms. We setted the fibers to be constantly along the x-axis. The snapshots for POD basis construction were taken every 0.05 ms with a duration of 25 ms.

In Fig. 5.4, we plot the first six POD modes of the transmembrane potential constructed from snapshots of u that were computed with conductivity parameter $\boldsymbol{\sigma}_{\mathrm{gen}} = [3, 2]$. The parameter chosen has $\sigma_{\mathrm{ml}}/\sigma_{\mathrm{mt}}$ close to one, which makes the tissue almost isotropic. This explains why the wave front propagated from the center of the slab tissue is kind of circular. We also plot in Fig. 5.5 the leading POD modes of the transmembrane potential constructed with $\boldsymbol{\sigma}_{\mathrm{gen}} = [4, 0.1]$. The wave front in this case is kind of elliptic since the ratio $\sigma_{\mathrm{ml}}/\sigma_{\mathrm{mt}}$ is considerably greater than one. The corresponding POD modes of the ionic current I_{ion} constructed with $\boldsymbol{\sigma}_{\mathrm{gen}} = [3, 2]$ and $\boldsymbol{\sigma}_{\mathrm{gen}} = [4, 0.1]$ are plotted in Fig. 5.6.

The comparison between Fig. 5.4 and 5.5 suggests that the POD modes constructed with different conductivity parameters are very weakly correlated. Therefore, the approach of extracting POD modes from combined snapshots computed with different parameters can not achieve enough dimension reduction, as shown by Fig. 5.3.

To check the stability and accuracy of reduced order modeling, we took a uniform sampling on the conductivity parameters: 25 parameter values were generated over the domain $[1, 5] \times [0, 2]$. For each parameter, a POD basis of the transmembrane potential
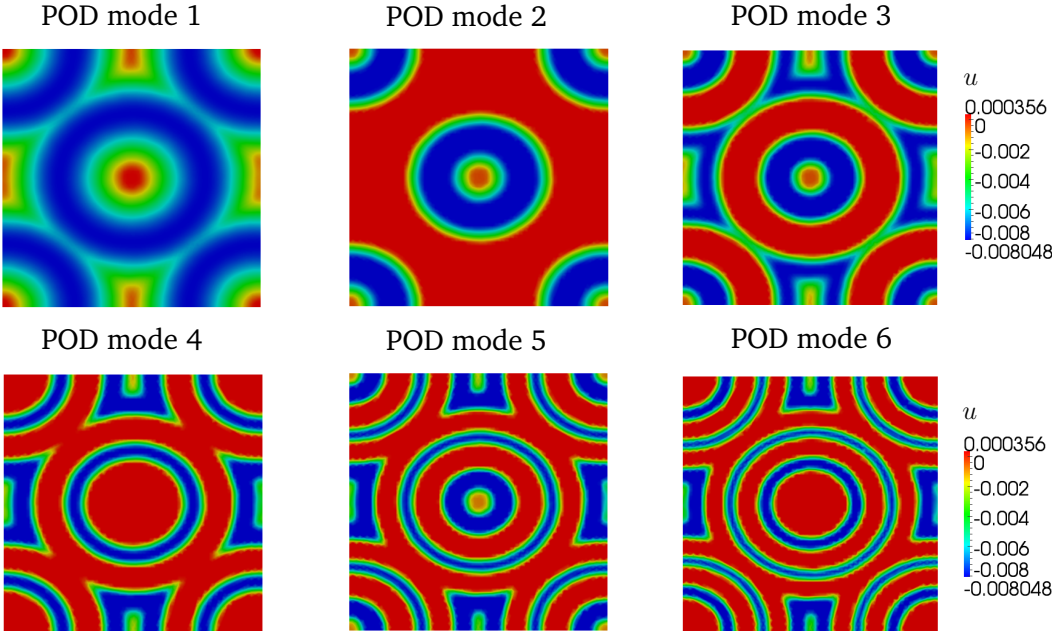
Figure 5.4: POD modes of the transmembrane potential constructed with $\boldsymbol{\sigma}_{\mathrm{gen}} = [3, 2]$.
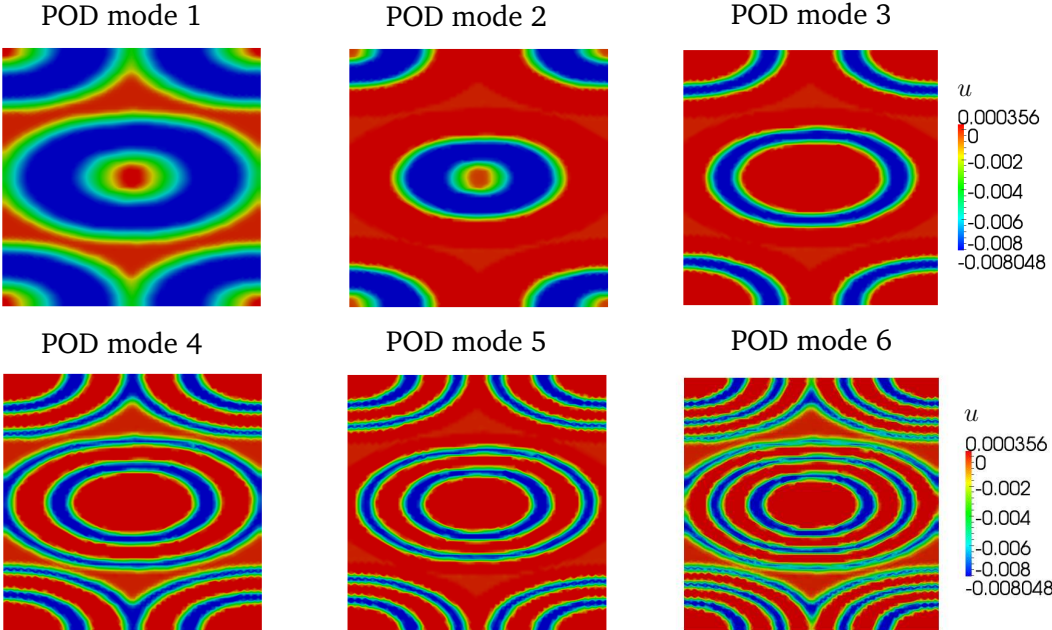
Figure 5.5: POD modes of the transmembrane potential constructed with $\boldsymbol{\sigma}_{\mathrm{gen}} = [4, 0.1]$.
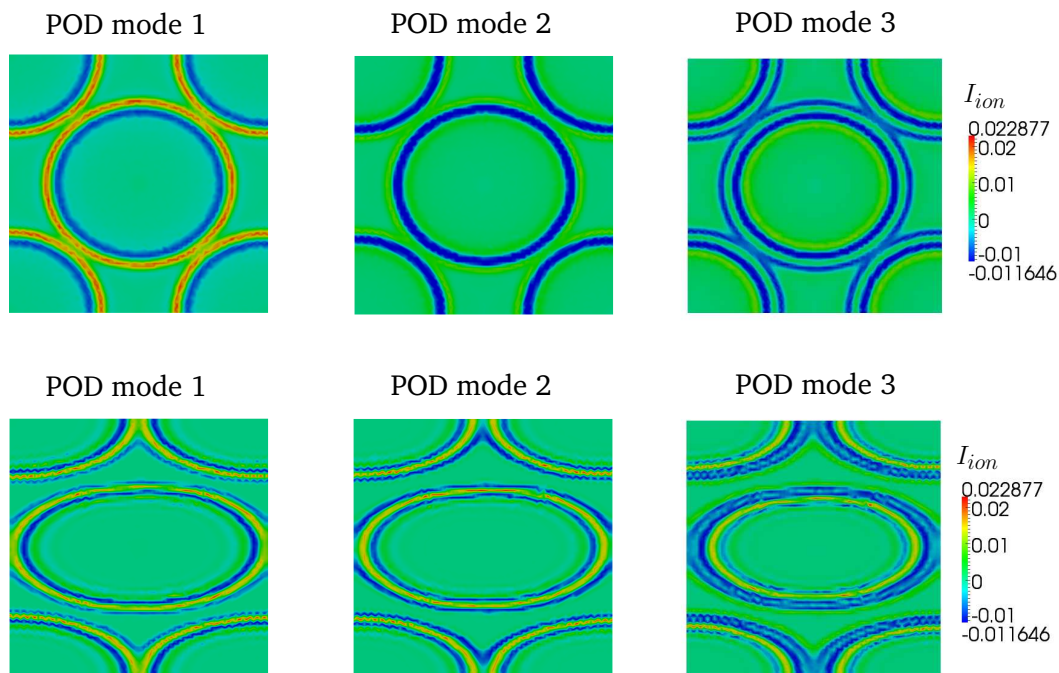
Figure 5.6: Top: POD modes of the ionic current constructed with $\boldsymbol{\sigma}_{\text{gen}} = [3, 2]$. Bottom: POD modes of the ionic current constructed with $\boldsymbol{\sigma}_{\text{gen}} = [4, 0.1]$.

Figure 5.7: Errors of u by POD-DEIM approximation. Left: errors w.r.t. the dimension of the POD basis, with $\dim(\mathbb{Z}_{\text{u}})$ ranging from 34 to 46 and $\dim(\mathbb{Z}_{\text{ion}})$ ranging from 82 to 106 ; Right: errors on 16×16 different conductivity parameters, with fixed POD-basis dimensions: $\dim(\mathbb{Z}_{\text{u}}) = 45$ and $\dim(\mathbb{Z}_{\text{ion}}) = 100$.

(ionic current) was constructed offline from snapshots computed with that parameter. In this way, 25 POD bases were available for importing during online computation of the reduced-order monodomain model.

Fig. 5.7 reports the relative error on the the transmembrane potential computed by the POD-DEIM approach. The errors in Fig. 5.7 (left) are with respect to the dimension of the POD basis, with $\dim(\mathbb{Z}_\mathrm{u})$ ranging from 34 to 46 and $\dim(\mathbb{Z}_\mathrm{ion})$ ranging from 82 to 106. The test conductivity parameter is $\boldsymbol{\sigma} = [2.6, 1.05]$. We observe that the POD-DEIM method provides stable and accurate approximation when the POD basis dimension is around 40 for u and 90 for I_ion.
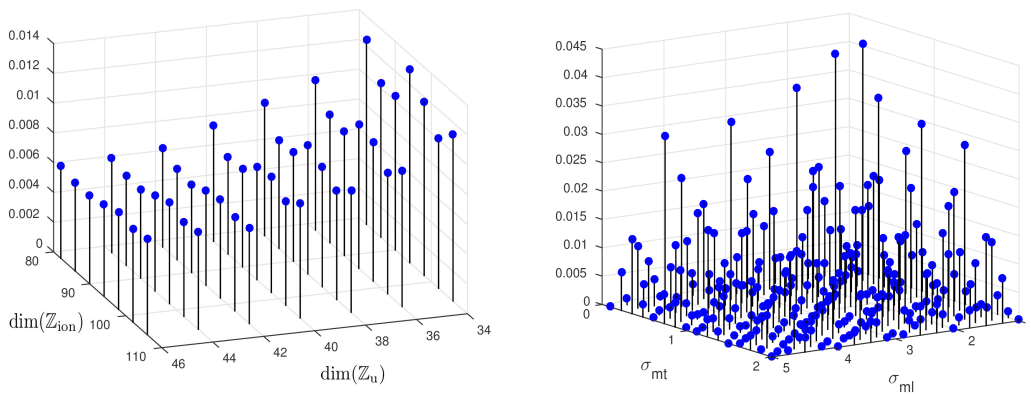
In Fig. 5.7 (right) we plot the errors on 16×16 different conductivity parameters, with fixed POD-basis dimensions: $\dim(\mathbb{Z}_\mathrm{u}) = 45$ and $\dim(\mathbb{Z}_\mathrm{ion}) = 100$. We observe that 60.55% of the parameters in this test lead errors below 0.005, 21.48% of them lead errors greater than 0.01 and they are mainly associated with conductivities at the boundary of the sample space. These errors indicate that a uniform sampling with 25 parameters would be inappropriate for its use in the inverse problem of conductivity estimation, this is confirmed by other non-reported numerical tests.

5.5.2   Domain of effectiveness (DOE) of the reduced basis

As we have mentioned in the Introduction section of Chapter 3, the monodomain model is strongly sensitive to the ratio of the longitudinal and tangential conductivities. This statement could be explained by a comparison of the POD modes in Fig. 5.4 and Fig. 5.5. As $\frac{\sigma_\mathrm{ml}}{\sigma_\mathrm{mt}} \approx 1$ (= 1.5 for $\boldsymbol{\sigma}_\mathrm{gen}$ in Fig. 5.4), the wavefront propagated from the center is close to a spherical shape; while $\frac{\sigma_\mathrm{ml}}{\sigma_\mathrm{mt}} >> 1$ (= 40 for $\boldsymbol{\sigma}_\mathrm{gen}$ in Fig. 5.5), the wavefront shape is rather elliptic. We claim that the conductivity ratio $\frac{\sigma_\mathrm{ml}}{\sigma_\mathrm{mt}}$ is the main factor upon which the transmembrane potential and accordingly the effectiveness of a reduced basis depend. A single reduced basis is particularly applicable or effective on a specific domain of the parameter space, which we will call the *domain of effectiveness* (DOE). Therefore, we carry out a supportive study on the domains of effectiveness of different reduced bases,
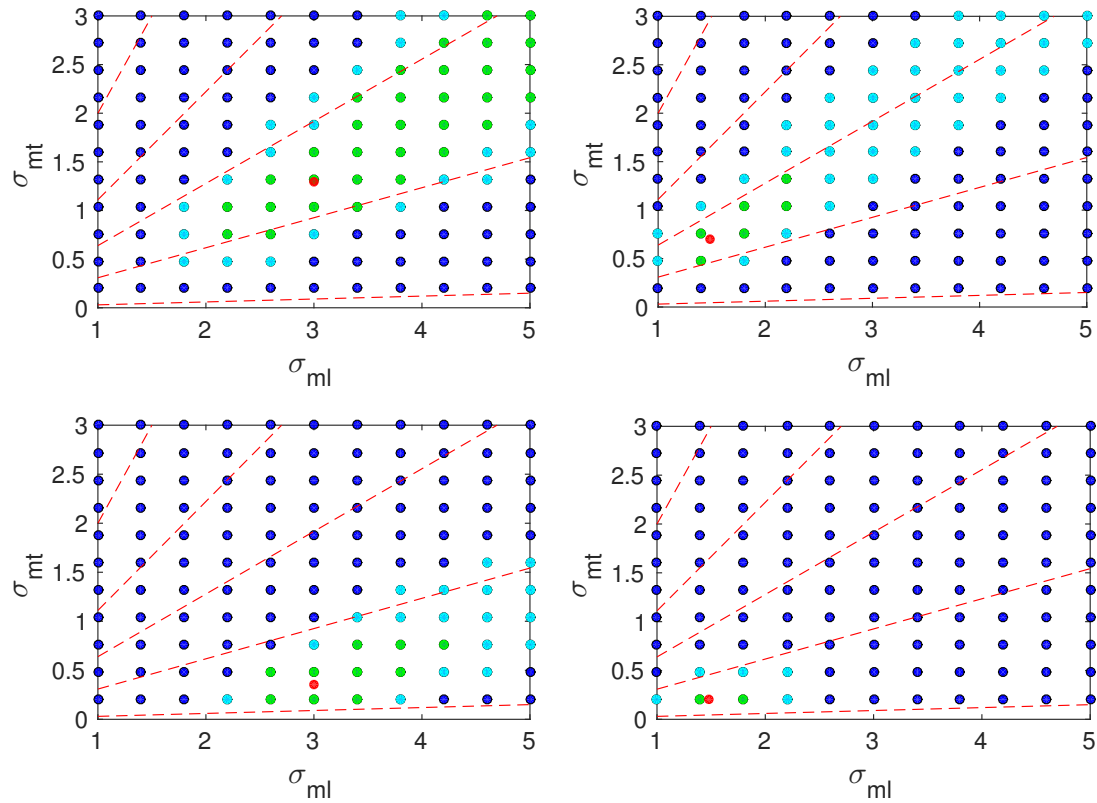
Figure 5.8: Domains of effectiveness of different reduced bases. The errors (denoted by e) of the ROM solutions are indicated in different colors. Green: $e \leq 0.002$, cyan: $0.002 < e \leq 0.005$, blue: $e > 0.005$. The parameter space is partitioned by the red dash lines using an equi-spaced partition on the range of $\arctan(\frac{\sigma_{\mathrm{mt}}}{\sigma_{\mathrm{ml}}})$. The POD basis generating parameter $\boldsymbol{\sigma}_{\mathrm{gen}}$ in each picture is indicated by a red point. Upperleft: $\boldsymbol{\sigma}_{\mathrm{gen}} = [3, 1.3]$; Upperright: $\boldsymbol{\sigma}_{\mathrm{gen}} = [1.48, 0.7]$; Lowerleft: $\boldsymbol{\sigma}_{\mathrm{gen}} = [3, 0.35]$; Lowerright: $\boldsymbol{\sigma}_{\mathrm{gen}} = [1.48, 0.2]$.

while each basis has a unique generating parameter $\boldsymbol{\sigma}_{\mathrm{gen}}$ that is different from others in the conductivity ratio.

Given a POD basis $\mathbb{Z}_{\mathrm{u}}$ and a test parameter $\boldsymbol{\sigma}$, we measure the effectiveness of $\mathbb{Z}_{\mathrm{u}}$ at $\boldsymbol{\sigma}$ by the relative error of reduced-order solution

$$
e(\boldsymbol{\sigma}) = \frac{\displaystyle\sum_{l=1}^{L} ||\mathbb{Z}_{\mathrm{u}}\mathbf{u}_{\mathbf{r}}^{l} - \mathbf{u}^{l}||^2}{\displaystyle\sum_{l=1}^{L} ||\mathbf{u}^{l}||^2}
$$

where $\mathbf{u}^{l}$ is the full-order solution at time t^{l} given $\boldsymbol{\sigma}$ and $\mathbf{u}_{\mathbf{r}}^{l}$ is the corresponding reduced-order solution solved with the reduced basis $\mathbb{Z}_{\mathrm{u}}$. We study the domains of effectiveness

of different reduced bases and plot them in Fig. 5.8. In each picture, a unique generating parameter $\boldsymbol{\sigma}_{\mathrm{gen}}$ (indicated by the red point) was used for the construction of the reduced basis. The reduced-order simulation errors are less than 0.002 at green points, between 0.002 and 0.005 at cyan points, and greater than 0.005 at blue points. The area of our interest is the neighbourhood containing those green points and cyan points, therefore we consider this area as the domain of effectiveness of the associated reduced basis.

In Fig. 5.8, the parameter space is partitioned by the red dash lines using an equi-spaced partition on the range of $\arctan(\frac{\sigma_{\mathrm{mt}}}{\sigma_{\mathrm{ml}}})$. It is interesting to see that the domain of effectiveness of a reduced basis is apparently confined to an angular region of its generating parameter. The region is wide while σ_{ml} and/or σ_{mt} are relatively large (as in Fig. 5.8 upperleft and lowerleft), and it is narrow while σ_{ml} and σ_{mt} are relatively small (as in Fig. 5.8 upperright and lowerright). This study supports the claim that the transmembrane potentials solved from the monodomain model are strongly sensitive to the conductivity ratio and amplitude.

A natural idea to enlarge the domain of effectiveness of a reduced basis is to include extra sensitivity snapshots in the POD basis construction. Following the idea in Compact POD [27], we took snapshots for the transmembrane potential u as

$$\left[\mathbf{u}^1, \delta_{\mathrm{l}} \frac{\partial \mathbf{u}^1}{\partial \sigma_{\mathrm{ml}}}, \delta_{\mathrm{t}} \frac{\partial \mathbf{u}^1}{\partial \sigma_{\mathrm{mt}}}, \cdots, \mathbf{u}^L, \delta_{\mathrm{l}} \frac{\partial \mathbf{u}^L}{\partial \sigma_{\mathrm{ml}}}, \delta_{\mathrm{t}} \frac{\partial \mathbf{u}^L}{\partial \sigma_{\mathrm{mt}}} \right],$$

where δ_{l} and δ_{t} are scaling factors applied on the sensitivity snapshots. We also took snapshots for the ionic current I_{ion} in a similar way. To investigate the feasibility of this concept, we fixed a generating parameter $\boldsymbol{\sigma}_{\mathrm{gen}} = [3, 0.35]$ and would like to compare the DOE of the sensitivity-based RB with the older one shown in Fig. 5.8 lowerleft. Two sets of scaling factors were chosen in a way such that

$$\boldsymbol{\sigma}_{\mathrm{gen}} + [\delta_{\mathrm{l}}, \delta_{\mathrm{t}}] = [3.8, 1.32] \qquad \boldsymbol{\sigma}_{\mathrm{gen}} + [\delta_{\mathrm{l}}, \delta_{\mathrm{t}}] = [4.2, 0.48].$$

Two reduced bases were generated accordingly and their DOE are plotted in Fig. 5.9.
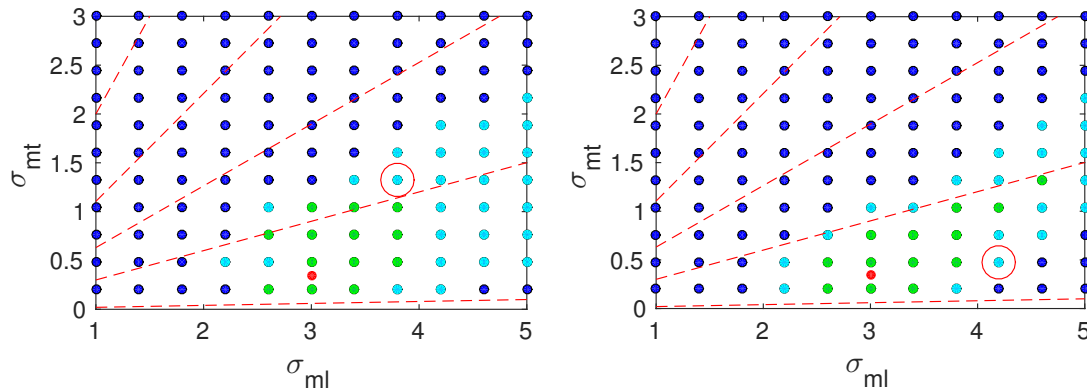
Figure 5.9: Domains of effectiveness of sensitivity-based reduced bases both generated by $\boldsymbol{\sigma}_{\text{gen}} = [3, 0.35]$. The left one is based on $\boldsymbol{\sigma}_{\text{gen}} + [\delta_l, \delta_t] = [3.8, 1.32]$ (marked by the red circle) and the right one takes $\boldsymbol{\sigma}_{\text{gen}} + [\delta_l, \delta_t] = [4.2, 0.48]$ (marked by the red circle).

The ROM in this test took 100 POD modes for u and 250 for I_{ion} which are appropriate numbers based on our experience. From this test, we discover that adding sensitivity snapshots is not effective for widening the DOE. In addition, the largely increased necessary number of POD modes makes this idea not feasible for application in inverse problem such as conductivity estimation.

5.5.3   POD-DEIM on the inverse problem

The measures

Considering the lose of accuracy in using the reduced-order model, we may need to acquire more measures to maintain the stability of the inverse conductivity solver. For this purpose, we can increase the number of measurement sites in space and the number of snapshots in time. In the following tests, we used 100×100 measurement sites on the tissue surface, which is achievable in experiments that we are carrying out with Professor Flavio Fenton at Georgia Institute of Technology. We took snapshot for a duration of $T = 30$ ms.

   The DEIM approximation for nonlinearity was applied under the assumption that the nonlinear term I_{ion} was evaluated pointwise in the full order, which is equivalent to a piece-wise linear finite element approximation. We state that this assumption greatly im-
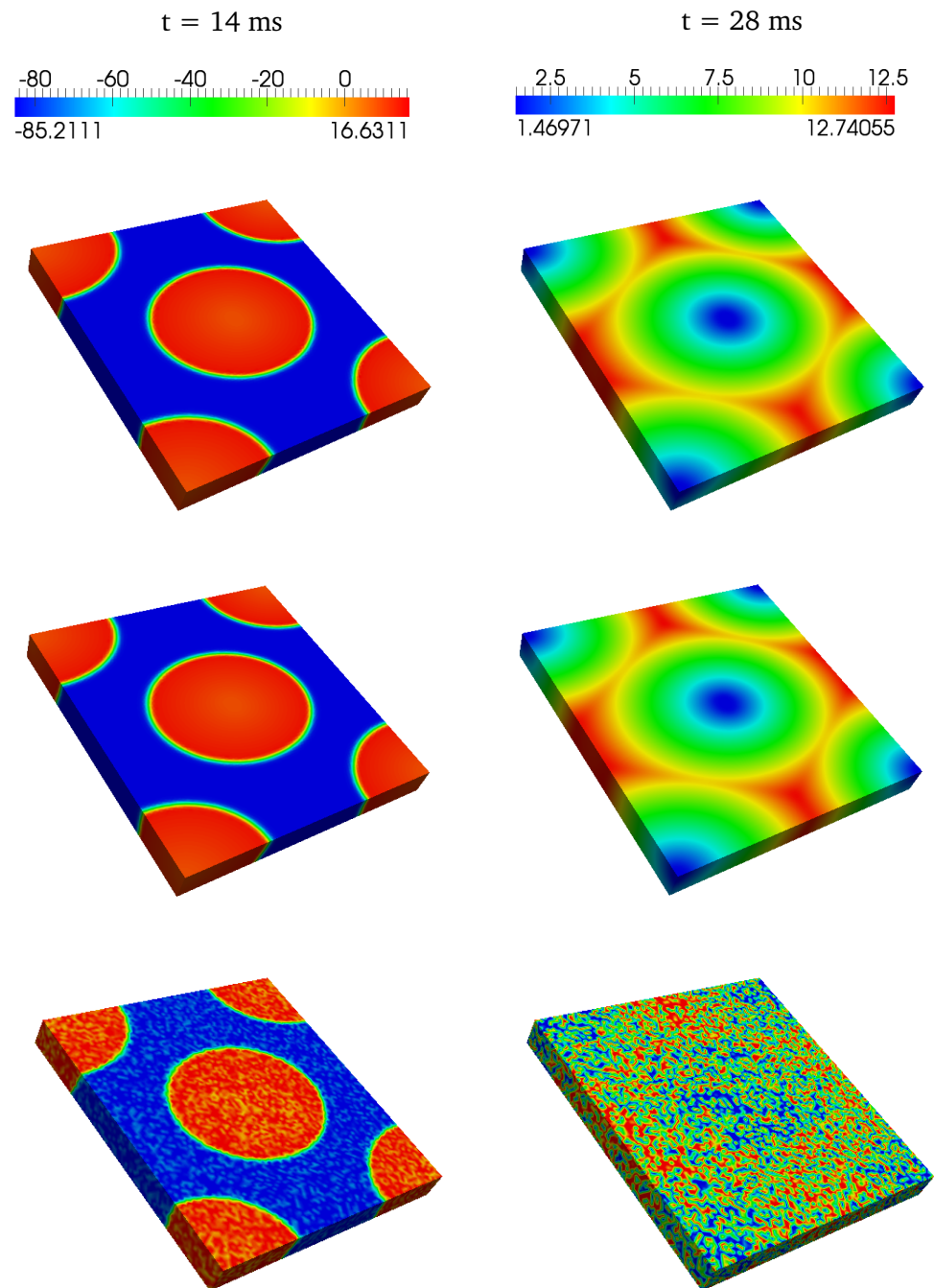
Figure 5.10: Row 1: u computed with exact finite element approximation on the nonlinear term I_{ion}; Row 2: u computed with point-wise evaluation on the nonlinear term I_{ion}; Row 3: synthetic measure of u generated from Row 1 by adding 15% noise uniformly

proves the computational efficiency of the full-order system while keeping enough accuracy when the mesh is fine. This is verified by a numerical experiment shown in Fig. 5.10. In this test the mesh contains 76832 nodes. As one can see, the pointwise computation on I_{ion} (Row 2 of Fig. 5.10) presents ignorable error as compared with the exact finite element approximation (Row 1 of Fig. 5.10). More importantly, the computational cost is reduced to 7.07% from 759.284 seconds to 53.6954 seconds. Row 3 of Fig. 5.10 displays the synthetic measures generated by adding 15% noise to the potential u computed with exact evaluation of I_{ion}. This typically represents the way we generate measures in future tests of the reduced inverse solver.

Sampling

We have reported in Sec. 5.5.1 that a uniform sampling on the conductivity parameter is not feasible: it needs too many sample points and the corresponding ROM approximation still lacks accuracy at many test points. However, based on the DOE study in Sec. 5.5.2, we can find a way that substantially decreases the number of sample points while still keeps the ROM approximation having enough accuracy. This has been achieved by sampling the polar coordinates of the conductivity values to take full advantage of the angular feature of the DOE. One typical example is shown in Fig. 5.11. In this sampling, the Gauss–Lobatto nodes were used to densify the "boundary layer" of the parameter space.

Conductivity estimation

In the following, we conduct a group of tests on the performance of the POD-DEIM approach applied in the inverse conductivity problem, using the ten samples plotted in Fig. 5.11. Six test points (plotted in blue in Fig. 5.11) were carefully chosen so that they are not too close to the sample points. With each test point, we solved the full-order monodomain equation without using pointwise computation on nonlinearity and then added 15% noise to the solution to generate the synthetic measures of the transmembrane po-
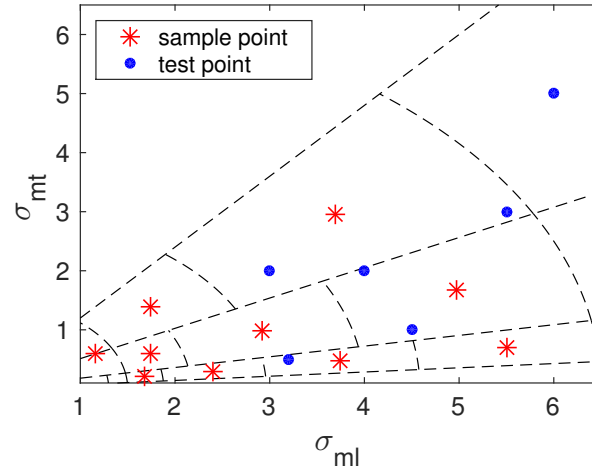
Figure 5.11: Ten samples (in red) generated by sampling the polar coordinates of conductivity values. The "boundary layer" of the sample space is densified by the use of Gauss–Lobatto nodes.

tential. The measurement snapshots were taken every 2 ms. We performed the numerical experiments on a 76832-node mesh and also a 24272-node mesh with a common simulation time step $\Delta t = 0.025$ ms. In each running of the reduced inverse conductivity solver, 35 POD modes were taken for u and 80 for I_{ion}, the norm $|| \cdot ||$ in step 4 of Algorithm 3 was taken as the Euclidean norm of the polar coordinates. The optimization iteration started from a fixed initial guess $\boldsymbol{\sigma}_{\text{initial}} = [1.5, 1]$ and was constrained by a maximum iteration number 40. We further restricted the admissible domain of the conductivities into $[1, 7] \times [0.05, 7]$ and constrained it by the condition $\frac{\sigma_{\text{ml}}}{\sigma_{\text{mt}}} \geq 0.8$, inspired from conductivity measures listed in Table 3.1.

The estimated conductivities are listed in Table 5.1 and Table 5.2 where the results correspond to the 76832-node mesh and the 24272-node mesh respectively. From Table 5.1 we can see: on average each solve of the reduced monodomain system (or its dual), including reduced basis importing, takes about only 3 ms as compared with 140 ms for the full-order model. In the 24272-node case, 1.5 ms would be compared with 38 ms. It is consistent that the computational cost reduction on the forward problem is in two order of magnitudes. For conductivity estimation, the reduced inverse solver returns

Table 5.1: Conductivity estimation on a slab mesh with DOF = 76832. $T = 30$ ms, $\Delta t = 0.025$ ms, $dt_{\text{snap}} = 2$ ms, noise = 15%, $\boldsymbol{\sigma}_{\text{initial}} = [1.5, 1]$.

	$\boldsymbol{\sigma}_{\text{exact}}$	$\boldsymbol{\sigma}_{\text{estimated}}$	# fwd | bwd	Total exe. time	Exe. time/solve
Full Order	[3.2, 0.5]	[3.237 0.625]	29 | 17	6211 s	135.02 s
POD+DEIM	[3.2, 0.5]	[3.161 0.393]	89 | 41	439.6 s	3.38 s
Full Order	[4.5, 1]	[4.535 1.099]	46 | 35	11160 s	137.78 s
POD+DEIM	[4.5, 1]	[4.596 0.974]	73 | 41	353.1 s	3.10 s
Full Order	[5.5, 3]	[5.528 3.064]	41 | 41	12780 s	155.85 s
POD+DEIM	[5.5, 3]	[5.384 3.053]	60 | 41	246.6 s	2.44 s
Full Order	[4, 2]	[4.045 2.076]	27 | 27	7525 s	144.71 s
POD+DEIM	[4, 2]	[3.764 1.968]	90 | 41	396.1 s	3.02 s
Full Order	[3, 2]	[3.054 2.077]	15 | 15	4199 s	139.97 s
POD+DEIM	[3, 2]	[2.490 2.434]	107 | 31	396.1 s	2.87 s
Full Order	[6, 5]	[5.854 5.121]	41 | 41	12870 s	156.95 s
POD+DEIM	[6, 5]	[4.820 5.836]	41 | 41	131.6 s	1.60 s

Table 5.2: Conductivity estimation on a slab mesh with DOF = 24272. $T = 30$ ms, $\Delta t = 0.025$ ms, $dt_{\text{snap}} = 2$ ms, noise = 15%, $\boldsymbol{\sigma}_{\text{initial}} = [1.5, 1]$.

|	$\boldsymbol{\sigma}_{\text{exact}}$	$\boldsymbol{\sigma}_{\text{estimated}}$	# fwd | bwd	Total exe. time	Exe. time/solve
Full Order	[3.2, 0.5]	[3.441 0.853]	21 | 15	1362 s	37.83 s
POD+DEIM	[3.2, 0.5]	[3.414 0.802]	69 | 41	179 s	1.63 s
Full Order	[4.5, 1]	[4.723 1.318]	37 | 37	2873 s	38.82 s
POD+DEIM	[4.5, 1]	[4.871 1.067]	31 | 26	81.66 s	1.43 s
Full Order	[5.5, 3]	[5.656 3.283]	41 | 41	3161 s	38.55 s
POD+DEIM	[5.5, 3]	[5.871 3.593]	63 | 41	160.3 s	1.54 s
Full Order	[4, 2]	[4.246 2.281]	37 | 37	2837 s	38.34 s
POD+DEIM	[4, 2]	[4.361 2.384]	72 | 41	194.4 s	1.72 s
Full Order	[3, 2]	[3.255 2.280]	22 | 22	1688 s	38.36 s
POD+DEIM	[3, 2]	[3.445 1.933]	44 | 41	97.81 s	1.15 s
Full Order	[6, 5]	[5.994 5.351]	41 | 41	3136 s	38.24 s
POD+DEIM	[6, 5]	[5.310 6.637]	20 | 19	48.9 s	1.25 s
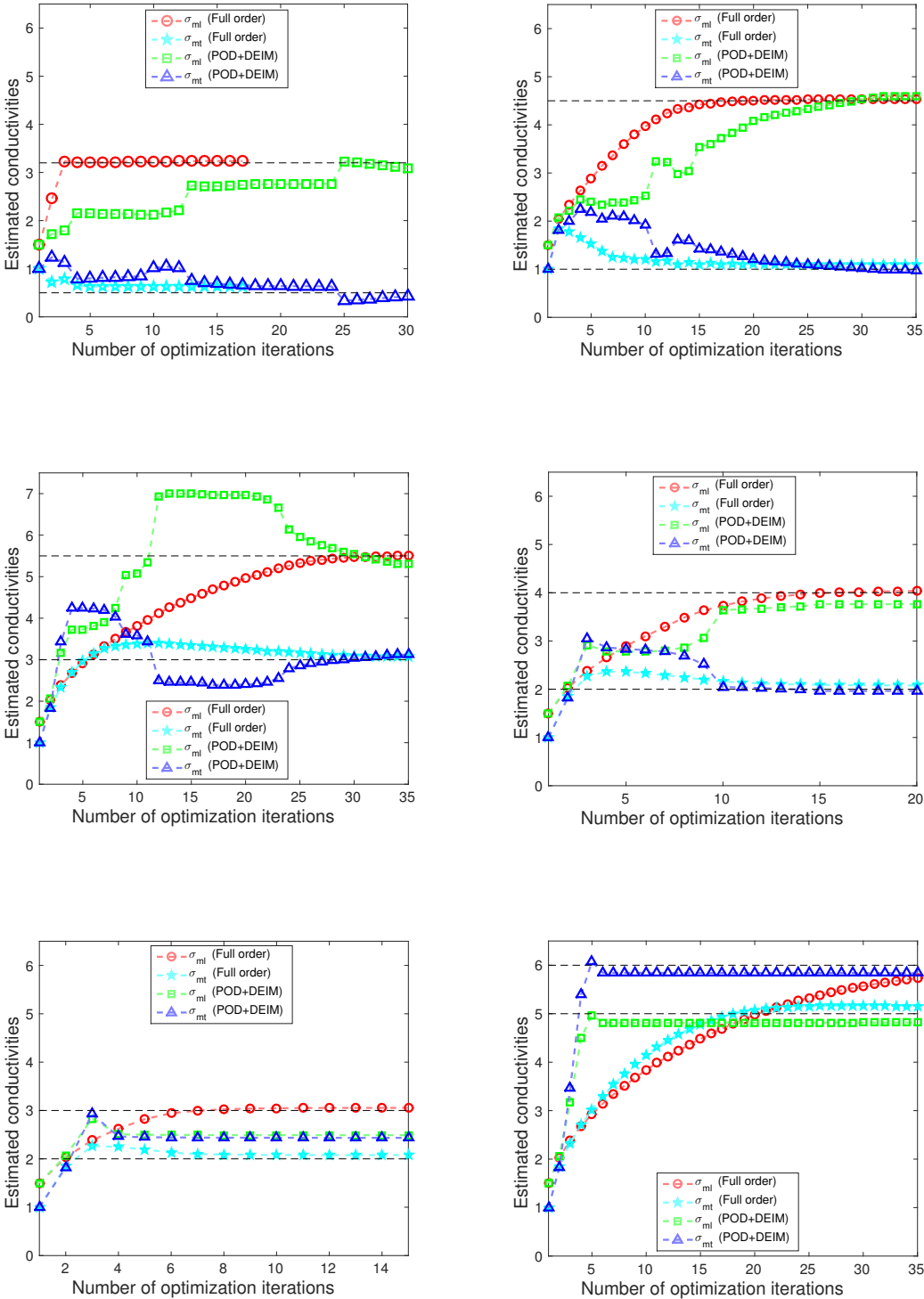
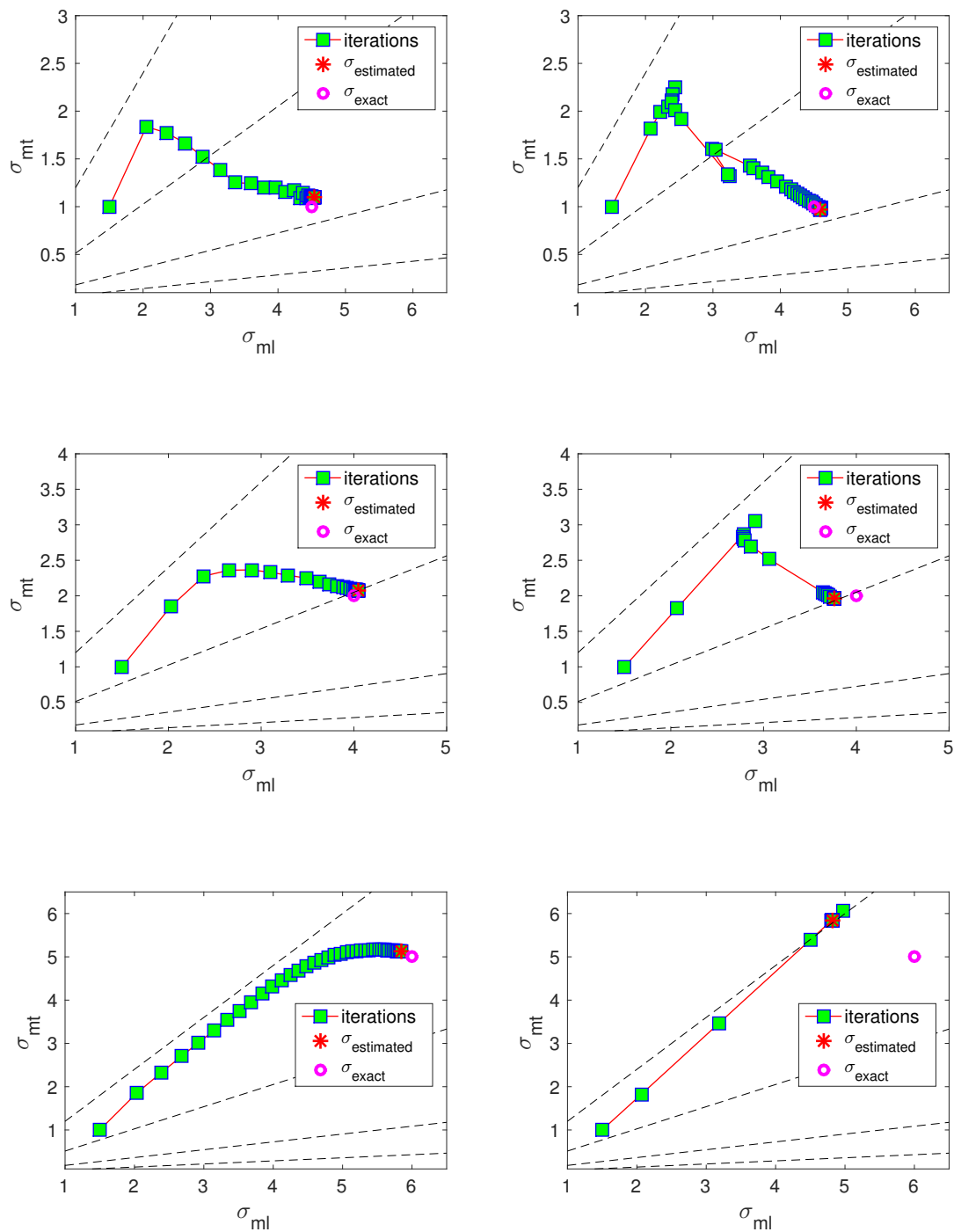**Figure 5.12:** Optimization iterations corresponds to Table 5.1

Figure 5.13: Optimization trajectory corresponds to Table 5.1 for test points: [4.5, 1], [4, 2], [6, 5]. The left column corresponds to the full-order inverse solver, while the right column corresponds to the reduced inverse solver.
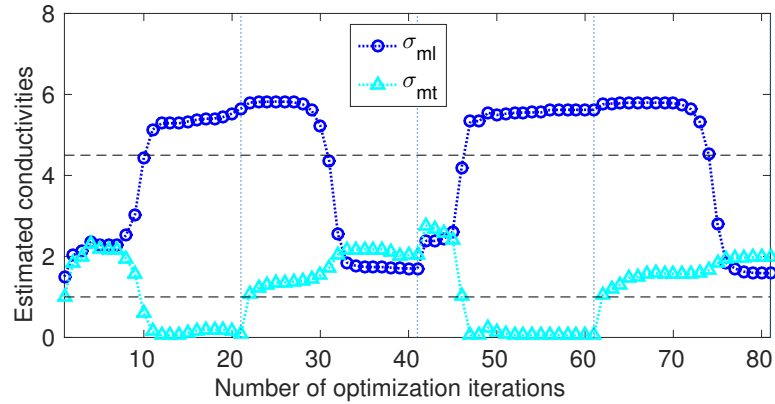
Figure 5.14: Optimization iterations by adaptive POD oscillate around the exact conductivity $\boldsymbol{\sigma}_{\text{exact}} = [4.5, 1]$ highlighted by the dash lines. Each optimization cycle is constrained by a maximum iteration number 20.

slightly worse estimates than the full-order inverse solver, due to the lose of accuracy of the ROM. However, the total execution time can be reduced by at least 90% and the estimation results using ROM are very satisfying with all the test points except for the last two, whose accuracies are weak on the conductivity ratio but fine on the magnitude. These two weak estimations can be easily improved by adding extra one or two sample points near the boundary of the admissible domain $\frac{\sigma_{\text{ml}}}{\sigma_{\text{mt}}} = 1$. Another impression the results convey is: even with the 24272-node mesh, which features somewhat obvious difference between the potential computed with the exact finite element approximation on nonlinearity and the potential solved by pointwise evaluation on nonlinearity, the conductivity estimations using ROM are still promising.

The iteration histories corresponding to the 76832-node case are plotted in Fig. 5.12. Some of them are also shown in the plane as displayed in Fig. 5.13. We can see that the optimal pathway in the reduced inverse solver is very similar to that in the full-order inverse solver. Since adaptive POD is a hot topic in the literature, here we test the practicability of adaptation by an online procedure. We generated the potential measures with $\sigma_{\text{exact}} = [4.5, 1]$. Given initial guess $\boldsymbol{\sigma}_{\text{initial}} = [1.5, 1]$, we solved the full-order monodomain system, extracted the snapshots of u and I_{ion} for POD basis construction online, solved the reduced inverse solver with the current unique basis, took the estimated con-

ductivities to run a full-order simulation, built a new POD basis and solved the reduced inverse solver again with the new basis and with previous estimate as the initial guess. These steps were circulated until a stop criterion was fulfilled. In the test, we setted a maximum iteration number 20 in each reduced inverse solving. The first four cycles of the iterations are reported in Fig. 5.14. As we expected, the optimization iterations intensively oscillate around the exact conductivity value. This is caused by the "self-contradictory" feature of the reduced monodomain model: we are forced to use a RB constructed with a unique generating parameter, but the domain of effectiveness of this kind of RB is generally very narrow. In conclusion, a simple use of POD adaptation for inverse conductivity problem is not feasible in practice. This concept needs to be further explored, customized, and refined in depth.

5.6   Chapter conclusions

We have presented some failure and success facts in solving the reduced monodomain inverse conductivity problem with the POD-DEIM approach. The monodomain solution features some exceptional properties, not existing in classical problems, that cause difficulties in reduced-order modeling.

The main challenge of model reduction lies in the POD basis construction. We have observed that the domain of effectiveness (DOE) of a POD basis based on a single generating parameter is kind of narrow, especially when the amplitude of the conductivity value is small. This phenomena has also been shown in a recent study on POD application for ionic model parameter estimation [17]. The situation in our case is even worse, considering the fact that we can not group snapshots for basis construction from different generating parameters, due to the strong sensitivity of the transmembrane potential to the conductivities. In other words, a unique POD basis is inadequate for the inverse conductivity problem, where the simulations are performed with various conductivity parameters. This is confirmed by a numerical test of adaptive POD, which returns intensive oscillation around the exact values.

Another challenge that deserves mention is the failure of adding sensitivity snapshots, which is expected to highly improve the effectiveness of the POD basis in classical problems [27]. We find that putting extra sensitivity snapshots into the snapshot matrix of state variables doesn't enlarge the DOE of the constructed RB as much as we desire. Even if it did to some extent, the required number of POD modes is almost tripled, hence it is not appropriate for online application.

Nevertheless, there are still some interesting observations that finally lead to a success. We detect that the domain of effectiveness of a reduced basis is confined to an angular region of its generating parameter, and the region would be enlarged if we expand the parameter amplitude. Based on this, we sample the parameter space utilizing the polar coordinates and the Gauss–Lobatto nodes. A sample set of size ten is then obtained. The usage of multiple POD bases, each generated with a sampled parameter, provides satisfactory results. Overall, by utilizing this POD-DEIM reduced order model, the computational effort can be reduced by at least 90% in conductivity estimation.

We do not claim that we have thoroughly solved all the difficulties in this chapter. Alternative sampling strategies such as an adaptive sampling in particular for the current problem should be investigated in future works. To our best knowledge, this is not an easy work, because a heuristic observation on reduced basis adaptation online returns unstable results.

Chapter 6

Reduced-order modeling for atrial electrophysiology by a data-driven approach

This development of a data-driven model reduction technique for electrocardiology is a project during the summer internship in 2014 at Siemens Corporate Research, Princeton, NJ. The work was supervised by Tiziano Passerini and Tommaso Mansi and led to the publication [138].

6.1   Introduction

Computational modeling of healthy and diseased *atrial* electrophysiology (EP) has a great potential for use in clinical practice. It can provide non-invasive, cost effective and personalized assessment of the state of the heart; furthermore, it can support the planning and guidance of cardiac therapies (such as the ablation therapy for atrial fibrillation) by predicting the response of the patient. To make them suitable for use in the clinic, EP models ought to be 1) computationally efficient, 2) reliable in capturing detailed cardiac biology, and 3) easy to be personalized, directly or statistically, from clinical data.

Recent EP models are capable of describing more and more complex cellular mechanisms, such as detailed intracellular Ca^{2+} handling and the functioning of ion channels, which are crucial for the detailed description of the organ electrical activity. However, these models are computationally demanding due to the many and coupled algebraic and ordinary differential equations accounting for different ionic channels and gating variables. As an example, the CRN human atrial cell model [36] introduced in Sec. 2.2.1 features 35 static parameters and 21 ordinary differential equations to describe 12 ionic channels, the corresponding gating variables and ionic concentrations (see the ionic channel diagram in Figure 2.8). Another challenge is the availability of robust and efficient methods to personalize EP models, especially ones featuring a large number of parameters. Several simplified or phenomenological models could be used as computationally efficient surrogates, such as the FitzHugh-Nagumo (FHN) model [47] which came before the CRN model chronologically. However, these models usually lack the capability of describing important physiological properties. Moreover, to the best of our knowledge no simplified model similar to the minimal one for ventricular dynamics is currently available for human atria-specific cellular EP.

The topic of reduced-order modeling for cardiac electrophysiology in particular has been explored in the literature. Most relevant to this work, an approach based on proper orthogonal decomposition and the Galerkin method has been proposed in [18] and also in Chapter 5.

Model reduction techniques relying on statistical learning (often referred to as meta-modeling) have been used in particular in the chemometrics community. The idea is to derive a statistical model that is able to predict the output of a nonlinear computational model which has complex dynamics, while being expressed with fewer parameters and being extremely computationally efficient [128]. Recently, Sobie [123] used a *Partial Least Squares Regression* (PLSR) model for the sensitivity analysis of ventricular cell models on the model parameters. The statistical model proved is able to regress with excellent accuracy some action potential quantities such as *action potential duration* (APD). Mansi

et al. [81] also used a data-driven approach with manifold learning techniques to predict the sarcomere force exerted by a cardiac myofilament model.

Motivated by recent progresses in meta-modeling [81], we apply a data-driven approach to the reduction of state-of-the-art cellular models used for atria simulation in literature. The reduced model learned by regression keeps the ability to capture the complex dynamics of the original biophysically detailed model, while in simple form and depending on a smaller number of parameters. This makes the model efficient and suitable for use for large scale simulations at the organ level. To the best of our knowledge, this represents the first example of application of a model reduction technique based on statistical learning to the multiscale modeling of cardiac EP. In this work, we focus on the CRN atrial cell model. We first use the Principal Component Analysis (PCA) to reduce the dimensionality of the AP manifold (Sec. 6.2.1). We then learn a regression model of AP dynamics at the cell level, given a set of CRN model parameters (Sec. 6.2.2). Finally we use this reduced cellular model for tissue-level EP modeling (Sec. 6.2.3).

As reported in Sec. 6.3, AP manifold dimension can be reduced to 15 despite being the output of a nonlinear system. Our regression model demonstrates the ability of capturing the physiological complexity of cardiac AP. It drastically improves the performance of atrial tissue-level EP modeling by achieving a 75% reduction of the computational cost with the same computational time step and two order of magnitudes less computational time with larger time steps (in the order of seconds to compute one heart cycle of electrical activation in a patient-specific atrial anatomy, using a regular workstation).

6.2   Methods

Although the methods described in the following do not depend on the specific choice of the cellular model, we focus here on the CRN cell model, a model suitable for the description of atrial electrophysiology. The CRN cell model was developed based on human atrial cell data and has been validated for use in both tissue [7] and organ [5] level simulations. The model was introduced in Sec. 2.2.1, and its dominating equation

is restated here as

$$\frac{du}{dt} = -\frac{I_{\text{ion}} + I_{\text{stim}}}{C_{\text{m}}}, \tag{6.1}$$

where I_{ion} is the total of 12 ionic currents.

For modeling electrophysiology at the tissue level, we resort to the monodomain model coupled with the CRN cell model. The monodomain equation has been reshaped as

$$\frac{\partial u}{\partial t} = \frac{1}{\beta C_{\text{m}}} \nabla \cdot (\boldsymbol{\sigma}_{\text{m}} \nabla u) - \frac{I_{\text{ion}} + I_{\text{stim}}}{C_{\text{m}}}, \tag{6.2}$$

where $I_{\text{stim}} = -\frac{1}{\beta} I_{\text{app}}$ as compared with the formulation in (2.16). While lacking the knowledge of proper conductivity values of $\boldsymbol{\sigma}_{\text{m}}$, we customize the value in a reasonable range for simulations in this Chapter.

6.2.1 AP manifold learning for dimensionality reduction

The solution of equation (6.1) is the time-dependent transmembrane action potential (AP) $u(t)$. We use manifold learning techniques to reduce the dimensionality of the manifold Ω_{AP} to which $u(t)$ belongs. Namely, we analyze the number of intrinsic parameters q that is necessary to capture the observed AP data. Let n be the number of observations. For each observation i, we choose a unique set of model parameters $\boldsymbol{\theta}^i \in \mathbb{R}^{1 \times p}$ and compute the AP in m time snapshots. The results are gathered in the observation vector $\mathbf{u}^i = [u^i(t_1), \cdots, u^i(t_m)] \in \mathbb{R}^{1 \times m}$. The $n \times m$ observation matrix

$$\mathbf{Y} = \begin{bmatrix} \mathbf{u}^1 \\ \mathbf{u}^2 \\ \vdots \\ \mathbf{u}^n \end{bmatrix} = \begin{bmatrix} u^1(t_1) & u^1(t_2) & \cdots & u^1(t_m) \\ u^2(t_1) & u^2(t_2) & \cdots & u^2(t_m) \\ \vdots & \vdots & \vdots & \vdots \\ u^n(t_1) & u^n(t_2) & \cdots & u^n(t_m) \end{bmatrix}$$

represents a sampling of the AP manifold. Before dimension reduction, values in the AP matrix $\mathbf{Y}$ are converted into z-scores — each column is mean-centered and normalized by its standard deviation [70]. After this pre-processing, we denote the AP matrix by $\mathbf{Y}_{\text{zs}}$. To

uncover the intrinsic structure of the AP manifold, both the Principal Component Analysis (PCA) [52] and the *Locally Linear Embedding* (LLE) [118] manifold learning techniques are tested.

The PCA has been introduced at the end of Sec. 5.3.1, we may use here different notations for concepts already introduced in a different context. The PCA projects the high-dimensional space Ω_{AP} onto the reduced space $\Omega_{\mathrm{AP}}^{\mathrm{pca}}$ formed by principal components $\mathbf{w}_l \in \mathbb{R}^{m \times 1}$ ($l \in \{1, \cdots, q\}$) that are orthogonal (uncorrelated) and maximize the observed covariance. The principal components $\mathbf{w}_l$'s are given by the eigenvectors of the covariance matrix $\mathbf{Y}_{\mathrm{zs}}^T \mathbf{Y}_{\mathrm{zs}} \in \mathbb{R}^{m \times m}$ in the decreasing order of corresponding eigenvalues. The transformation from an observation $\mathbf{z} \in \mathbb{R}^{1 \times m}$ in Ω_{AP} to a new vector $\mathbf{u}_{\mathrm{pca}} \in \mathbb{R}^{1 \times q}$ of principal component scores in $\Omega_{\mathrm{AP}}^{\mathrm{pca}}$ is

$$\mathbf{u}_{\mathrm{pca}} = \mathbf{z}\mathbf{W}$$

where $\mathbf{W} = [\mathbf{w}_1, \cdots, \mathbf{w}_q] \in \mathbb{R}^{m \times q}$. Given an observation by the PCA coefficient vector $\widehat{\mathbf{u}}_{\mathrm{pca}} \in \mathbb{R}^{1 \times q}$, the reconstruction from space $\Omega_{\mathrm{AP}}^{\mathrm{pca}}$ to space Ω_{AP} is by

$$\widehat{\mathbf{u}} = \bar{\mathbf{y}} + (\widehat{\mathbf{u}}_{\mathrm{pca}}\mathbf{W}^T) \circ \boldsymbol{\sigma}_Y.$$

Here $\bar{\mathbf{y}}$ and $\boldsymbol{\sigma}_Y$ are vectors containing the means and standard deviations of observations in $\mathbf{Y}$, and $\circ$ means element-wise product.

The LLE seeks a projection of data onto a low-dimensional space $\Omega_{\mathrm{AP}}^{\mathrm{lle}}$ by a neighbourhood preserving mapping. It can be thought of as a process of local PCA which are globally compared to capture the best nonlinear structure. The standard LLE algorithm is in three steps:

1. search the k (user defined) nearest neighbours of each data point $\mathbf{z}^i$, denote the neighbour indices as $\{n_1, \cdots, n_k\}$;

2. compute the barycentric coordinates $\{w_{ij}\}_{j=1}^k$ that best reconstruct each data point $\mathbf{z}^i$ from its neighbours;

Table 6.1: Parameters in the CRN model

Parameter	Definition	Baseline value
g_{Na}	Maximal fast inward Na$^+$ current (I_{Na}) conductance	7.8 nS/pF
g_{K1}	Maximal inward rectifier K$^+$ current (I_{K1}) conductance	0.09 nS/pF
g_{to}	Maximal transient outward K$^+$ current (I_{to}) conductance	0.1652 nS/pF
g_{Kr}	Maximal rapid delayed rectifier K$^+$ current (I_{Kr}) conductance	0.0294 nS/pF
g_{Ks}	Maximal slow delayed rectifier K$^+$ current (I_{Ks}) conductance	0.129 nS/pF
$g_{\mathrm{Ca,L}}$	Maximal L-type inward Ca^{2+} current ($I_{\mathrm{Ca,L}}$) conductance	0.1238 nS/pF
$g_{\mathrm{b,Ca}}$	Maximal background Ca^{2+} current ($I_{\mathrm{b,Ca}}$) conductance	0.00113 nS/pF
$g_{\mathrm{b,Na}}$	Maximal background Na$^+$ current ($I_{\mathrm{b,Na}}$) conductance	0.000674 nS/pF
$I_{\mathrm{NaK(max)}}$	Maximal Na$^+$ $-$ K$^+$ pump current (I_{NaK})	0.60 pA/pF
$I_{\mathrm{NaCa(max)}}$	Maximal Na$^+$/Ca^{2+} exchanger current (I_{NaCa})	1600 pA/pF
$I_{\mathrm{p,Ca(max)}}$	Maximal sarcoplasmic Ca^{2+} pump current ($I_{\mathrm{p,Ca}}$)	0.275 pA/pF
$g_{\mathrm{Kur(max)}}$	Scale factor of ultrarapid delayed rectifier K$^+$ current (I_{Kur})	1

3. compute the embedding coordinates vector $\mathbf{u}_{\mathrm{lle}}^i \in \mathbb{R}^{1 \times q}$ of $\mathbf{z}^i$ in $\Omega_{\mathrm{AP}}^{\mathrm{lle}}$ with fixed weights w_{ij} by minimizing the embedding cost function

$$\Phi(\mathbf{U}_{\mathrm{emb}}) = \sum_{i=1}^{n} |\mathbf{u}_{\mathrm{lle}}^i - \sum_{j=1}^{k} w_{ij}\mathbf{u}_{\mathrm{lle}}^{n_j}|^2$$

where $\mathbf{U}_{\mathrm{emb}} = [\mathbf{u}_{\mathrm{lle}}^1, \cdots, \mathbf{u}_{\mathrm{lle}}^n]$.

Given an observation by the LLE coefficient vector $\widehat{\mathbf{u}}_{\mathrm{lle}}$, the reconstruction from space $\Omega_{\mathrm{AP}}^{\mathrm{lle}}$ to space Ω_{AP} starts from finding its k nearest neighbours within space $\Omega_{\mathrm{AP}}^{\mathrm{lle}}$ and then follows a similar way as above.

6.2.2 Regression model

We then learn a regression model of action potential dynamics given a sample space of the CRN model parameters $\boldsymbol{\theta} \in \mathbb{R}^{1 \times p}$ and their corresponding AP outputs $\mathbf{u} \in \mathbb{R}^{1 \times m}$.

Model Input. The CRN model parameters $\boldsymbol{\theta}$ are used as the regression inputs.

Model Output. Instead of the time-series of action potential $u(t)$, we consider the reduced AP representation computed in Section 6.2.1 as output: the regression model predicts the q embedding coordinates $\mathbf{u}_{\mathrm{emb}}$ (either $\mathbf{u}_{\mathrm{pca}}$ or $\mathbf{u}_{\mathrm{lle}}$), which are then used to reconstruct the AP time frames $\mathbf{u}$ with the basis provided by PCA or LLE.

Model Construction. The data-driven model writes

$$\mathbf{u}_{\mathrm{emb}} = \mathbf{f}(\boldsymbol{\theta}), \ \mathbf{f} : \mathbb{R}^p \to \mathbb{R}^q.$$

Rather than directly regressing $\mathbf{u}_{\mathrm{emb}}$ from $\boldsymbol{\theta}$, we propose a two-step model construction process based on statistical learning. We first regress some phenomenological features of the AP, and then use them as additional inputs for the second regression step to increase the accuracy of the overall prediction. The rationale behind this choice is that many phenomenological features of AP can be regressed with high accuracy from $\boldsymbol{\theta}$, as shown in Sec. 6.3, and adding them as features helps further constraining the second regression problem.

More precisely, we characterize the action potential by different properties: peak voltage (V_{peak}), resting membrane potential (V_{rest}), action potential duration (APD). We learn a prediction model for these quantities

$$\mathbf{f}_1 : \boldsymbol{\theta} \mapsto [V_{\mathrm{peak}}, V_{\mathrm{rest}}, APD]$$

using the projection pursuit regression (PPR) method [53]. The central idea of PPR is to extract optimal linear combinations of inputs as derived features, the outputs are then modelled as a nonlinear function of these features. The model for each component (say f_1) of $\mathbf{f}_1$ has the form

$$f_1(\boldsymbol{\theta}) = \sum_{j=1}^{s} g_j(\boldsymbol{\theta}\boldsymbol{\omega}_j),$$

where the projection direction $\boldsymbol{\omega}_j$ is a unit vector in $\mathbb{R}^{p \times 1}$, the function $g_j(\cdot)$ is unspecified and estimated using a flexible smoothing method. The model is built in an iterative manner: given projection direction $\boldsymbol{\omega}$ (consider $s = 1$ for instance and omit the subscript), apply a univariate smoother to obtain an estimation of g; given function g, use Gauss-Newton search to minimize the fitting error function over test directions and then obtain an optimal direction $\boldsymbol{\omega}$. The number of ridge terms s is determined by a backward

deletion procedure. In this work, we use the R function ppr[1], where R is a free software environment for statistical computing.

The second step of the full statistical learning procedure is to regress the embedding coordinates $\mathbf{u}_{\mathrm{emb}}$ by including predicted values of those AP quantities as inputs together with the CRN model parameters $\boldsymbol{\theta}$. This step estimates a model

$$\mathbf{f}_2 : [\boldsymbol{\theta}, \mathbf{f}_1(\boldsymbol{\theta})] \mapsto \mathbf{u}_{\mathrm{emb}}$$

using either the multivariate adaptive regression spline (MARS [52]) or the PPR method as in the first step. MARS is a non-parametric regression method extending linear regression by fitting linear or cubic splines to capture data nonlinearity. The model for each component (say f_2) of $\mathbf{f}_2$ has additive form as

$$f_2(\boldsymbol{\theta}, \mathbf{f}_1(\boldsymbol{\theta})) = \beta_0 + \sum_{j=1}^{J} \beta_j h_j(\boldsymbol{\theta}, \mathbf{f}_1(\boldsymbol{\theta})),$$

where $h_j(x)$ is a function of the form $\max(x - c, 0)$ or $\max(c - x, 0)$ or their products with c being a constant. The model is built by a greedy approach fitting the splines to the training data, and then a backward deletion pass on splines to minimize over-fitting. We use the R package earth [84] for MARS model construction. A possible modification of this step is to iteratively use the components of $\mathbf{u}_{\mathrm{emb}}$ as inputs. To be specific, we use $[\boldsymbol{\theta}, \mathbf{f}_1(\boldsymbol{\theta})]$ and also $\mathbf{u}_{\mathrm{emb}}(1)$ to regress $\mathbf{u}_{\mathrm{emb}}(2)$, and similarly for the following components of $\mathbf{u}_{\mathrm{emb}}$.

AP Prediction. Given a new set of parameters $\widehat{\boldsymbol{\theta}}$, the AP prediction is as follows

$$\widehat{\boldsymbol{\theta}} \to \widehat{\mathbf{u}}_{\mathrm{emb}} = \mathbf{f}_2(\hat{\boldsymbol{\theta}}, \mathbf{f}_1(\widehat{\boldsymbol{\theta}})) \to \widehat{\mathbf{u}} \text{ reconstruction from } \widehat{\mathbf{u}}_{\mathrm{emb}}.$$

---

[1] https://stat.ethz.ch/R-manual/R-devel/library/stats/html/ppr.html

6.2.3   Application to tissue-level atrial EP modeling

We present a framework for efficient patient-specific simulation of cardiac transmembrane potential. We process medical images for computational domain preparation, use the reduced regression model constructed in Sec. 6.2.2 for cellular AP simulation and the lattice-Boltzmann algorithm for AP propagation. Details of EP modeling on the atria as an example is described in the following.

Computational domain preparation from medical images

Starting from atria images (e.g. from CT), the left and right atrium are automatically segmented using a machine learning approach [142]. Regional atrial wall thickness can be extracted from high resolution images, but this may be challenging to obtain for the whole atria. We follow a simpler approach, applying a uniform mesh thickening based on thresholding a level-set representation of the atrial surface on an isotropic Cartesian grid. Grid nodes lying at the sino-atrial node region are manually annotated. If available, information on the fiber orientation can be readily included in the computational domain, as described in [141] for the case of ventricular tissue. In this work we do not model the presence of fibers in the atrial tissue. Since tissue anisotropy plays a role in the monodomain equation, but not in the cell model, the proposed model reduction strategy is not affected by this choice.

Lattice-Boltzmann method for cardiac EP

We solve the monodomain equation on a Cartesian grid by applying the lattice-Boltzmann method introduced in [111]. In the lattice-Boltzmann approach, the potential u is represented in terms of the probability $f_i(\boldsymbol{x}, t)$ of finding a particle at location $(\boldsymbol{x}, t)$ moving with velocity $\boldsymbol{e}_i$. The transmembrane potential is approximated by the f_i's through

$$u(\boldsymbol{x}, t) = \sum_i f_i(\boldsymbol{x}, t).$$

We use a 7-connectivity topology (6 connections + central position). The directions of the velocities $\boldsymbol{e}_i$ are related to the links connecting every lattice node to its 6 nearest neighbours on the Cartesian grid, as well as a link to itself.

The *lattice Boltzmann equation* (LBE) derived for the monodomain model by Rapaka et al. in [111] is solved by two successive steps:

$$\mathbf{f}^* = \mathbf{f}(\boldsymbol{x}, t) - \mathbf{A}(\mathbf{f} - u(\boldsymbol{x}, t)\boldsymbol{\omega}) - \Delta t \tfrac{I_{\text{ion}} + I_{\text{stim}}}{C_{\text{m}}}(\boldsymbol{x}, t)\boldsymbol{\omega} \tag{6.3}$$

$$\mathbf{f}(\boldsymbol{x} + \boldsymbol{e}_i \Delta x, t + \Delta t) = \mathbf{f}^* \tag{6.4}$$

where $\mathbf{f}(\boldsymbol{x} + \boldsymbol{e}_i \Delta x, t + \Delta t)$ is the column vector having components $f_i(\boldsymbol{x} + \boldsymbol{e}_i \Delta x, t + \Delta t)$, and Δx and Δt are the the grid interval and the time step, respectively. Here, $\boldsymbol{\omega} = [\omega_1, \omega_2, \cdots, \omega_7]^T$ is the vector of weight coefficients and $\omega_i = 1/7$ is chosen. Equation (6.3) gives a strictly local collision rule in which $\mathbf{f}^*$ is a post-collision state of the vector of distribution functions. The collision matrix $\mathbf{A}$ relaxes the distribution function f_i towards the local equilibrium value of the potential u, and is given by the *multiple-relaxation-time* (MRT) model $\mathbf{A} = \mathbf{M}^{-1}\mathbf{S}\mathbf{M}$, where $\mathbf{M}$ and $\mathbf{S}$ are detailed in [111] and [140]. After collision, the distribution functions stream along their corresponding directions to the neighbouring node (eq. 6.4).

The Neumann boundary condition on a surface of complex geometries can be handled by means of a level-set formulation without the need of advanced meshing algorithms. For details on the Lattice-Boltzmann algorithm, we refer to [111]. The ionic current term I_{ion} in the equation (6.3) is registered (see below) from the designed regression model.

Registration of the regression cellular model

The CRN cellular model was designed by setting I_{ion} as a sum of analytical functions of u and controlling the time evolution of u using equation (6.1). The parameters inside the model are then adjusted by fitting experimental data (action potentials) measured in isolated atrial myocites [36]. The regression model we designed is discrete. We describe its registration in tissue-level modeling as the following steps.

1. Given a set of model parameters, the regression model predicts the full time sequence $\mathbf{u}_{\mathrm{ref}}$ of AP, in m time snapshots (as for the observations in the training data set). To obtain the potential value at each time in the heart cycle, we align $\mathbf{u}_{\mathrm{ref}}$ at the time t_{upstroke} of AP upstroke or depolarization; then we extract the proper snapshot from $\mathbf{u}_{\mathrm{ref}}$.

2. To monitor t_{upstroke} in each cell, we propose to use the simple Mitchell–Schaeffer (MS) model [88] (having only one gating variable). For the sake of clarity, we assume that the time step Δt used by the monodomain solver is a multiple of the time step used to sample $\mathbf{u}_{\mathrm{ref}}$.

3. After the upstroke, at time $t^i = t_{\mathrm{upstroke}} + i\Delta t$, the term involving ionic current in equation (6.3) is computed as follows

$$-\frac{I_{\mathrm{ion}} + I_{\mathrm{stim}}}{C_{\mathrm{m}}}(\boldsymbol{x}, t^i) = \frac{\mathbf{u}_{\mathrm{ref}}(i) - u(\boldsymbol{x}, t^{i-1})}{\Delta t}\ ,$$

   with $i \in \mathbb{N}$ corresponding to the selected time snapshot of $\mathbf{u}_{\mathrm{ref}}$. Notice that this discrete from is still fitted by single cellular AP in which case $u(\boldsymbol{x}, t^{i-1})$ should be $\mathbf{u}_{\mathrm{ref}}(i-1)$, and it is consistent with the backward Euler discretization of equation (6.1) which describes the original CRN cellular model.

4. After AP repolarization, we switch to use the MS model to monitor the next heart beat.

   To find more sophisticated ways for monitoring AP upstroke is a subject of future work.

6.3   Experiments and results

6.3.1   Model parameter selection and sampling

We considered as model input a set of 12 parameters listed in Table 6.1 with each controlling an ionic channel in the CRN model. The chosen parameters represent maximal
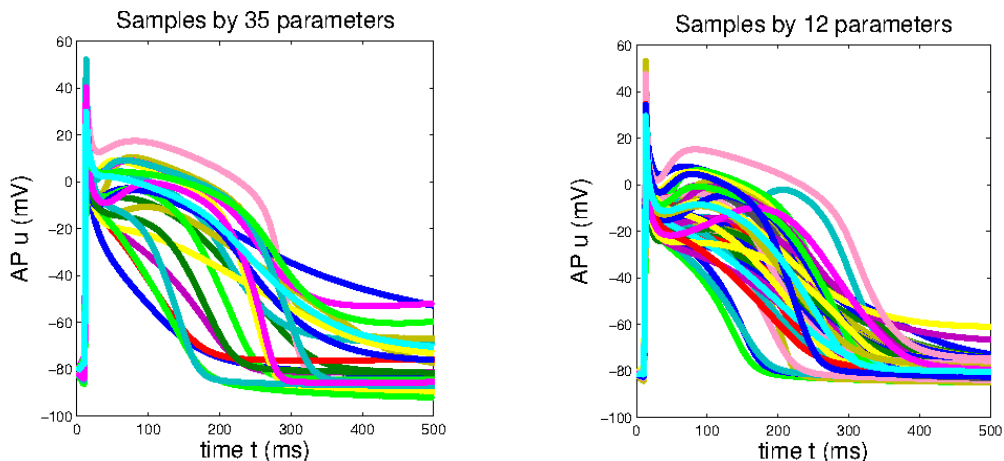
Figure 6.1: Samples with SD=0.3 by different number of parameters

ionic conductances and maximal channel currents. A sample was generated by scaling the baseline values listed in [36], and scaling factors were chosen randomly from a log-normal distribution with mean value 1 and standard deviation 0.3. It is worth mentioning that using these 12 parameters rather than the entire set of 35 parameters in the original model can still capture a large variety of AP patterns. As shown in Figure 6.1, the variety of samples generated by these 12 parameters is comparable with that of the 35-parameter samples. In other words, it's unnecessary to use the full set of parameters to explore the Ω_{AP} manifold, while taking a larger number of parameters may reduce the regression accuracy and make the model personalization less efficient.

Different samples can be obtained with alternative choices of the parameters to be used as model input. For instance, the parameters selection could be guided by a sensitivity analysis of relevant features of the cell model (e.g., the APD). This would allow the definition of different samples for different applications. In an extreme example such as the study of atrial fibrillation, characterized by a significantly shortened APD, a specialized sample could be constructed by perturbing the parameters after proper adjustment of the reference values, as shown in [72].

For the generation of the database, an electrical stimulus was applied with amplitude -20 pA/pF starting at $t = 10$ ms and lasting for 1 ms. In the first 500 ms, $u(t)$

was recorded in 1000 time snapshots. In our first experiment, the training set consisted
of 1000 observations and the testing set consisted of 500 different observations. The
goodness of fit of the predicted output is measured in different ways (and always on the
original data before the dimension reduction or the conversion into z-scores):

- R^2 *value* defined as

$$R^2 = 1 - \frac{SS_{\text{res}}}{SS_{\text{tot}}}$$

  with SS_{res} being the residual sum of squares and SS_{tot} being the total sum of
  squares,

- *Maximum Amplitude Difference* (MAD, in mV) defined by

$$MAD(y_i, y_j) = |\max(y_i(t)) - \max(y_j(t))|,$$

- absolute differences between *Areas Under the Curves* (AUC).

The resting potential V_{rest} is defined as the potential recorded at the end of the simulation,
i.e at $t = 500$ ms. The action potential duration APD_{20} (APD_{40}, APD_{60}) is defined as
the time from AP onset ($\arg_t \max \frac{du}{dt}$) to the -20 mV (-40 mV, -60 mV) repolarization
moment. For the training dataset in this experiment, the $MAD, V_{\text{rest}}, APD_{60}$ variations
in mean $\pm$ SD form were 29.2772 $\pm$ 8.43309 mV, -77.4807 $\pm$ 5.61862 mV, and 269.346
$\pm$ 67.45435 ms respectively.

6.3.2   PCA versus LLE for manifold learning

The reduced spaces $\Omega_{\text{AP}}^{\text{pca}}$ and $\Omega_{\text{AP}}^{\text{lle}}$ were constructed from the training set. We find that
the PCA and LLE dimension reduction techniques perform similarly on the AP manifold
Ω_{AP}, despite the fact that LLE can capture nonlinear manifold structures. To investigate
this, we compare the accuracy of reconstruction by plotting the maximum relative error
(relative to the mean value of training data) of APD_{60} in the left of Figure 6.2, and the
maximum R^2 value in the right. Each red vertical line in the right denotes the minimum
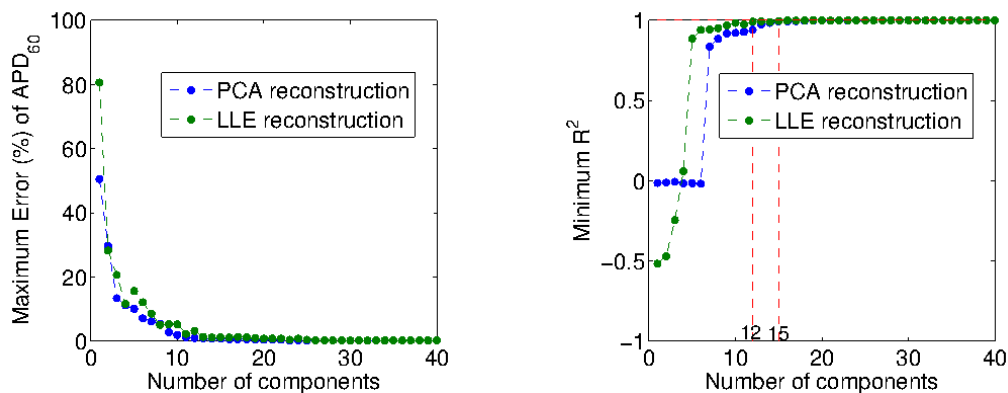
Figure 6.2: Goodness of reconstruction on testing data using PCA and LLE.

number of components needed for $R^2 > 0.99$ in reconstructing the AP in our training data. For LLE, the number of neighbors k is chose as $\max(20, n_{\mathrm{comp}})$ with n_{comp} being the number of components. An optimal number of neighbors can be chosen through benchmarking and the goodness of reconstruction will be improved, but the overall performance versus the number of components is almost the same. We see that both PCA and LLE need more that 10 components to accurately capture AP dynamics, but 15 components are sufficient (compared with the original 1000 time frames).

In consideration of the convenience of AP reconstruction, we will use PCA dimension reduction in subsequent experiments. Figure 6.3 illustrates the modes of AP variations estimated by PCA components. In particular, the first mode captures the AP amplitude, the following modes capture variations of curve curvatures in different phases of the heart beat.

6.3.3 Regression model construction

As mentioned in Sec. 6.2.2, we build a model by a two-step regression method. In the first step, three regression methods were tested to predict $[V_{\mathrm{peak}}, V_{\mathrm{rest}}, APD_{60}, APD_{40}, APD_{20}]$: PLSR, MARS, and PPR. To study the accuracy of PLSR, we set the number of components option in PLSR to be the number of model inputs p. In the earth function for MARS, we chose the maximum interaction degree as 2, and the maximum number
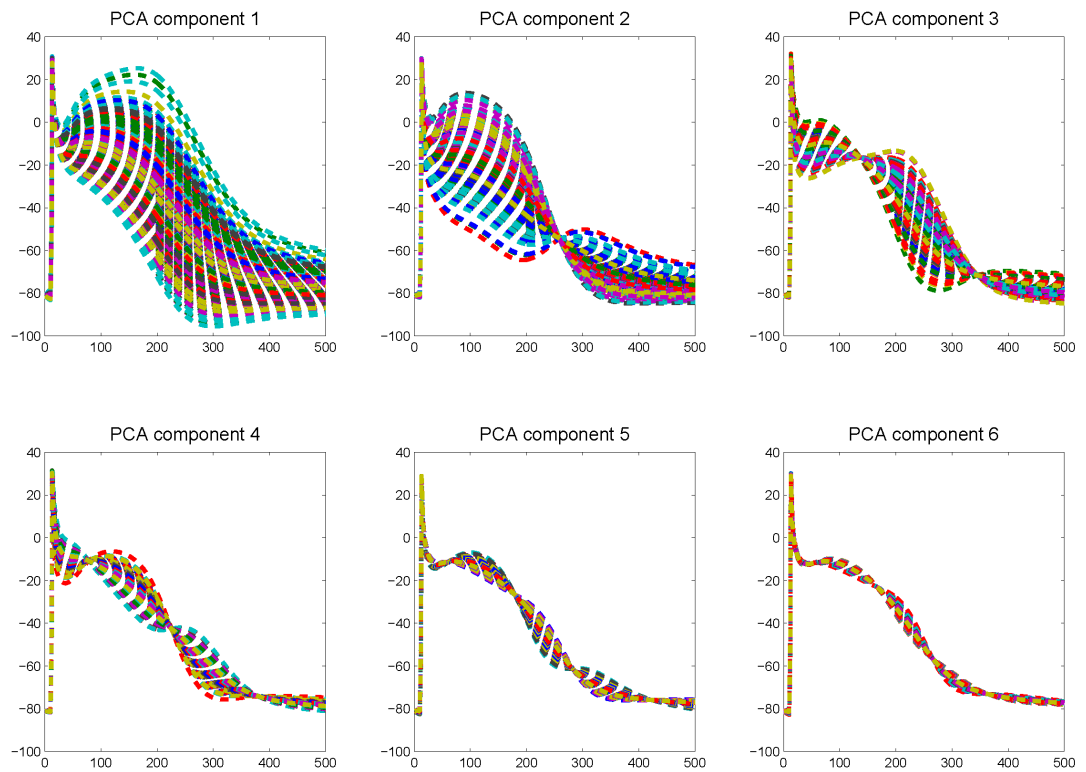
Figure 6.3: Dimensionality reduction of the AP manifold generated by the CRN model. The first six PCA modes are plotted.

of model terms as 80. In use of the ppr function for PPR, the number of terms in the model was set as 10, and the optimization level was set to re-balance the contributions from each regressor at each step. We report their R^2 values in Figure 6.4. We see that the most widely used method PLSR can accurately predict V_{peak}, but fails in regressing V_{rest}. This demonstrates the nonlinear complexity of the CRN atrial model, compared with sample variations of a ventricle model which can be easily predicted by PLSR with R^2 value 0.98 [123]. This results consists with the sample patterns in Figure 6.1 and the mode variations represented by PCA. We also find that MARS can accurately predict V_{peak} and V_{rest}, but returns worse results in APD prediction than PPR. Overall, PPR performs the best in this test, with all the R^2 values are above 0.97.

We also study the PPR model stability on the range of variation of the testing data. In Figure 6.5, the x-axis represents the standard deviation of testing data. We see that the R^2 values decrease as we increase SD, but for SD = 0.4, all R^2 values are still greater than 0.9. For SD=0.5, the predictor is much weaker. However, for the purpose of modeling patient specific EP, we believe that the range of variation of the model parameters obtained with a SD of 0.3 is large enough to reproduce the AP patterns of a large group of patients. Moreover, specific regression models can be designed for disease states characterized by altered AP patterns such as atrial fibrillation, when the APD is much shorter. This can be achieved e.g. by scaling adjusted values as in [72].

In the second step of model construction, we use extra parameters predicted from step one: $\mathbf{f}_1 = [V_{\text{peak}}, V_{\text{rest}}, APD_{60}, APD_{40}, APD_{20}]$. To predict $\mathbf{u}_{\text{emb}}$, i.e. the embedding coordinates in the 15-dimensional reduced space $\Omega_{\text{AP}}^{\text{pca}}$ of Ω_{AP}, for both MARS and PPR we tested four approaches:

($\mathcal{M}_1$)   use only $\boldsymbol{\theta}$ as model input;

($\mathcal{M}_2$)   use $[\boldsymbol{\theta}, \mathbf{f}_1]$ as model input;

($\mathcal{M}_3$)   use $\boldsymbol{\theta}$ as model input, and iteratively regress components of $\mathbf{u}_{\text{emb}}$, i.e. use $[\boldsymbol{\theta}, \mathbf{u}_{\text{emb}}(1), \cdots \mathbf{u}_{\text{emb}}(i)]$ as model input to predict $\mathbf{u}_{\text{emb}}(i+1)$;
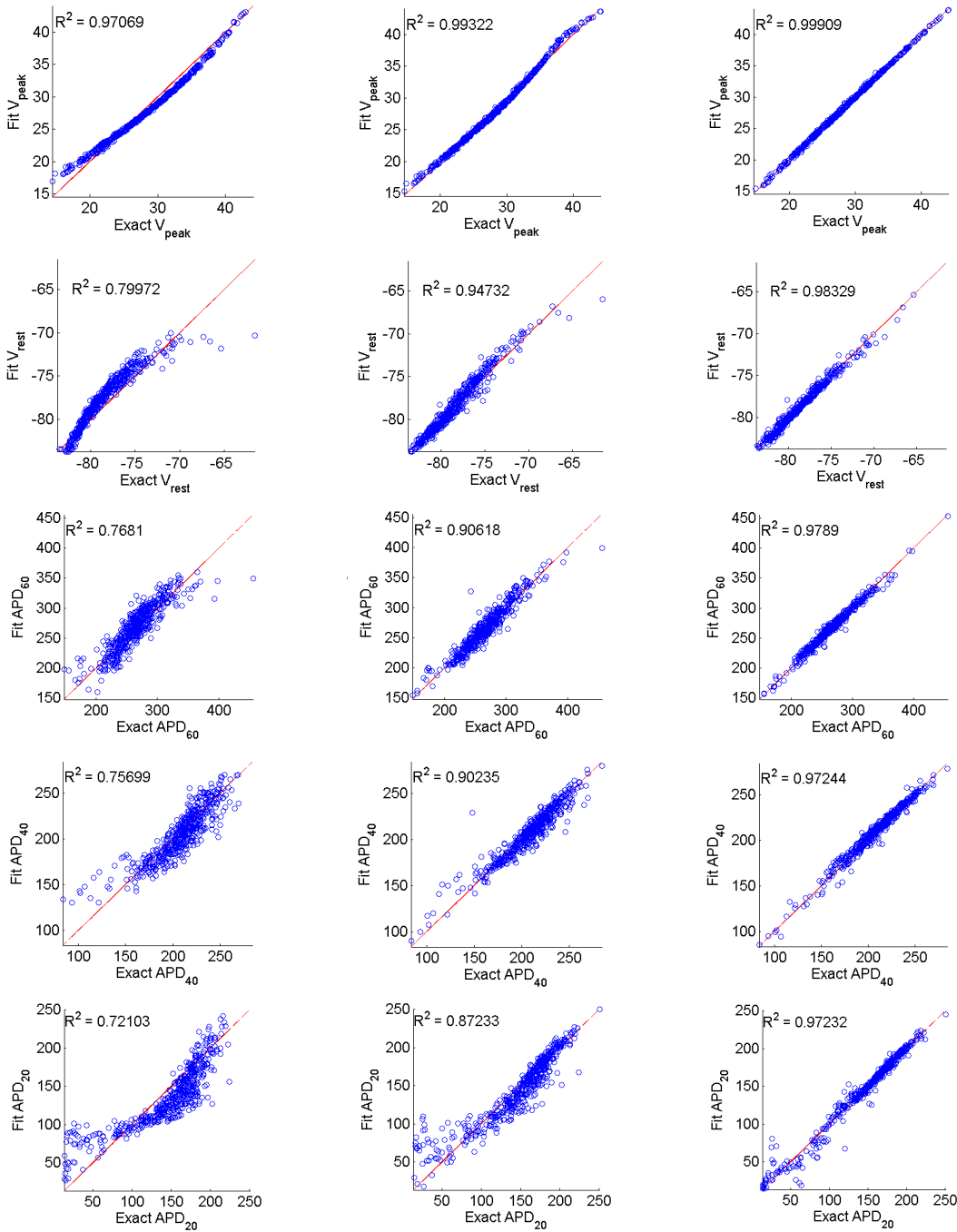
Figure 6.4: Regression on V_{peak}, V_{rest}, and APD by three methods: PLSR (column 1), MARS (column 2), PPR (column 3)
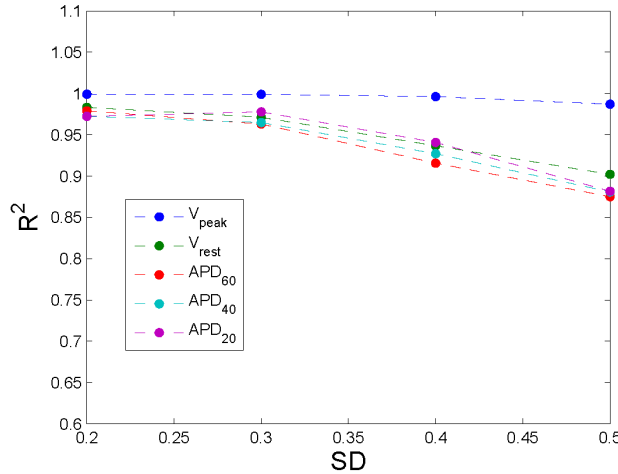
Figure 6.5: Model stability analysis on testing data variation range.

($\mathcal{M}_4$) use $[\boldsymbol{\theta}, \mathbf{f}_1]$ as model input, and iteratively regress components of $\mathbf{u}_{\mathrm{emb}}$.

We plot the MARS prediction in Figure 6.6 and the PPR prediction in Figure 6.7. Table 6.2 and 6.3 list the corresponding fitting errors by MARS and PPR predictions relative to mean values of the training data, respectively. The errors in MAD and V_{rest} measure the AP amplitudes, errors in APD measure the variation of curve curvatures (AP patterns), and AUC measures the errors in a global way.

As one can see, adding $\mathbf{f}_1$ as an extra parameter made the predicted AP curves have better APD fit and thus reduced the APD errors, while iteratively regressing the PCA components significantly decreased the MAD error. Overall, method $\mathcal{M}_4$ produced the best prediction. Both MARS and PPR predict the AP dynamics accurately, and PPR is accurate enough to be used without extra parameters. Compared with MARS, the regression accuracy is improved while using PPR. However, if we consider the regression model application in 3D EP modeling and EP model personalization, the regression model prediction speed impacts the personalization efficiency. In this scenario, MARS seems to be more promising based on our tests, as it is proved to be somewhat faster than PPR by the fact that PPR needs to store smoothing splines for each ridge function term in order to compute prediction.
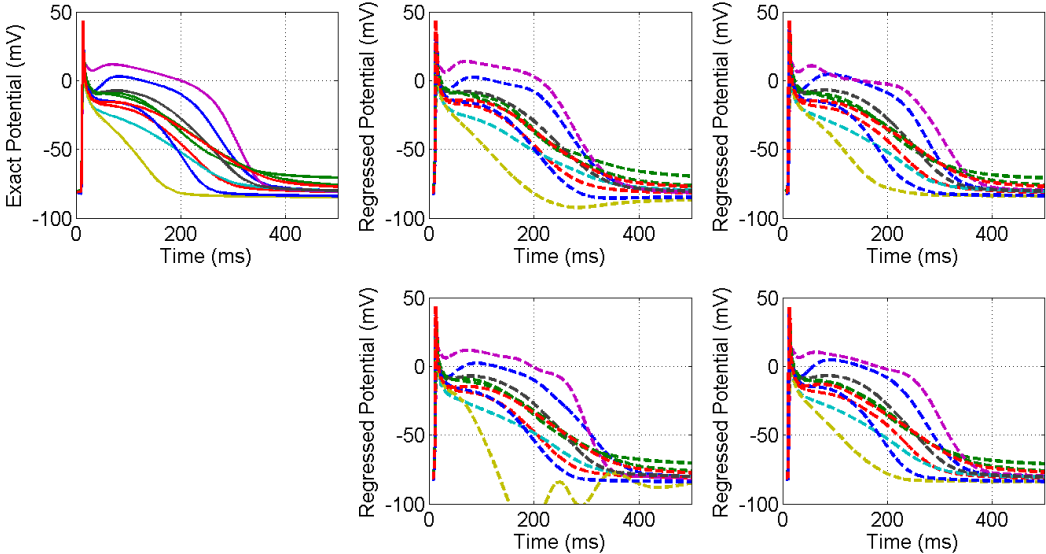
Figure 6.6: AP regression by MARS. 1st row: exact, $\mathcal{M}_1$, $\mathcal{M}_2$; 2nd row: $\mathcal{M}_3$, $\mathcal{M}_4$.
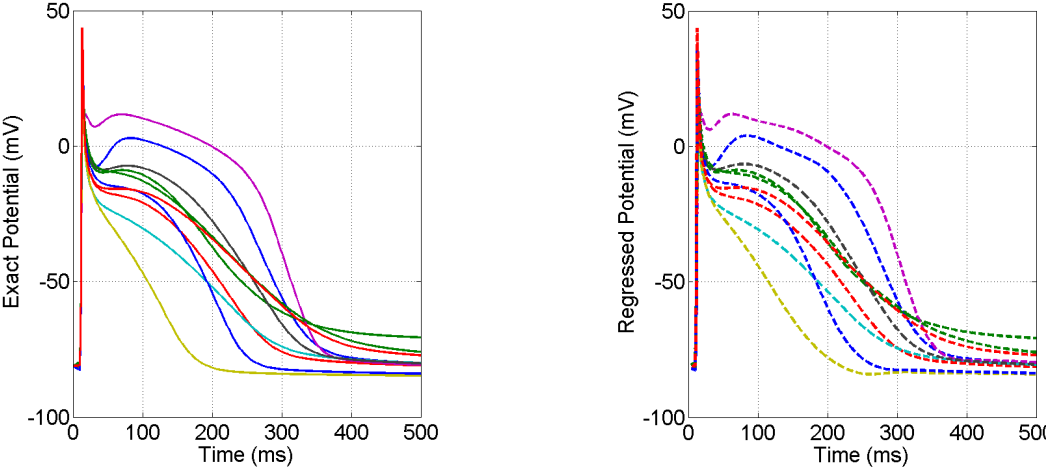

Figure 6.7: AP regression by PPR. Left: exact, Right: $\mathcal{M}_4$.

6.3.4 Application to tissue-level EP modeling

An application of this regression model to 3D tissue-level EP modeling was tested in this subsection. We used as reference a given time series $\mathbf{u}_{\text{ref}}$ of cellular AP, with resting potential -80.83 mV and AP amplitude 8 mV. To monitor upstroke, we used the MS model with parameters as in [88], except for choosing the change-over voltage parameter v_{gate}

Table 6.2: Errors of the regressed AP (by MARS) compared to the original AP.

Relative Error (%) in (90-percentile Mean SD)

Method	$\mathcal{M}_1$			$\mathcal{M}_2$			$\mathcal{M}_3$			$\mathcal{M}_4$		
MAD	5.18	2.84	2.33	2.54	1.19	1.22	2.39	1.42	4.21	2.90	1.38	2.18
V_{rest}	2.50	1.20	1.52	1.50	0.68	0.80	0.99	0.46	0.72	1.58	0.73	0.89
APD_{60}	11.88	5.48	6.68	5.66	2.75	3.12	9.37	4.53	4.53	5.84	2.68	2.94
APD_{40}	11.72	5.25	5.93	6.59	2.85	3.64	11.23	5.12	5.67	6.10	2.60	2.92
APD_{20}	18.93	8.17	11.29	8.25	3.88	7.75	12.75	5.87	9.17	9.00	4.52	8.69
AUC	6.11	2.98	3.53	2.94	1.37	1.72	6.38	2.95	3.04	3.00	1.41	1.76

Table 6.3: Errors of the regressed AP (by PPR) compared to the original AP.

Relative Error (%) in (90-percentile Mean SD)

Method	$\mathcal{M}_1$			$\mathcal{M}_2$			$\mathcal{M}_3$			$\mathcal{M}_4$		
MAD	45.10	23.32	16.43	45.72	23.25	16.50	1.75	0.91	1.21	2.10	0.99	1.47
V_{rest}	1.83	0.86	0.91	1.64	0.74	0.85	0.81	0.37	0.50	1.42	0.67	0.80
APD_{60}	7.51	3.35	3.59	6.12	2.66	3.12	6.59	2.88	3.41	6.12	2.73	3.31
APD_{40}	8.30	3.56	4.14	5.98	2.84	3.05	6.35	2.89	3.52	5.61	2.76	2.84
APD_{20}	12.37	5.29	7.02	8.62	4.05	4.94	8.06	3.72	6.94	7.87	3.51	7.47
AUC	3.65	1.70	2.06	2.99	1.39	1.55	3.82	1.74	2.06	2.70	1.26	1.58

to be 0.46=(-40+80.83)/(8+80.83), consistent with the I_{Na} channel upstroke -40 mV in the original CRN model. We simulate the potential propagation on a patient-specific geometry of left and right atrium reconstructed from medical images, with stimulus applied on the sino-atrial node. Cell model registration started at the moment $u = -10$ mV right after AP depolarization, and stopped while $u = -75$ mV after AP repolarization. The time step Δt was 0.05 ms.

Using registration of the proposed regression model reduced the computational time by 75% (from 84 seconds of computation time for solving one heart cycle with the original CRN model, to 23 seconds with the reduced model), see results in table 6.4 with different final time T. The computation speed was dramatically improved as we increased the time step for the regression model registration, which is prohibited by stability requirements of numerical solvers for the original CRN model. For $\Delta t = 1$ ms, the computational cost was reduced to 1.5% and the simulation was almost real-time (in the order of one second per heart cycle). All computations were performed on a standard workstation. Some snapshots of the simulation are reported in Figure 6.8.

Table 6.4: Efficiency comparison between the original CRN model and the reduced CRN model.

Model	Δt	$T{=}1$ s	$T{=}2$ s	$T{=}4$ s
Original CRN	0.05 ms	167.78 s	339.42 s	676.03 s
Reduced CRN	0.05 ms	46.12 s	94.5 s	128.88 s
Reduced CRN	0.5 ms	4.67 s	9.64 s	18.5 s
Reduced CRN	1 ms	2.57 s	4.7 s	9.46 s

t = 10 ms

t = 130 ms

t = 250 ms

t = 370 ms
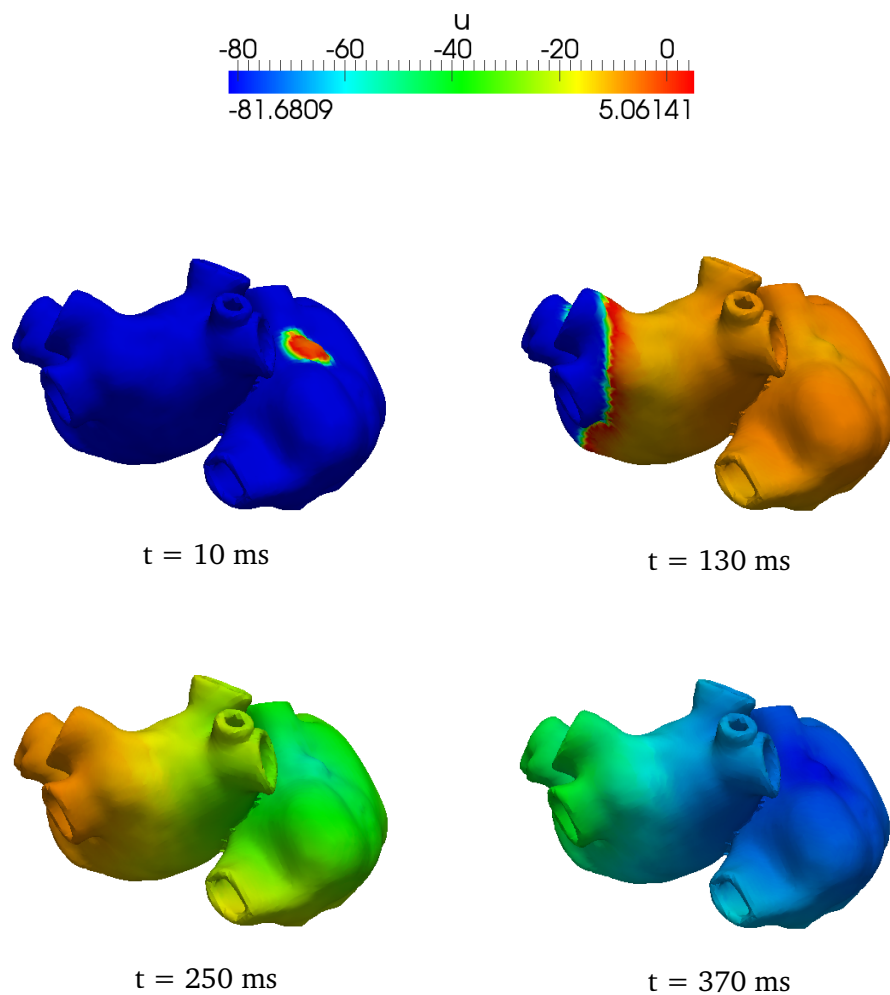
Figure 6.8: Simulation on the atria by the regression model registration. From left to right: t =10 ms; t = 130 ms; t=250 ms; t = 370 ms.

Table 6.5: Errors of the regressed AP (by PPR with DI parameter) compared to the original AP.

Relative Error (%) in (90-percentile Mean SD)

Data	SD = 0.3			SD = 0.2		
MAD	10.1659	4.61849	5.57327	6.297828	4.386615	4.17627
V_{rest}	0.56859	0.27091	0.49154	0.20318	0.098738	0.13962
APD_{60}	10.0082	4.53703	4.80177	3.9263	1.60495	2.31019
APD_{40}	12.6205	5.48759	7.15154	5.37466	2.17504	2.62042
APD_{20}	15.32442	6.771756	13.04303	6.65314	2.93477	5.29514
AUC	4.69999	2.09210	2.38051	2.0124	0.85393	0.95506

6.3.5   Restitution study by diastolic interval change

The reduced model can be extended to recover the restitution properties of AP (see Sec. 2.1.2 or Fig. 2.5) with varying diastolic interval (DI). DI is defined as

$$DI = CL - APD_{60},$$

with CL being the cycle length of heart beat. In a preliminary experiment, we added DI to the set of model parameters $\boldsymbol{\theta}$; the baseline value of DI was 250 ms, and it was randomly sampled to generate the observation matrix, as explained above. More sophisticated control of the action potential duration alternans, as done in [66], is a possible extension of this work. Random scale factors for DI were in log-normal distribution with mean value 1 and standard deviation 0.3. We increased the number of training data to be 1500 since the AP dynamics is more complex.

In this test the prediction fit of AP was not as good as in previous ones, but the overall fitting errors were in an acceptable range (in the order of 5%). Especially if we use sample data with standard deviation 0.2, the regression result is comparable with the case that the DI parameter is not included. See the error list in table 6.5 and a sample of predicted APs in Figure 6.9. In this test, the PPR regression was adopted. The MARS regression provides a little worse prediction but still with acceptable error. This test result suggests that the regression model has potential use in modeling complex pathological patterns in diseases such as atrial fibrillation.
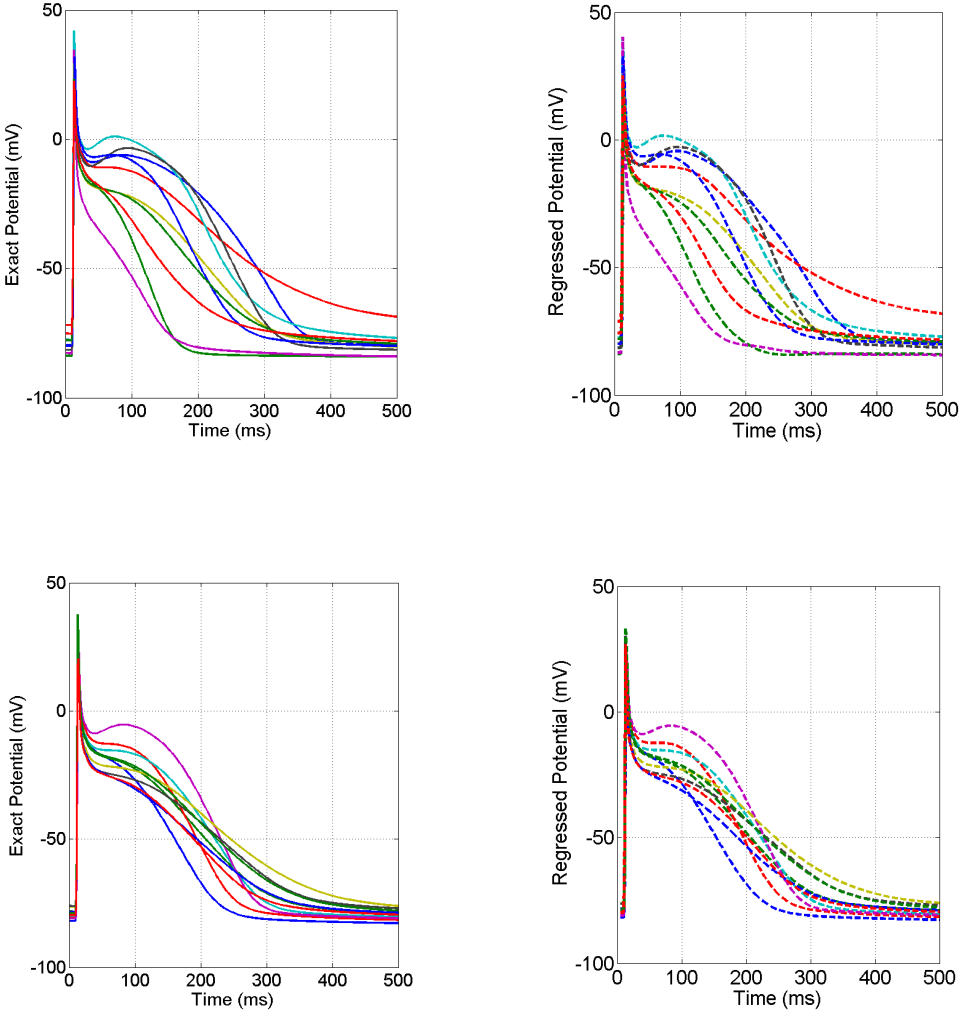
Figure 6.9: AP regression by PPR with DI parameter. Top two: SD = 0.3; bottom two: SD = 0.2

6.4   Discussion and conclusion

In this chapter, we use a data-driven approach for the CRN cellular model reduction. The regression model we designed is able to capture the AP dynamics of the original CRN model, while in a very simple form. Before the model construction, the AP manifold dimension was reduced 15 parameters using a manifold learning technique (PCA). In model construction, different AP quantities (APD for instance) were accurately regressed using the PPR method. The embedding coordinates of the action potential in its reduced space were then regressed by PPR or MARS using the above quantities as extra parameters and an iterative regression strategy on the outputs could be optionally applied. This approach returns accurate results even with sample parameters having standard deviation 0.3. It's also interesting to see that this approach can still be used to study the restitution properties of AP with changing diastolic intervals. Finally and most significantly, the application of this regression model to tissue-level EP modeling dramatically improves the computational efficiency: it decreases the computational time up to two orders of magnitude as compared to using the original non-reduced model and enables almost real-time computations (order of seconds for computing a heart cycle on a standard workstation).

The statistical learning approach is general enough, that it can be applied to the reduction of any other cardiac cell models. Moreover, with a proper design of the training data set the reduced model can be tailored to the specific application, for the prediction of the most relevant features (for instance, a specific ionic current or a channel blocker).

In future work, we will focus on more precise ways for monitoring AP upstroke, such as the use of the eikonal equation for the depolarization time, or a regression approach on the sodium ionic channel which controls the AP depolarization phase. We also intend to study the AP restitution properties with a more sophisticated control of the action potential duration alternans, as done in [66], with the aim of modeling complex pathological patterns such as atrial fibrillation.

Chapter 7

Conclusions

In this thesis, we address some challenges arose in cardiac electrophysiological modeling. The first part of the thesis (Chapter 3–5) is on the estimation of cardiac conductivities from potential measures. The inverse conductivity problem itself is novel. Surprisingly enough, there is few literature (and quite not consistent) on these parameter values, but the interest in an accurate *in vivo* estimation of these parameters is high since it is a crucial step for applying computational electrocardiology in practice. Here we bring our contributions:

1. we provide for the first time a rigorous mathematical formulation of the inverse conductivity problem based on constrained minimization arguments and an existence analysis;

2. we significantly improve numerical approaches in the literature by resorting to a derivative-based optimization method with the settlement of some challenges due to discontinuity;

3. thanks to the improvement at the previous point, we perform results in 3D that were not available in literatures on variational conductivity estimation;

4. we apply the POD-DEIM approach to the inverse conductivity problem, which features very different properties from classical problems, and reduce the online com-

putational effort by at least 90%;

5. we obtain a rather small set of samples by sampling the parameter space based on polar coordinates and densifying the "boundary layer" of the sample space utilizing Gauss–Lobatto nodes.

The second part of the thesis (Chapter 6) is an internship project accomplished at Siemens Corporate Research, Princeton, NJ. The work is on the development of a data-driven approach to the reduction of state-of-the-art cellular models used for atrial electrophysiological simulation. The novelties and advantages lie in the following aspects.

1. Our regression model keeps the ability to capture the complex dynamics of the original biophysically detailed model, while in very simple form and depending on a smaller number of parameters.

2. The reduced cellular model drastically improves the performance of tissue-level atrial electrophysiology (EP) modeling and enables almost real-time computations. This represents the first example of application of a statistical model reduction technique to the multiscale modeling of cardiac EP.

3. The model is also capable of describing the restitution properties of the AP.

References

[1] *Heart disease and antiarrhythmics*, WebMD. http://www.webmd.com/heart-disease/guide/medicine-antiarrhythmics.

[2] R. Adams and J. Fournier, *Sobolev spaces*, second ed., Elsevier, The Netherlands, 2003.

[3] J. Almquist, M. Wallman, I. Jacobson, and M. Jirstrand, *Modeling the effect of kv1.5 block on the canine action potential*, Biophysical Journal **99** (2010), no. 9, 2726–2736.

[4] E. Arian, M. Fahl, and E.W. Sachs, *Trust-region proper orthogonal decomposition for flow control*, Tech. report, Institute for Computer, 2000.

[5] O. Aslanidi, M. Colman, J. Stott, H. Dobrzynski, M. Boyett, A. Holden, and H. Zhang, *3d virtual human atria: A computational platform for studying clinical atrial fibrillation*, Prog. Biophys. Mol. Biol. **107** (2011), 156–168.

[6] P. Astrid, *Reduction of process simulation models: a proper orthogonal decomposition approach*, Ph.D. thesis, Eindhoven University of Technology, 2004.

[7] F. Atienza, J. Almendral, J. Moreno, R. Vaidyanathan, A. Talkachou, J. Kalifa, A. Arenal, J. Villacastin, E. Torrecilla, A. Sanchez, R. Ploutz-Snyder, J. Jalife, and O. Berenfeld, *Activation of inward rectifier potassium channels accelerates atrial fibrillation in humans: Evidence for a reentrant mechanism*, Circulation **114** (2006), 2434–2442.

[8] S. Banerjee, J.V. Cole, and K.F. Jensen, *Nonlinear model reduction strategies for rapid thermal processing systems*, Semiconductor Manufacturing, IEEE Transactions on **11** (1998), no. 2, 266–275.

[9] M. Barrault, Y. Maday, N.C. Nguyen, and A.T. Patera, *An 'empirical interpolation' method: application to efficient reduced-basis discretization of partial differential equations*, Comptes Rendus Mathematique **339** (2004), no. 9, 667 – 672.

[10] B. Barros, R. Santos, M. Lobosco, and S. Alonso, *Simulation of ectopic pacemakers in the heart: Multiple ectopic beats generated by reentry inside fibrotic regions*, BioMed Research International (2015), Article ID 713058, in press.

[11] J. Bayer, R. Blake, G. Plank, and N. Trayanova, *A novel rule-based algorithm for assigning myocardial fiber orientation to computational heart models*, Ann. Biomed. Eng. **40** (2012), no. 10, 2243–2254.

[12] T. Bechtold, M. Striebel, K. Mohaghegh, and E.J.W. ter Maten, *Nonlinear model order reduction in nanoelectronics: Combination of pod and tpwl*, PAMM **8** (2008), no. 1, 10057–10060.

[13] G. Beeler and H. Reuter, *Reconstruction of the action potential of ventricular myocardial fibres*, J. Physiol. **268** (1977), no. 1, 177–210.

[14] L. Bertagna and A. Veneziani, *A model reduction approach for the variational estimation of vascular compliance by solving an inverse fluid-structure interaction problem*, Inverse Problems **30** (2014), 055006.

[15] L. Biegler, G. Biros, O. Ghattas, M. Heinkenschloss, D. Keyes, B. Mallick, Y. Marzouk, L. Tenorio, and K. Willcox (eds.), *Large-scale inverse problems and quantification of uncertainty*, Wiley Online Library, 2011.

[16] P. Bochev and R. Lehouc, *On the finite element solution of the pure neumann problem*, Siam Review **47** (2005), no. 1, 50–66.

[17] M. Boulakia and J-F. Gerbeau, *Parameter identification in cardiac electrophysiology using proper orthogonal decomposition method*, Functional Imaging and Modeling of the Heart, Lecture Notes in Computer Science, vol. 6666, 2011, pp. 315–322.

[18] M. Boulakia, E. Schenone, and J-F. Gerbeau, *Reduced-order modeling for cardiac electrophysiology. application to parameter identification*, Int. J. Num. Meth. Biomed. Engng. **28** (2012), no. 6–7, 727–744.

[19] Y. Bourgault, Y. Coudière, and C. Pierre, *Existence and uniqueness of the solution for the bidomain model used in cardiac electrophysiology*, Nonlinear Anal. Real World Appl. **10** (2009), no. 1, 458–482.

[20] Y. Bourgault and C. Pierre, *Comparing the bidomain and monodomain models in electro-cardiology through convergence analysis*, December 2010.

[21] A. Bueno-Orovio, E. Cherry, and F. Fenton, *Minimal model for human ventricular action potentials in tissue*, J. Theor. Biol. **253** (2008), no. 3, 544–60.

[22] A. Buffa, Y. Maday, A.T. Patera, C. Prud'homme, and G. Turinici, *A priori convergence of the greedy algorithm for the parametrized reduced basis method*, ESAIM: Mathematical Modelling and Numerical Analysis **46** (2012), 595–603.

[23] T. Bui-Thanh, M. Damodaran, and K.E. Willcox, *Aerodynamic data reconstruction and inverse design using proper orthogonal decomposition*, AIAA Journal **42** (2004), no. 8, 1505–1516.

[24] T. Bui-Thanh, K. Willcox, and O. Ghattas, *Model reduction for large-scale systems with high-dimensional parametric input space*, SIAM Journal on Scientific Computing **30** (2008), no. 6, 3270–3288.

[25] J.W. Cain, *Taking math to heart: Mathematical challenges in cardiac electrophysiology*, Notices Amer. Math. Soc (2011), 542–549.

[26] M.A. Cardoso and L.J. Durlofsky, *Linearized reduced-order models for subsurface flow simulation*, J. Comput. Phys. **229** (2010), no. 3, 681–700.

[27] K. Carlberg and C. Farhat, *A compact proper orthogonal decomposition basis for optimization-oriented reduced-order models*, (2008), no. 2008-5964.

[28] N. Chamakuri, K. Kunisch, and G. Plank, *Pde constrained optimization of electrical defibrillation in a 3d ventricular slice geometry*, International Journal for Numerical Methods in Biomedical Engineering (2015), n/a–n/a.

[29] S. Chaturantabut, *Dimension reduction for unsteady nonlinear partial differential equations via empirical interpolation methods*, Master's thesis, Rice University, 2008.

[30] S. Chaturantabut, *Nonlinear model reduction via discrete empirical interpolation*, Ph.D. thesis, Rice University, 2011.

[31] J. Chen, M. Henneman, M. Trimble, J. Bax, S. Borges-Neto, A. Iskandrian, K. Nichols, and E. Garcia, *Assessment of left ventricular mechanical dyssynchrony by phase analysis of ecg-gated spect myocardial perfusion imaging*, Journal of Nuclear Cardiology **15** (2008), no. 1, 127–136.

[32] E.M. Cherry and F.H. Fenton, *Visualization of spiral and scroll waves in simulated and experimental cardiac tissue*, New Journal of Physics **10** (2008), no. 12, 125016.

[33] R. Clayton, O. Bernus, E. Cherry, H. Dierckx, F. Fenton, L. Mirabella, A. Panfilov, F. Sachse, G. Seemann, and H. Zhang, *Models of cardiac tissue electrophysiology: Progress, challenges and open questions*, Prog. Biophys. Mol. Biol. **104** (2011), no. 1-3, 22–48.

[34] L. Clerc, *Directional differences of impulse spread in trabecular muscle from mammalian heart*, J. Physiol. **255** (1976), 335–346.

[35] M.J.M. Cluitmans, P. Bonizzi, J.M.H. Karel, P.G.A. Volders, R.L.M. Peeters, and R.L. Westra, *Inverse reconstruction of epicardial potentials improved by vectorcardiography and realistic potentials*, Computing in Cardiology Conference (CinC), 2013, 2013, pp. 369–372.

[36] M. Courtemanche, R. Ramirez, and S. Nattel, *Ionic mechanisms underlying human atrial action potential properties: insights from a mathematical model*, Am. J. Physiol. **275** (1998), H301–H321.

[37] L. Dang, N. Virag, Z. Ihara, V. Jacquemet, J.-M. Vesin, J. Schlaepfer, P. Ruchat, and L. Kappenberger, *Evaluation of ablation patterns using a biophysical model of atrial fibrillation*, Annals of Biomedical Engineering **33** (2005), no. 4, 465–474.

[38] M.C. Delfour and J.P. Zolésio., *Shapes and geometries: analysis, differential calculus, and optimization.*, Society for Industrial and Applied Mathematics, Philadelphia, 2001.

[39] ———, *Shapes and geometries: Metrics, analysis, differential calculus, and optimization*, second ed., Society for Industrial and Applied Mathematics, Philadelphia, 2010.

[40] M. D'Elia, L. Mirabella, T. Passerini, M. Perego, M. Piccinelli, C. Vergara, and A. Veneziani, *Applications of variational data assimilation in computational hemodynamics*, Modeling of Physiological Flows, Springer, New York, 2011, pp. 363–394.

[41] N. Dong and J. Roychowdhury, *Piecewise polynomial nonlinear model reduction*, Design Automation Conference, 2003. Proceedings, June 2003, pp. 484–489.

[42] Q. Du, V. Faber, and M. Gunzburger, *Centroidal voronoi tessellations: Applications and algorithms*, SIAM Rev. **41** (1999), no. 4, 637–676.

[43] B. Engquist, A. Tornberg, and R. Tsai, *Discretization of dirac delta functions in level set methods*, J. Comput. Phys. **207** (2005), no. 1, 28–51.

[44] F. Fenton and E. Cherry, *Models of cardiac cell*, Scholarpedia **3** (2008), no. 8, 1868.

[45] F. Fenton and A. Karma, *Vortex dynamics in three-dimensional continuous myocardium with fiber rotation: filament instability and fibrillation*, Chaos **8** (1998), 20–47.

[46] J.P. Fink and W.C. Rheinboldt, *On the error behavior of the reduced basis technique for nonlinear finite element approximations*, Journal of Applied Mathematics and Mechanics **63** (1983), 21–28.

[47] R. FitzHugh, *Impulses and physiological states in theoretical models of nerve membrane*, Biophys. J. **1** (1961), 445–466.

[48] M. Frangos, Y. Marzouk, K. Willcox, and B. van Bloemen Waanders, *Surrogate and reduced-order modeling: A comparison of approaches for large-scale statistical inverse problems*, Large-Scale Inverse Problems and Quantification of Uncertainty, Wiley Online Library, 2011, pp. 123–149.

[49] P. Colli Franzone and L. Pavarino, *A parallel solver for reaction-diffusion systems in computational electrocardiology*, Math. Mod. Meth. Appl. S. **14** (2004), no. 6, 883–911.

[50] P. Colli Franzone, L. F. Pavarino, and B. Taccardi, *Simulating patterns of excitation, repolarization and action potential duration with cardiac bidomain and monodomain models*, Math. Biosc. **197** (2005), 35–66.

[51] P. Colli Franzone and G. Savaré, *Degenerate evolution systems modeling the cardiac electric field at micro-and macroscopic level*, Progress in nonlinear Differential Equations and Their Applications **50** (2002), 49–78.

[52] J. Friedman, T. Hastie, and R. Tibshirani, *The elements of statistical learning: Data mining, inference, and prediction*, Springer, 2009.

[53] J. Friedman and W. Stuetzle, *Projection pursuit regression*, J. Amer. Statist. Assoc. **76** (1981), 817–823.

[54] D. Galbally, K. Fidkowski, K. Willcox, and O. Ghattas, *Non-linear model reduction for uncertainty quantification in large-scale inverse problems*, International Journal for Numerical Methods in Engineering **81** (2010), no. 12, 1581–1608.

[55] D. Geselowitz, *An application of electrocardiographic lead theory to impedance plethysmography*, IEEE Trans. Biomed. Eng. **BME-18** (1971), no. 1, 38–41.

[56] L. Gerardo Giorda, L. Mirabella, F. Nobile, M. Perego, and A. Veneziani, *A model-based block-triangular preconditioner for the bidomain system in electrocardiology*, J. Comput. Phys. **228** (2009), no. 10, 3625–3639.

[57] L. Gerardo Giorda, M. Perego, and A. Veneziani, *Optimized schwarz coupling of bidomain and monodomain models in electrocardiology*, ESAIM: Mathematical Modelling and Numerical Analysis **45** (2011), no. 2, 309–334.

[58] L. Graham and D. Kilpatrick, *Estimation of the bidomain conductivity parameters of cardiac tissue from extracellular potential distributions initiated by point stimulation*, Ann. Biomed. Eng. **38** (2010), no. 12, 3630–3648.

[59] M.D. Gunzburger, *Perspectives in flow control and optimization. advances in design and control*, SIAM, Philadelphia, 2002.

[60] F. Hecht, *Freefem++ software.* http://www.freefem.org/ff++, 2013.

[61] S.Y. Ho, R.H. Anderson, and D. Sánchez-Quintana, *Atrial structure and fibres: morphologic bases of atrial conduction*, Cardiovascular Research **54** (2002), no. 2, 325–336.

[62] S.Y. Ho and D. Sánchez-Quintana, *The importance of atrial structure and fibers*, Clinical Anatomy **22** (2009), no. 1, 52–63.

[63] A. Hodgkin and A. Huxley, *A quantitative description of membrane current and its application to conduction and excitation in nerve*, J. Physiol. **117** (1952), no. 4, 500–544.

[64] E.W. Hsu and C.S. Henriquez, *Myocardial fiber orientation mapping using reduced encoding diffusion tensor imaging*, Journal of Cardiovascular Magnetic Resonance **3** (2001), no. 4, 339–47.

[65] P. Johnston, *A sensitivity study of conductivity values in the passive bidomain equation*, Math. Biosci. **232** (2011), no. 2, 142–150.

[66] U. Kanu, S. Iravanian, R. Gilmour, and D. Christini, *Control of action potential duration alternans in canine cardiac ventricular tissue*, IEEE Trans. Biomed. Eng. **58** (2011), no. 4.

[67] E. Kayvanpour, T. Mansi, F. Sedaghat-Hamedani, A. Amr, D. Neumann, B. Georgescu, P. Seegerer, A. Kamen, J. Haas, K. S. Frese, M. Irawati, V. Wirsz, E.AND King, S. Buss, D. Mereles, E. Zitron, A. Keller, H. A. Katus, D. Comaniciu, and B. Meder, *Towards personalized cardiology: Multi-scale modeling of the failing heart*, PLoS ONE **10** (2015), no. 7, e0134869.

[68] D.J. Knezevic, N. Nguyen, and A.T. Patera, *Reduced basis approximation and a posteriori error estimation for the parametrized unsteady boussinesq equations*, Mathematical Models and Methods in Applied Sciences **21** (2011), no. 07, 1415–1442.

[69] B. Kogan, *Introduction to computational cardiology*, Springer, New York, 2009.

[70] S. Kokoska, *Introductory statistics, a problem-solving approach*, W. H. Freeman, 2011.

[71] M.W. Krueger, G. Seemann, K. Rhode, D.U.J. Keller, C. Schilling, A. Arujuna, J. Gill, M.D. O'Neill, R. Razavi, and O. Dossel, *Personalization of atrial anatomy and electrophysiology as a basis for clinical modeling of radio-frequency ablation of atrial fibrillation*, Medical Imaging, IEEE Transactions on **32** (2013), no. 1, 73–84.

[72] D. Krummen, J. Bayer, J. Ho, G. Ho, M. Smetak, P. Clopton, N. Trayanova, and S. Narayan, *Mechanisms of human atrial fibrillation initiation: clinical and computational studies of repolarization restitution and activation latency*, Circ. Arrhythm. Electrophysiol. **5** (2012), no. 6, 1149–59.

[73] K. Kunisch and S. Volkwein, *Galerkin proper orthogonal decomposition methods for a general equation in fluid dynamics*, SIAM Journal on Numerical Analysis **40** (2002), no. 2, 492–515.

[74] K. Kunisch and S. Volkwein, *Proper orthogonal decomposition for optimality systems*, ESAIM: Mathematical Modelling and Numerical Analysis **42** (2008), no. 1, 1–23.

[75] K. Kunisch and M. Wagner, *Optimal control of the bidomain system (ii): Uniqueness and regularity theorems for weak solutions*, Ann. Mat. Pura Appl. **192** (2013), no. 6, 951–986.

[76] I.J. LeGrice, P.J. Hunter, and B.H. Smaill, *Flaminar structure of the heart: a mathematical model*, Am. J. Physiol. Heart Circ. Physiol. **272** (1997), no. 5, H2466–2476.

[77] P. LeGuyader, F. Trelles, and P. Savard, *Extracellular measurement of anisotropic bidomain myocardial conductivities. i. theoretical analysis*, Annals Biomed. Eng. **29** (2001), 862–877.

[78] P. Lin, *Köthe-bochner function spaces*, Birkhäuser, Boston, 2003.

[79] C. Luo and Y. Rudy, *A model of the ventricular cardiac action potential: depolarization, repolarization and their interaction*, Circ. Res. **68** (1991).

[80] C. Luo and Y. Rudy, *Dynamic model of the cardiac ventricular action potential - simulations of ionic currents and concentration changes*, Circ. Res. **74** (1994), 1071–1097.

[81] T. Mansi, B. Georgescu, J. Hussan, P. Hunter, A. Kamen, and D. Comaniciu, *Data-driven reduction of a cardiac myofilament model*, Functional Imaging and Modeling of the Heart, Lecture Notes in Comput. Sci., vol. 7945, 2013, pp. 232–240.

[82] M.D. McKay, R.J. Beckman, and W.J. Conover, *A comparison of three methods for selecting values of input variables in the analysis of output from a computer code*, Technometrics **21** (1979), no. 2, pp. 239–245.

[83] S. Mendis, P. Puska, and B. Norrving, *Global atlas on cardiovascular disease prevention and control*, Geneva, Switzerland: World Health Organization (2011).

[84] S. Milborrow and R. Tibshirani, *Multivariate adaptive regression splines.* http://www.milbo.users.sonic.net/earth/.

[85] W.T. Miller and D.B. Geselowitz, *Simulation studies of the electrocardiogram. i. the normal heart*, Circ. Res. **43** (1978), no. 2, 301–315.

[86] L. Mirabella, F. Nobile, and A. Veneziani, *An a posteriori error estimator for model adaptivity in electrocardiology*, Comput. Method. Appl. M. **200** (2011), no. 37, 2727–2737.

[87] L. Mirsky, *Symmetric gauge functions and unitarily invariant norms*, The Quarterly Journal of Mathematics **11** (1960), no. 1, 50–59.

[88] C. Mitchell and D. Schaeffer, *A two-current model for the dynamics of cardiac membrane*, Bull. Math. Biol. **65** (2003), no. 5, 767–793.

[89] P. Moireau and D. Chapelle, *Reduced-order unscented kalman filtering with application to parameter identification in large-dimensional systems*, ESAIM: Contr. Optim. Ca. **17** (2011), 380–405.

[90] R.C. Barr P.C. Dolber M.S. Spach, J.F. Heidlage, *Cell size and communication: Role in structural and electrical development and remodeling of the heart*, Heart Rhythm **1** (2004), 500–515.

[91] A.L. Muzikant and C.S. Henriquez, *Validation of three-dimensional conduction models using experimental mapping: are we getting closer?*, Prog. Biophys. Mol. Biol. **69** (1998), no. 2-3, 205–23.

[92] C. Nagaiah, C. Engwer, and K. Kunisch, *Boundary control of bidomain equations with state dependent switching source functions in the ionic model*, J. Comput. Phys. **273** (2014), 227–242.

[93] C. Nagaiah, K. Kunisch, and G. Plank, *Numerical solution for optimal control of the reaction-diffusion equations in cardiac electrophysiology*, Comput. Optim. Appl. **49** (2011), no. 1, 149–178.

[94] J. Nagumo, S. Arimoto, and S. Yoshizawa, *An active pulse transmission line simulating nerve axon*, Proc. IRE. **50** (1962), 2061–2070.

[95] N.C. Nguyen, A.T. Patera, and J. Peraire, *A 'best points' interpolation method for efficient approximation of parametrized functions*, International Journal for Numerical Methods in Engineering **73** (2008), no. 4, 521–543.

[96] N.C. Nguyen, G. Rozza, D.B.P. Huynh, and A.T. Patera, *Reduced basis approximation and a posteriori error estimation for parametrized parabolic pdes: Application to real-time bayesian parameter estimation*, Large-Scale Inverse Problems and Quantification of Uncertainty, Wiley Online Library, 2011, pp. 151–177.

[97] B. Nielsen, T. Ruud, G. Lines, and A. Tveito, *Optimal monodomain approximation of the bidomain equations*, Appl. Math. Comp. **184** (2007), 276–290.

[98] J. Nocedal and S. Wright, *Numerical optimization*, second ed., Springer, New York, 2006.

[99] H.S. Oster, B. Taccardi, R.L. Lux, P.R. Ershler, and Y. Rudy, *Noninvasive electrocardiographic imaging: Reconstruction of epicardial potentials, electrograms, and isochrones and localization of single and multiple electrocardiac events*, Circulation **96** (1997), no. 3, 1012–1024.

[100] S. De Paris, *Lifev web site.* http://www.lifev.org, 2015.

[101] L. Pavarino and S. Scacchi, *Multilevel additive schwarz preconditioners for the bidomain reaction-diffusion system*, SIAM J. Sci. Comput. **31** (2008), 420–443.

[102] K. Pearson, *On lines and planes of closest fit to systems of points in space*, Philosophical Magazine Series 6 **2** (1901), no. 11, 559–572.

[103] M. Perego and A. Veneziani, *An efficient generalization of the rush-larsen method for solving electro-physiology membrane equations*, Electron. Trans. Numer. Anal. **35** (2009), 234–256.

[104] M. Perego, A. Veneziani, and C. Vergara, *A variational approach for estimating the compliance of the cardiovascular tissue: An inverse fluid-structure interaction problem*, SIAM J. Sci. Comput. **33** (2011), no. 3, 1181–1211.

[105] J. Peyrat, M. Sermesant, X. Pennec, H. Delingette, Chenyang X., E.R. McVeigh, and N. Ayache, *A computational framework for the statistical analysis of cardiac diffusion tensors: Application to a small database of canine hearts*, Medical Imaging, IEEE Transactions on **26** (2007), no. 11, 1500–1514.

[106] C. Pierre, *Preconditioning the bidomain model with almost linear complexity*, J. Comput. Phys. **231** (2012), no. 1, 82–97.

[107] R. Plonsey, *Bioelectric phenomena*, McGraw-Hill, 1969.

[108] A. Pullan, L. Cheng, and M. Buist, *Mathematically modelling the electrical activity of the heart: From cell to body surface and back again*, World Scientific Pub. Co. Inc., Singapore, 2005.

[109] A. Quarteroni (ed.), *Numerical models for differential problems*, Modeling, Simulation and Applications, vol. 2, Springer, 2009.

[110] A. Quarteroni, G. Rozza, and A. Manzoni, *Certified reduced basis approximation for parametrized partial differential equations and applications*, Journal of Mathematics in Industry **1** (2011), no. 1, 3.

[111] S. Rapaka, T. Mansi, B. Georgescu, M. Pop, G. Wright, A. Kamen, and D. Comaniciu, *Lbm-ep: Lattice-boltzmann method for fast cardiac electrophysiology simulation from 3d images,* Med. Image. Comput. Comput. Assist. Interv. **15** (2012), no. 2, 33–40.

[112] M. Rewienski and J. White, *A trajectory piecewise-linear approach to model order reduction and fast simulation of nonlinear circuits and micromachined devices*, Computer-Aided Design of Integrated Circuits and Systems, IEEE Transactions on **22** (2003), no. 2, 155–170.

[113] M.J. Rewieński, *A trajectory piecewise-linear approach to model order reduction of nonlinear dynamical systems*, Ph.D. thesis, Technical University of Gdańsk, 2003.

[114] D. Roberts, L. Hersh, and A. Scher, *Influence of cardiac fiber orientation on wavefront voltage, conduction, velocity and tissue resistivity in the dog*, Circ. Res. **44** (1979), no. 5, 701–712.

[115] D. Roberts and A. Scher, *Effect of tissue anisotropy on extracellular potential fields in canine myocardium in situ*, Circ. Res. **50** (1982), no. 3, 342–351.

[116] J. Rogers and A. McCulloch, *A collocation–galerkin finite element model of cardiac action potential propagation*, IEEE Trans. Biomed. Eng. **41** (1994), no. 8, 743–757.

[117] B. Roth, *Meandering of spiral waves in anisotropic cardiac tissue*, Physica. D. **150** (2001), 127–136.

[118] S. Roweis and L. Saul, *Nonlinear dimensionality reduction by locally linear embedding*, Science **290** (2000), no. 5500, 2323–2326.

[119] R. Sadleir and C. Henriquez, *Estimation of cardiac bidomain parameters from extracellular measurement: two dimensional study*, Ann. Biomed. Eng. **34** (2006), no. 8, 1289–1303.

[120] A.T. Sambelashvili, V.P. Nikolski, and I.R. Efimov, *Virtual electrode theory explains pacing threshold increase caused by cardiac tissue damage*, American Journal of Physiology - Heart and Circulatory Physiology **286** (2004), no. 6, H2183–H2194.

[121] O.H. Schmitt, *Biological information processing using the concept of interpenetrating domains*, Information Processing in the Nervous System (K. N. Leibovic, ed.), Springer, 1969, pp. 325–331.

[122] L. Sherwood, *Human physiology: From cells to systems*, 8 ed., Cengage Learning, 2012.

[123] E. Sobie, *Parameter sensitivity analysis in electrophysiological models using multivariable regression*, Biophys. J. **96** (2009), no. 4, 1264–74.

[124] M.S. Spach, *Anisotropy of cardiac tissue: A major determinant of conduction?*, J. Cardiovasc. Electrophysi. ol **10** (1999), 887–890.

[125] J. Stinstra, B. Hopenfeld, and R. MacLeod, *On the passive cardiac conductivity*, Ann. Biomed. Eng. **33** (2005), no. 12, 1743–1751.

[126] D. Streeter, H. Spotnitz, D. Patel, J. Ross, and E. Sonnenblick, *Fiber orientation in the canine left ventricle during diastole and systole*, Circ. Res. **24** (1969), no. 3, 339–347.

[127] Z. Syed, E. Vigmond, and L. Leon, *Atrial cell action potential parameter fitting using genetic algorithms*, Med. Biol. Eng. Comput. **43** (2005), 56–571.

[128] K. Tøndel, U. Indahl, A. Gjuvsland, J. Vik, P. Hunter, S. Omholt, and H. Martens, *Hierarchical cluster-based partial least squares regression (hc-plsr) is an efficient tool for metamodelling of nonlinear dynamic models*, BMC Systems Biology **5** (2011), 90.

[129] N. Trayanova, *Defibrillation of the heart: insights into mechanisms from modelling studies*, Experimental Physiology **91** (2006), 323–337.

[130] L. Tung, *A bi-domain model for describing ischemic myocardial d-c potentials*, Ph.D. thesis, Massachusetts Inst. Technol., 1978.

[131] K. Ten Tusscher, D. Noble, P. Noble, and A. Panfilov, *A model for human ventricular tissue*, Am. J. Physiol. **286** (2004), no. 4, H1573–H1589.

[132] M. Veneroni, *Reaction–diffusion systems for the macroscopic bidomain model of the cardiac electric field*, Nonlinear Anal. Real World Appl. **10** (2009), no. 2, 849–868.

[133] A. Veneziani and M. D'Elia, *Uncertainty quantification for data assimilation in a steady incompressible navier-stokes problem*, ESAIM: M2AN **47** (2013), no. 04, 1037–1057.

[134] A. Veneziani and C. Vergara, *Inverse problems in cardiovascular mathematics: toward patient-specific data assimilation and optimization*, Int. J. Num. Meth. Biomed. Eng. **29** (2013), no. 7, 723–725.

[135] C.T. Villongco, D.E. Krummen, P. Stark, J.H. Omens, and A.D. McCulloch, *Patient-specific modeling of ventricular activation pattern using surface ecg-derived vectorcardiogram in bundle branch block*, Progress in Biophysics and Molecular Biology **115** (2014), no. 2–3, 305 – 313.

[136] S. Volkwein, *Proper orthogonal decomposition: Theory and reduced-order modelling*, 2013.

[137] J.P. Wikswo, Jr., S.F. Lin, and R.A. Abbas, *Virtual electrodes in cardiac tissue: a common mechanism for anodal and cathodal stimulation*, Biophys. J. **69** (1995), no. 6, 2195–2210.

[138] H. Yang, T. Passerini, T. Mansi, and D. Comaniciu, *Data-driven model reduction for fast, high fidelity atrial electrophysiology computations*, Functional Imaging and Modeling of the Heart, Lecture Notes in Computer Science, vol. 9126, Springer International Publishing, 2015, pp. 466–474.

[139] H. Yang and A. Veneziani, *Estimation of cardiac conductivities in ventricular tissue by a variational approach*, Inverse Problems **31** (2015), no. 11, 115001.

[140] H. Yoshida and M. Nagaoka, *Multiple-relaxation-time lattice boltzmann model for the convection and anisotropic diffusion equation*, Journal of Computational Physics **229** (2010), no. 20, 7774 – 7795.

[141] O. Zettinig, T. Mansi, D. Neumann, B. Georgescu, S. Rapaka, P. Seegerer, E. Kayvanpour, F. Sedaghat-Hamedani, A. Amr, J. Haas, H. Steen, H. Katus, B. Meder,

N. Navab, A. Kamen, and D. Comaniciu, *Data-driven estimation of cardiac electrical diffusivity from 12-lead ecg signals*, Med. Image. Anal. **18** (2014), no. 8, 1361–1376.

[142] Y. Zheng, A. Barbu, B. Georgescu, M. Scheuering, and D. Comaniciu, *Four-chamber heart modeling and automatic segmentation for 3-d cardiac ct volumes using marginal space learning and steerable features*, IEEE Trans. Med. Imaging **27** (2008), no. 11, 1668–1681.

[143] L. Zhukov and A.H. Barr, *Heart-muscle fiber reconstruction from diffusion tensor mri*, Visualization, 2003. VIS 2003. IEEE, Oct 2003, pp. 597–602.